Verification of d-wave Pairing Symmetry by Microwave Intermodulation Distortion Measurements in Yttrium Barium Copper Oxide

by

Sang-Hoon Park

Submitted to the Department of Electrical Engineering and Computer Science
in partial fulfillment of the requirements for the degree of

Doctor of Philosophy in Electrical Engineering

at the

MASSACHUSETTS INSTITUTE OF TECHNOLOGY

June 2004

Author .....
Department of Electrical Engineering and Computer Science
May 21, 2004

Certified by .....
Daniel E. Oates
Visiting Scientist
Thesis Supervisor

Certified by .....
Terry P. Orlando
Professor of Electrical Engineering
Thesis Supervisor

Accepted by .....
Arthur C. Smith
Chairman, Department Committee on Graduate Students

Verification of d-wave Pairing Symmetry by Microwave Intermodulation Distortion Measurements in Yttrium Barium Copper Oxide

by

Sang-Hoon Park

Submitted to the Department of Electrical Engineering and Computer Science
on May 21, 2004, in partial fulfillment of the
requirements for the degree of
Doctor of Philosophy in Electrical Engineering

Abstract

We report measurements of the temperature and power dependence of the microwave frequency intermodulation distortion (IMD) in high quality pulsed laser deposition (PLD) Yttrium Barium Copper Oxide (YBCO) on $LaAlO_3$ substrate.
A low-temperature ($T < 30$ K) increase in IMD is the observation of an upturn of the nonlinear coefficient of the quadratic field dependence of the penetration depth. This IMD upturn is limited by the nonlinear Meissner effect that has been predicted for d-wave high-T_c superconductors.

Various amounts of IMD increase are observed for different films with impurity (Ni, Zn and Ca) doping and other defects. The demonstration of the IMD upturn and the nonlinear Meissner effect were possible because the IMD measurement is an extremely sensitive method to detect the penetration depth change at even less than 0.01 nm. IMDs from various samples tend to merge at a single universal value at 0 K regardless of disorder, defects, and impurities due to the node singularity at 0 K. There is a similar converging trend in IMD towards the transition temperature T_c due to the quasiparticle thermal excitation and depletion of superelectrons. It is most likely that IMD has both intrinsic and extrinsic contributions.

The $1/T^2$ divergence at low T of the IMD was theoretically predicted and confirmed with high quality PLD YBCO on $LaAlO_3$ substrate from below 30 K.

We found that Ni-doped YBCO gave an IMD increase comparable to high quality PLD YBCO. This finding agrees with the evidence that Ni (magnetic impurity) does not destroy superconductivity and preserves d-wave symmetry as shown in scanning tunnelling microscope experiments.

The off-the-resonance excitation experiment indicates that the response time scale of nonlinearity in IMD generation is not affected by the magnitude of two-tone separation $\Delta f = f_2 - f_1$ in YBCO on $LaAlO_3$ substrate. But, at low temperature ($T < 20$ K) and low output power at fundamental frequency ($P^1_{out} < -30$ dBm), the response time scale slows down IMD generation as the Δf increases in YBCO on

MgO substrate.

Thesis Supervisor: Daniel E. Oates
Title: Visiting Scientist

Thesis Supervisor: Terry P. Orlando
Title: Professor of Electrical Engineering

Acknowledgments

I would like to thank Dr. Daniel Oates at MIT Lincoln Laboratory for his guidance throughout this thesis research. Without the highest quality samples he provided, this thesis work would not be possible. I also would like to thank Professor Orlando for much valuable advice. He served as my academic and research advisor, and thesis committee member. Both Professors Hu and Berggren were kind enough to be on my research qualifying exam (RQE) committee. Professor Berggren was on my thesis committee, too.

At MIT Lincoln Laboratory, Group 86 leader Mark Gouker and assistant leader Leonard Johnson allowed me to fully concentrate on my thesis research. Group secretary Ms. JoAnne Rantz was kind to help me with any administrative matter. I was fortunate enough to get help from Mr. Bob Konieczka. He assembled all resonators used in this thesis research. Mr. George Fitch did all the programming work for data acquisition. Mr. Dan Baker patterned all samples used in this thesis research. Mr. Terry Weir, Rene Boisvert, Mark Seaver and Brian Reynolds helped me with instruments.

I also wish to thank Dr. John Derov for his hospitality and help at the Air Force Research Laboratory.

Dr. Jürgen Halbritter and Professor Matthias Hein in Germany helped me with some of the interpretations in this thesis work.

I would like to express my deepest gratitude to my wife Su-Jung Park for her never-ending love. She has been a constant inspiration to me. My two precious daughters Anne and Hye-Young Park have also been a great joy in my life.

Finally, the author wishes to thank US Air Force Office of Scientific Research for its support, and MIT Dean for Graduate Students, Dr. Isaac Colbert for support for my last semester.

Contents

List of Figures

List of Tables

Chapter 1

Introduction

1.1 Historical developments of superconductor

Kamerlingh Onnes at Leiden Cryogenic Laboratory found superconductivity in mercury at a critical temperature of 4.15 K in 1911 after he succeeded in producing liquid helium in 1908 [1]. Walther Meissner and Robert Oschenfeld showed in 1933 that a superconductor expels magnetic flux below its critical magnetic field $H_c(T)$ [2].

In 1935, Heinz and Fritz London brothers also showed that there is a characteristic length scale λ closely related to the magnetic field screening properties of the superconductor. The London penetration depth was shown to have an empirical relation

$$\lambda(T) = \frac{\lambda_o(0)}{\sqrt{1-(T/T_c)^4}} = \frac{1}{\sqrt{1-(T/T_c)^4}}\sqrt{\frac{\Lambda}{\mu_o}} \tag{1.1}$$

where $\lambda_o(0)$ is the penetration depth at 0 K, T the temperature, T_c the critical temperature above which the superconductivity disappears, Λ is defined as $m^*/n^*(q^*)^2$, $m^* = 2m$ is 2 times an electron mass, n^* the number density of superelectrons, $q^* = 2q$ is 2 times an electron charge, and μ_o is the permeability of free space. As the equation 1.1 shows, the penetration depth of superconductor is independent of frequency unlike the skin depth

$$\delta = \sqrt{\frac{2}{\omega \mu_o \sigma_o}} \tag{1.2}$$

of normal metals, where ω is the angular frequency, and σ_o is the conductivity.

In 1950, Ginzburg and Landau introduced another phenomenological theory of superconductivity which incorporates electrodynamics, quantum mechanics, and thermodynamics. The theory showed that the coherence length and the penetration depth were two fundamental characteristic lengths.

In 1953, Pippard introduced a coherence length to explain nonlocal electrodynamics [3]. The coherence length is the range of phase coherence in a Cooper pair, which consists of two electrons bound with an energy 2Δ which is called the energy gap of the superconductor. Pippard also realized that the coherence length decreases by the presence of defects or impurities through the mean free path. Pippard's empirical relation for coherence length is

$$\frac{1}{\xi_p} = \frac{1}{\xi_o} + \frac{1}{\alpha \ell} \tag{1.3}$$

where ξ_p is the Pippard coherence length, ξ_o the intrinsic coherence length, α a constant on the order of unity, and ℓ is the electron mean free path between scattering events. In the impure limit, ℓ decreases due to the increased scattering. From equation 1.3, when the electron mean free path $\ell << \xi_o$, then $\xi_p \simeq \ell$. Scattering not only reduces the coherence length but also increases the penetration depth [4].

In 1957 Abrikosov classified superconductors as two different types by the relative size of the penetration depth λ and the coherence length ξ [5]. When $\lambda << \xi$ the superconductor is called Type I. A Type I superconductor follows the nonlocal electrodynamics, since the value of the electric field changes within a coherence length. In addition, a Type I superconductor expels magnetic flux exclusively below its critical magnetic field $H_c(T)$. When $\lambda >> \xi$ the superconductor is called Type II. Local electrodynamics applies to this type of superconductor. All high temperature super-

conductors are Type II, which have two critical magnetic fields H_{c1} and H_{c2}. Below H_{c1}, the magnetic field is expelled from the material. Above H_{c2}, superconductivity is destroyed completely. For the range $H_{c1} < H < H_{c2}$, the magnetic field enters the superconductor in an array of vortices. Each vortex carries a quantum of flux Φ_o which is $2.0679 \times 10^{-15}\mathrm{Tm}^2$ [6].

The BCS theory developed in 1957 by Bardeen, Cooper and Schrieffer [7] was the first quantum-mechanical, microscopic theory of superconductivity. It showed that the formation of Cooper pairs through the electron-phonon interaction is responsible for superconductivity. The Cooper pair acts like a boson that is composed of a spin-up and spin-down electron pair. The BCS theory predicted the energy gap of the Cooper pair $E_g = 2\Delta(T)$, where $\Delta(T)$ is the gap function. In 1959, Gorkov showed that the Ginzburg-Landau theory could indeed be derived from the microscopic BCS theory.

In 1962, Josephson predicted that the Cooper pairs can tunnel through a very thin insulating barrier [8]. His remarkable prediction was verified experimentally by Anderson and Rowell in 1963 [9]. Now, the Josephson junction is a key element of many superconducting circuits.

A. Müller and G. Bednorz discovered in 1986 that a layered copper-oxide material, Ba-La-Cu-O became superconducting at temperatures exceeding 30 K [10]. Before this time, the highest critical temperature superconductor was Nb_3Ge (T_c was 23 K). In January of 1987, Paul C. W. Chu and Maw-Kuen Wu showed that $YBa_2Cu_3O_{7-\delta}$ had a critical temperature of 95 K. This was an exciting achievement since the YBCO could be cooled by liquid nitrogen, which compared to liquid helium, is cheap and widely available. Figure 1-1 is the structure of YBCO. Superelectrons are believed to flow on the CuO_2 plane. The Cu-O chains in the top and bottom probably act as charge reservoirs.

BCS theory was extremely successful in low-T_c superconductors. But, only partially successful in high-T_c superconductors. Evidence of Cooper pairs has been demonstrated, but the pairing mechanism of high-T_c superconductors is still elusive at this moment, even though there have been intensive research activities in the last

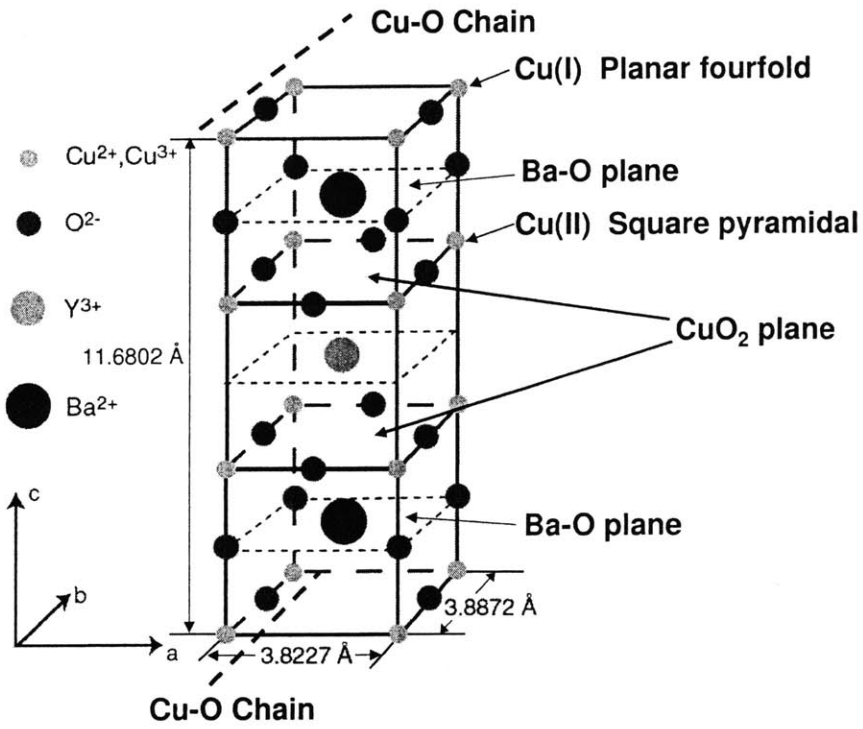

vspace1in

Figure 1-1: This is the structure of YBCO. CuO_2 planes sandwich the Y atoms. The Cu(II) atoms in CuO_2 plane have a square pyramidal coordination. The molecular formula of YBCO is expressed as $YBa_2Cu_3O_{7-x}$. When x is 0, the crystal is superconducting with T_c = 93 K and orthorhombic with lattice parameters a = 3.8227 , b = 3.8872 , and c = 11.6802 . The coordination of the Cu(I) in Cu-O chain is planar fourfold. When x = 1, the compound is non-superconducting and tetragonal. All oxygen sites on the top plane are vacant. The coordination of Cu(I) is linear twofold. When x = 0.03, the YBCO is known to be optimally doped.

decade [6].

1.2 Applications

All the high-T_c superconductors discovered so far are Type II, with very short coherence lengths and very high critical fields. Therefore, high-T_c superconductors are naturally useful in applications that require very high magnetic fields. For example, YBCO is estimated to be superconducting up to 100 Tesla. Flux pinning is especially important for high magnetic field applications to reduce hysteretic loss [11]. Circular particle accelerators, controlled fusion, maglev trains all require the high magnetic field provided by superconducting magnets. The Josephson tunneling junction is another important superconducting element. It is used in superconducting quantum interference device (SQUID), single-flux-quantum logic, and radiation detectors.

Very recently, quantum computing, which takes advantage of entangled states of Cooper pairs, has been proposed and shows a great potential for solving some problems far beyond the capability of the current supercomputers [12].

The demand for compact and high quality microwave passive devices such as resonators, filters, transmission lines, multiplexers, and delay lines has increased [13]. The significantly lower surface resistance of superconductors than that of normal metals is quite useful for resonators with high quality factors and low insertion loss. Figure 1-2 shows the measured filter response using YBCO, silver and gold metalization [14]. The filter was fabricated on 0.5-mm $LaAlO_3$ using gold, silver, and postannealed coevaporated YBCO. The YBCO filter had 1.0-dB insertion loss at 77 K compared with 5.9 dB for the silver filter at 77 K and 10.6-dB of insertion loss for the gold filter at 300 K.

The significantly low RF surface resistance also helps the device miniaturization. By reducing the size of the superconducting device, we can make it more compatible with the existing microwave circuits [15].

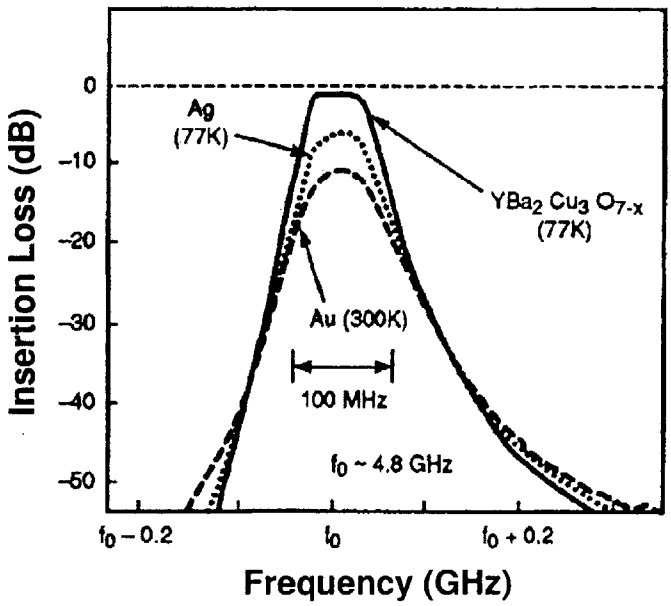

Figure 1-2: Measured filter response of an all-YBCO filter (Insertion loss IL is 1.0 dB) at 77 K, of an all-Ag filter (IL is 5.9 dB) at 77 K, and of an all-Au (IL is 10.6 dB) at 77 K. W. G. Lyons et. al. IEEE MTT-S Digest, p. 1230, 1991.

1.3 Motivation

In the two-fluid model, the total current flows through the resistive branch and the inductive branch as shown in Figure 1-3.

$$j_T = j_n + j_s \tag{1.4}$$

Here, j_T is the total current density, j_n the normal current density, and j_s is the supercurrent density. According to the two-fluid model [2, 4] the surface impedance Z_s is

$$Z_s = R_s + jX_s = \frac{\omega^2\mu^2 n_n \sigma_n \lambda^3}{2n} + j\omega\mu\lambda = \frac{\omega^2\mu^2\sigma_1\lambda^3}{2} + j\omega\mu\lambda \tag{1.5}$$

where μ_o(H/m) the permeability of free space, n_n(m^{-3}) the number density of electrons in unpaired states, $\sigma_n(\Omega^{-1}\text{m}^{-1})$ the normal-state conductivity, λ(m) the penetration depth, n(m^{-3}) the total density of conduction electrons, and $\sigma_1(\Omega^{-1}\text{m}^{-1})$ is the real part of the conductivity in the superconductor.

Superconductors only display true zero resistances with DC currents, since $X_s \to 0$ and the total current j_T in Figure 1-3 flows only through the inductive branch. At AC (RF) current, the inductive branch develops a non-zero impedance. So, some current is forced to flow through the resistive branch and then a superconductor develops loss. As we see, the normal fluid is involved in the surface resistance which is a source of loss in superconductors. But, the loss is still quite low compared to normal metals at the same temperatures.

Superconducting materials, however, have intrinsic problems. The resistance and inductance increase as the current increases. This nonlinear resistance or inductance is a source of nonlinear behavior, such as the intermodulation distortion and harmonic generation. The superconducting films used for measurements in this thesis are very thin (400 nm or 350 nm thickness). So, the high current density due to limited

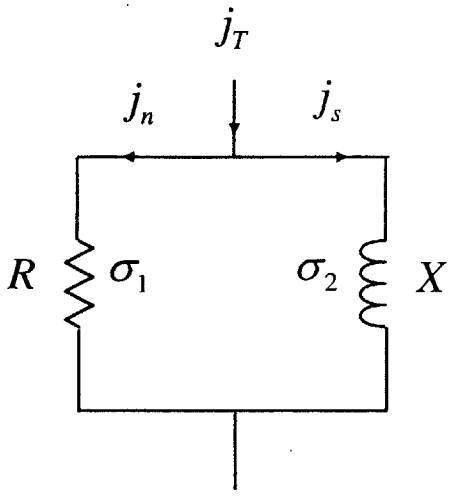

Figure 1-3: Superconductor shows both the normal channel and superconducting channel. j_T is the supercurrent density, j_n the normal current density, j_s the supercurrent density, R_s the surface resistance, and X_s is the surface reactance. σ_1 is the real part of conductivity and σ_2 is the imaginary part of conductivity.

cross-sectional film area increases the nonlinear behavior.

In filters, by mixing two input signals f_1 and f_2, many additional frequencies are generated by nonlinear behavior. Most important frequencies are $2f_2 - f_1$ and $2f_1 - f_2$. These additional two frequencies are called intermodulation (IMD) and are very close to the input frequencies applied to the filter. Then, IMD interferes with the input signals. So, IMD is still a major limiting factor for the design of high performance filters. The goal of our study is identifying IMD signals, understanding the generation mechanism and reducing IMDs by improving superconducting materials.

All of the superconducting samples used in this thesis were deposited on a dielectric substrate. To be a good substrate, the loss associated with it should be very low. In addition, the superconducting material and substrate should match each other in terms of the thermal expansion coefficient and lattice parameter [12] to ensure a high quality material deposited on the substrate.

Chapter 2

Intrinsic origin of nonlinearity in d-wave superconductor near the node

2.1 Quasiparticle excitation near the node singularity

Before this study, the general consensus was that IMD was generated by the extrinsic origins [16]. In the high-T_c superconductors, grain boundaries, weak-link Josephson regions, twin boundaries, defects, impurities, dislocations, magnetic impurities, inclusion of normal conducting materials, and heating effects including both global and local [17] are some of many possible extrinsic origins of nonlinear behavior that generate IMD.

But, this study shows that in d-wave superconductors, the IMD has intrinsic contributions at low temperatures. The theoretical prediction was: if the high-T_c superconductor has d-wave symmetry, which is generally believed now, IMD increases at low temperatures. In s-wave superconductors, the IMD was predicted to decrease exponentially.

Low-T_c conventional superconductors are known to have s-wave spherical symme-

try. s-wave superconductors have a true gap, but d-wave superconductors are believed to have 4 nodal lines along the cylindrical Fermi surface as shown in Figure 2-1. So, at the node, there are low energy excitations at all temperatures, with the result that the temperature dependence of the penetration depth is linear for $T << T_c$. On the Fermi surface, the energy of a quasiparticle in the presence of the superflow velocity $\vec{v}_s$ is given by [18, 19, 20].

$$E + \sigma_v = \sqrt{\varepsilon^2 + |\Delta(T)|^2} + \sigma_v \tag{2.1}$$

where ε is the quasiparticle energy in the normal state, the gap function $\Delta(T)$ is $\Delta_o(T)\sin(2\theta)$ for a $d_{x^2-y^2}$ -wave gap, θ the azimuthal angle referred to a node, $\sigma_v = \vec{v}_f \cdot \vec{v}_s$ the shift in the quasiparticle energy due to the superflow, $\vec{v}_f$ is the quasiparticle velocity.

The introduction of an arbitrary mass scale is not needed since we follow Yip and Sauls' constitutive equation relating the supercurrent, $\vec{j}_s$, to the velocity $\vec{v}_s = (1/2)[\vec{\partial}\phi + (2e/c)\vec{A}]$ [18].

In the equation 2.1, $\sqrt{\varepsilon^2 + |\Delta(T)|^2}$ is 0 at the node. So the term $\vec{v}_f \cdot \vec{v}_s$ becomes important in the presence of the superflow $\vec{v}_s$. When T = 0, there is no thermal excitation. The quasiparticle is excited only by $\vec{v}_f \cdot \vec{v}_s$.

The wedge of the occupied states of the quasiparticles near the node opposite to the $\vec{v}_s$ is indicated in the dotted circle in Figure 2-1. $\alpha_c = \sin^{-1}(v_f v_s/2\Delta_0)$ is the wedge angle of the occupied states of quasiparticles.

As a result, the unperturbed supercurrent $-e\vec{v}_s n$ is reduced by $\vec{j}_{qp}$ the quasiparticle backflow as shown in

$$\vec{j}(T, \vec{j}_s) = -e\vec{v}_s n - \vec{j}_{qp} \tag{2.2}$$

where $\vec{j}(T, \vec{j}_s)$ is the total current, and n is the total density at the Fermi level. The $\vec{j}_{qp}$ the quasiparticle backflow is expressed by BCS theory as [18, 19, 20, 21, 22]

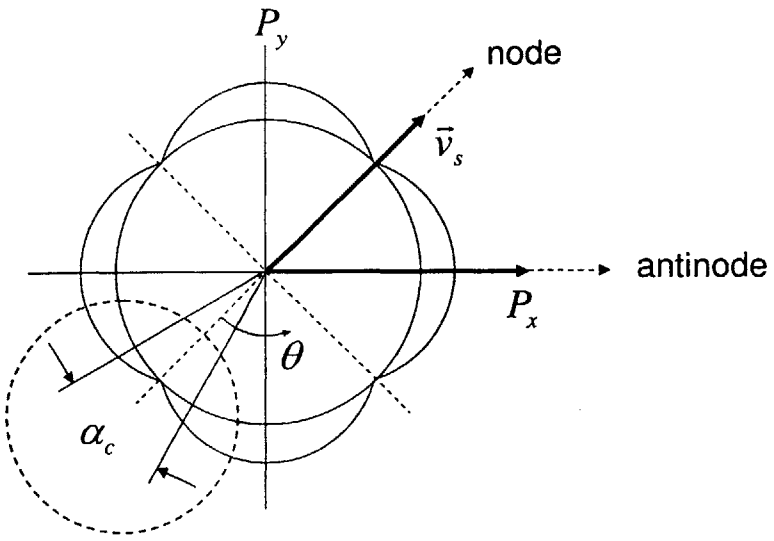

Figure 2-1: Gap function for $d_{x^2-y^2}$ symmetry in momentum space, $\alpha_c = \sin^{-1}(v_f v_s/2\Delta_o)$ is the wedge angle of the occupied states of the quasiparticles. When $v_f v_s = 2\Delta_o$ is the energy gap, α_c becomes 90^o , and θ is the azimuthal angle referred to a node.

$$\vec{j}_{qp} = -2eN(0)\int_0^{\infty} d\varepsilon \int_{-\alpha_c/2}^{\alpha_c/2} \frac{d\theta}{2\pi} \vec{v}_f f(\sqrt{\varepsilon^2 + |\Delta(T)|^2} + \vec{v}_f \cdot \vec{v}_s) \tag{2.3}$$

where $N(0)$ is the normal state density of states (dos), $f(\sqrt{\varepsilon^2 + |\Delta(T)|^2} + \vec{v}_f \cdot \vec{v}_s)$ is Fermi equilibrium distribution of quasiparticles. In a more general sense, when $v_f v_s$ is greater then the thermal energy term πT [18], expanding equation 2.3 to linear order and then substituting equation 2.3 into equation 2.2 gives

$$\vec{j} = -e\vec{v}_s n(1 - \frac{|\vec{v}_s|}{2\Delta_o/v_f}) \tag{2.4}$$

where $|\vec{v}_s|$ is the projected $\vec{v}_s$ to any of the four nodes.

Yip and Sauls [18] applied Maxwell's equations to equation 2.4 and obtained the linear field dependence of the penetration depth as a consequence of d-wave symmetry of the high-temperature superconductors as

$$\frac{1}{\lambda_{eff}} = \frac{1}{\lambda}(1 - \frac{2}{3}\frac{|\vec{H}|}{|\vec{H}_o|}), \vec{H}||\text{node} \tag{2.5}$$

$$\frac{1}{\lambda_{eff}} = \frac{1}{\lambda}(1 - \frac{1}{\sqrt{2}}\frac{2}{3}\frac{|\vec{H}|}{|\vec{H}_o|}), \vec{H}||\text{antinode} \tag{2.6}$$

where $H_o \simeq H_c$ is the critical field, $\vec{H}||$node and $\vec{H}||$antinode mean that the direction of field is parallel to the direction of the node and antinode, respectively as shown in Figure 2-1. The linear field dependence of the penetration depth in the local limit is commonly known as the nonlinear Meissner effect (NLME). Figure 2-2 shows more details of quasiparticle excitation near the node. As we just reviewed, when $v_f v_s > \pi T$ as in the region II, the field dependence of the penetration depth is linear. When $v_f v_s$ is lower than the thermal energy term πT as in the region I, some of the lowest energy states are occupied by thermally excited electrons.

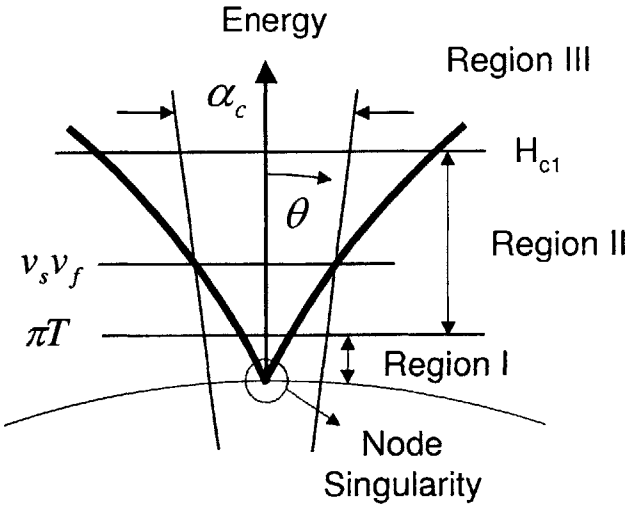

Figure 2-2: Quasiparticle excitations near the node: Region I ($v_f v_s < \pi T$) has the quadratic field dependence of the penetration depth, Region II ($v_f v_s > \pi T$) has the linear field dependence, and Region III is the Abrikosov vortex state. θ is the azimuthal angle referred to a node. The true node singularity is achieved at 0 K.

Yip and Sauls demonstrated that the quasiparticle backflow term in this region becomes quadratic with respect to the $\vec{v}_s$ [18]. So, the total current is given by

$$\vec{j} = -e\vec{v}_s n[1 - \alpha(T)(\frac{|\vec{v}_s|}{v_c})^2] \tag{2.7}$$

where $\alpha(T)$ contains the temperature dependence, and $v_c = \Delta_o(T)/v_f$ is the critical velocity over which the superconductivity disappears.

When the supercurrent $\vec{j}_s$ increases from zero, $v_f v_s$ increases, too. The quadratic field dependence in the region I crosses over to the linear field dependence of region II. When the field strength is greater than H_{c1}, the Abrikosov vortices start entering into the superconductor in the region III.

The node singularity at 0 K is removed by the thermal excitation at non zero temperatures. Impurities also remove the node singularity by increasing the lifetime from the quasiparticle scattering [18]. Furthermore, nonlocal electrodynamics removes the node singularity by increasing quasiparticle excitation due to the increased effective coherent length ξ_{eff} [23, 24].

Figure 2-3 shows the summary of Yip and Sauls' nonlinear current responses in *d*-wave superconductor.

Figure 2-4 shows the experimental observation of the nonlinear Meissner effect. As Yip and Sauls' theory predicted, there is a crossover from the quadratic to the linear dependence of the penetration depth as the current increases. Over H_{c1}, vortices start entering the superconductor and there is a slope change.

Yip and Sauls' theory predicted that the curvature of the quadratic current dependent region in Figure 2-4 is temperature dependent. But, the experimental data shows that it is very diificult to verify their prediction [25]. The corresponding $\Delta\lambda$ is less than 0.01 nm.

$j(T, j_s) = nev_s - j_{qp}$ **current density**

where $j_{qp} = -2eN(0)\int_0^{\infty} d\varepsilon_p \int_{-\alpha_c}^{\alpha_c} \frac{d\theta}{2\pi} v_f f\left[\sqrt{\varepsilon_p^2 + \Delta^2(\theta)} + v_f \cdot v_s\right]$ **BCS quasiparticle backflow**

$v_f v_s > \pi T$

Expanding to linear order

$$\vec{j} = -e\vec{v}n\left\{1 - \frac{|\vec{v}_s|}{2\Delta_o / v_f}\right\}$$

Maxwell's eq

$$\frac{1}{\lambda(H,T)} = \frac{1}{\lambda_o(T)}\left\{1 - \frac{2}{3}\frac{H}{H_o(T)}\right\} \quad \vec{H} \,//\, \text{node}$$

linear field dependence region

$v_f v_s < \pi T$

$$\vec{j} = -e\vec{v}_s n\left\{1 - \alpha(T)\left(\frac{v_s}{v_c}\right)^2\right\} \quad \textbf{where } v_c = \Delta_o(T)/v_f$$

Maxwell's eq

$$\frac{1}{\lambda(T,H)} = \frac{1}{\lambda(T)}\left\{1 - \frac{3}{4}\alpha(T)\left[\frac{H}{H_o(T)}\right]^2\right\}$$

quadratic field dependence region

Figure 2-3: Two limiting cases of nonlinear current responses for d-wave superconductor Yip and Sauls, PRL, vol. 69, pp. 2264-2267, 1992.

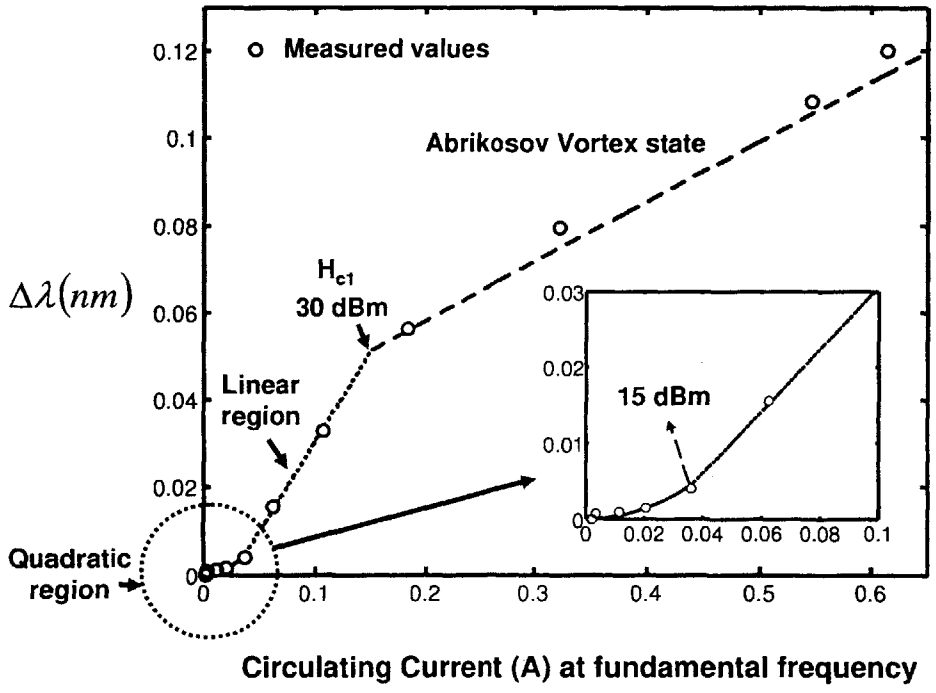

Figure 2-4: $\Delta\lambda$ vs circulating current with undoped YBCO on $LaAlO_3$ at 1.7 K.

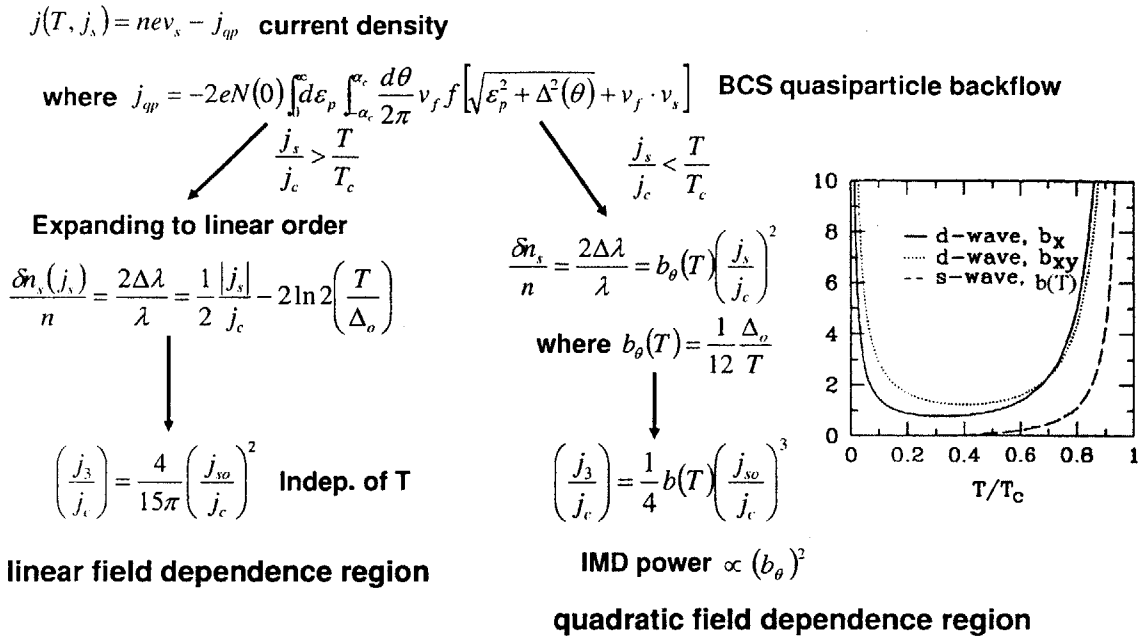

Figure 2-5: Two limiting cases of the nonlinear third harmonic current response for d-wave superconductor. Dahm and Scalapino, PRB, vol. 60, pp. 13125-13130, 1999.

2.2 Observation of nonlinear response due to the quasiparticle excitation

To overcome this difficulty, Dahm and Scalapino [20, 26, 27, 28, 29] extended Yip and Sauls' theory and obtained two limiting cases of the change in the superfluid density and they applied it to IMD and third harmonic generation (THG) to get more easily observable temperature dependence of the quadratic-current-dependent region [29]. The summary of their work is shown in Figure 2-5. Their analysis demonstrated that the temperature dependences of IMD and third harmonic generation have the same qualitative behaviors. Dahm and Scalapino started from the same quasiparticle backflow (equation 2.3) as Yip and Sauls. When $j_s/j_c < T/T_c$, the coefficient $b_\theta(T)$ of the quadratic-current term is temperature dependent. The $b_\theta(T)$ diverges as $1/T$ as shown in Figure 2-5 at low temperature and IMD power is proportional to $[b_\theta(T)]^2$ [29].

Figure 2-6 shows Dahm and Scalapino's theoretical prediction and my measure-

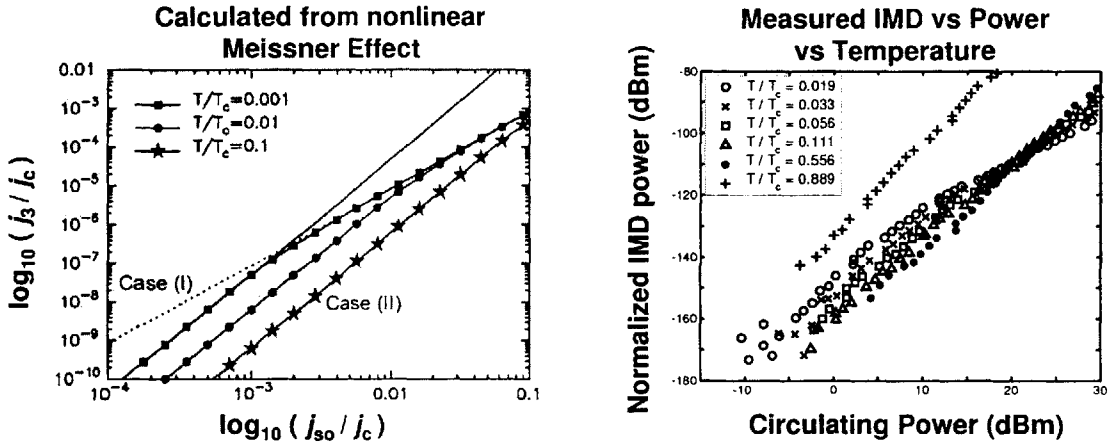

Case I): linear field dependence region

$$\frac{j_s}{j_c} > \frac{T}{T_c} \qquad \left(\frac{j_3}{j_c}\right) = \frac{4}{15\pi}\left(\frac{j_{so}}{j_c}\right)^2$$ **Indep of T**

High power: $\Delta\lambda \propto |I| \rightarrow IMD \propto P^2$

Case II): quadratic field dependence region

$$\frac{j_s}{j_c} < \frac{T}{T_c} \qquad \left(\frac{j_3}{j_c}\right) = \frac{1}{4}b(T)\left(\frac{j_{so}}{j_c}\right)^3$$

Low power: $\Delta\lambda \propto I^2 \rightarrow IMD \propto P^3$

Figure 2-6: Comparison of nonlinear response prediction and measured IMD. T. Dahm and D. J. Scalapino, PRB 60, 13125, 1999.

ments. The agreement is excellent. Indeed, as the temperature decreases, the nonlinear response increases due to the increase.

In this thesis, we will present the first convincing evidence of an IMD increase and saturation due to Yip-Sauls limit in YBCO at low temperature. We also confirmed the predicted $1/T^2$ *temperature dependence of IMD power below 30 K.*

IMD measurements have been proven to be an extremely sensitive method to detect the penetration depth change. Otherwise, observing change in λ is very difficult since $\Delta\lambda$ is exceedingly small with current change.

Chapter 3

Experiments and Background

3.1 Experiments

3.1.1 Thin films used

Table 3.1 shows the details of the films used in this study. All films were epitaxially deposited on the given substrate with the c-axis normal to the substrate surface. YBCO was deposited on $LaAlO_3$ by PLD, sputtering and coevaporation. One sample of YBCO on sapphire was included. Sample 1 is the highest quality [30]. Samples 2, 3, 4, and 5 were deposited under the same condition only the target was different, so the quality is similar to sample 1, but with impurities included. Ni and Zn are known to substitute for Cu. Ca is known to substitute for Y. In sample 6, the YBCO was grown by sputtering [31, 32]. The linear R_s measurements show that sample 6 is of lower quality than sample 1. Sample 7 [33] was made by overlaying 40 nm of 30 % Ca YBCO on another sample from the wafer that was also used for the sample 6. In sample 8, the YBCO was on sapphire [34, 35]. Samples on sapphire are known to have higher concentrations of defects since there is a mismatch in lattice and thermal expansion coefficient between YBCO and sapphire [36, 37]. Sample 9 was grown on MgO by coevaporation [38, 39]. Sample 10 [40] was measured for comparison purpose.

Number	Film Type	Substrate	Deposition Method	Source
1	$YBa_2Cu_3O_{7-X}$	(100) $LaAlO_3$	PLD	Koren
2	$YBa_2Ni_{0.06}Cu_{2.94}O_{7-X}$	$LaAlO_3$	PLD	Koren
3	$YBa_2Zn_{0.06}Cu_{2.94}O_{7-X}$	$LaAlO_3$	PLD	Koren
4	$Y_{0.94}Ca_{0.06}Ba_2Cu_3O_{7-X}$ 6 % Homogeneous Ca	$LaAlO_3$	PLD	Koren
5	$Y_{0.7}Ca_{0.3}Ba_2Cu_3O_{7-X}$ 6 % Homogeneous Ca	$LaAlO_3$	PLD	Koren
6	$YBa_2Cu_3O_{7-X}$	$LaAlO_3$	Sputtered	Anderson
7	$YBa_2Cu_3O_{7-X}$ + 30% Ca overlayer	$LaAlO_3$	Sputtered	Anderson & Hammerl
8	$YBa_2Cu_3O_{7-X}$	r-plane-Al_2O_3 (Sapphire)	PLD	Lorenz
9	$YBa_2Cu_3O_{7-X}$	(001) MgO	Coevaporation	Humphreys
10	Nb	$LaAlO_3$	Sputtered	Berggren

Table 3.1: Details of the films used in IMD measurements.

3.1.2 IMD measurements

Figure 3-1 shows the diagram of the two-tone IMD measurement setup. Two signal generators produce tones f_1 and f_2. The tone separation $\Delta f = f_2 - f_1$ was 1/32 of the 3dB bandwidth of the resonator, since the IMD power depends on Δf and $P_{IMD}(\Delta f)$ becomes independent of Δf at this extremely narrow separation. The power amplifier was used to increase the input signal power up to 30 dBm. The lowpass filter keeps the generator harmonics from entering the power combiner. The power combiner is a reciprocal device which can be also used as a power divider. The isolators were placed to suppress standing waves. The combined f_1 and f_2 were applied to the resonator. These input signals were calibrated with a power meter before each measurement. The third-order IMDs at $2f_1 - f_2$ and $2f_2 - f_1$ were measured by a spectrum analyzer versus the output power at f_1 and f_2. The signal generators and spectrum analyzer are phase-locked to a common 10 MHz reference signal.

The following mixing equations show how we get two intermodulation frequencies $2f_1 - f_2$ and $2f_2 - f_1$. In a superconductor, the impedance does not depend on the direction of current flow. Define the nonlinear impedance as

$$Z(t) = Z_o + a|I(t)| + bI^2(t) + \cdots. \tag{3.1}$$

Then the voltage across a nonlinear material is

$$V(t) \propto I(t)Z(t) = I(t)(Z_o + a|I(t)| + bI^2(t) + \cdots) = I(t)Z_o + aI^2(t) + bI^3(t) + \cdots. \tag{3.2}$$

If we let signal generator 1 current $I_1(t) = A\cos(\omega_1 t)$ and signal generator 2 current $I_2(t) = B\cos(\omega_2 t)$, where A and B are constants, the current in the power combiner becomes

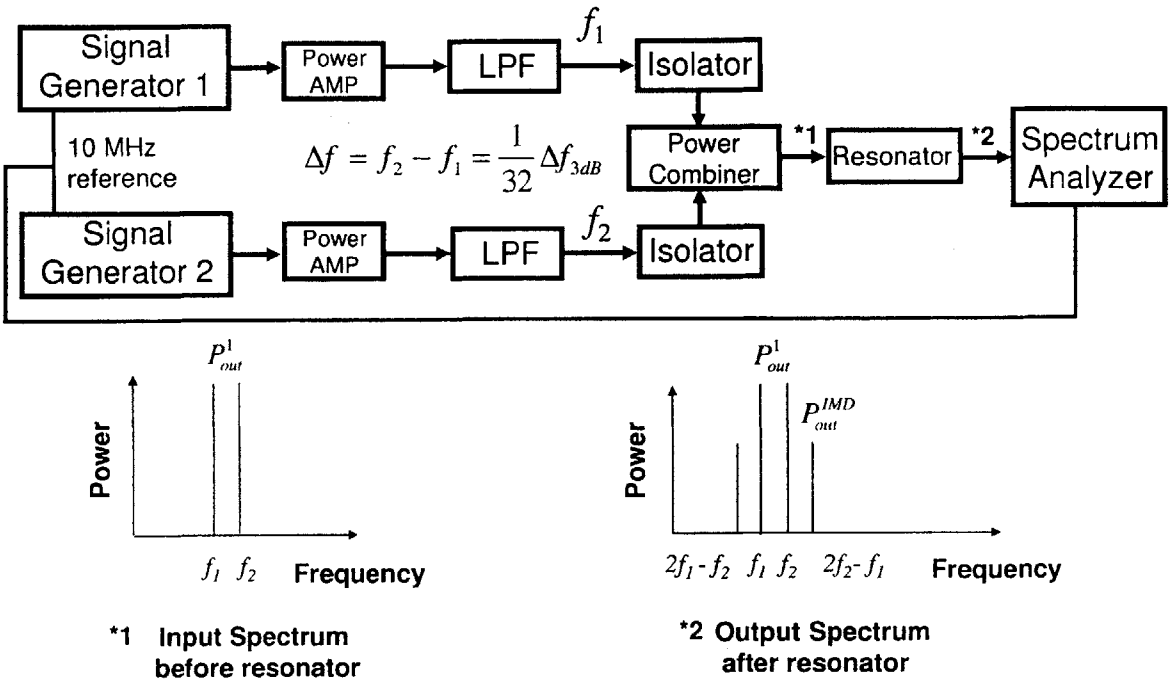

Figure 3-1: Two phased-locked generators produce two tones symmetrical about the center frequency of the resonator. The tone separation was 1/32 of the 3 dB bandwidth of the resonator. The power amplifiers were used to increase the signal input power up to 30 dBm. The lowpass filter keeps generator harmonics from entering the power combiner. The isolator was placed to suppress the standing waves. Then, the combined f_1 and f_2 were applied to the resonator. The third-order IMDs at $2f_1 - f_2$ and $2f_2 - f_1$ were measured as a function of the output power at fundamental frequency.

$$I(t) = I_1(t) + I_2(t) = A\cos(\omega_1 t) + B\cos(\omega_2 t). \tag{3.3}$$

Among all terms in equation (3.2), $bI^3(t)$ contributes the most to intermodulation power when the nonlinear inductance has I^2 dependence. Substituting equation (3.3) into $I^3(t)$ gives

$$I^3(t) = (A\cos(\omega_1 t) + B\cos(\omega_2 t))(A\cos(\omega_1 t) + B\cos(\omega_2 t))(A\cos(\omega_1 t) + B\cos(\omega_2 t)) \tag{3.4}$$

Simplifying and collecting terms with trigonometric identities, we found

$$I^3(t) = \frac{3}{4}A^2 B\cos(2\omega_1 - \omega_2)t + \frac{3}{4}AB^2\cos(2\omega_2 - \omega_1)t + \cdots \tag{3.5}$$

These intermodulation terms will be important since they fall within the passband of the resonator.

In equation (3.2), $aI^2(t)$ contributes the most to intermodulation power when the nonlinear inductance has $|I|$ dependence. But, the intermodulation frequencies will be the same as equation 3.5 [41].

3.1.3 Dewar, test probe and stripline resonator

Figure 3-2 is a photo of the IMD measurement setup. The right side of the photo shows one of the Dewars used. The boiling point of liquid helium 4 is 4.2 K at 1 atm. To obtain lower temperatures, a vacuum pump was used to decrease the vapor pressure of the liquid helium. In addition, helium 4 becomes superfluid below the lambda point T = 2.17 K. Superfluid helium is known to have no viscosity at all. Tight sealing of the test probe is especially important. The left side of Figure 3-3

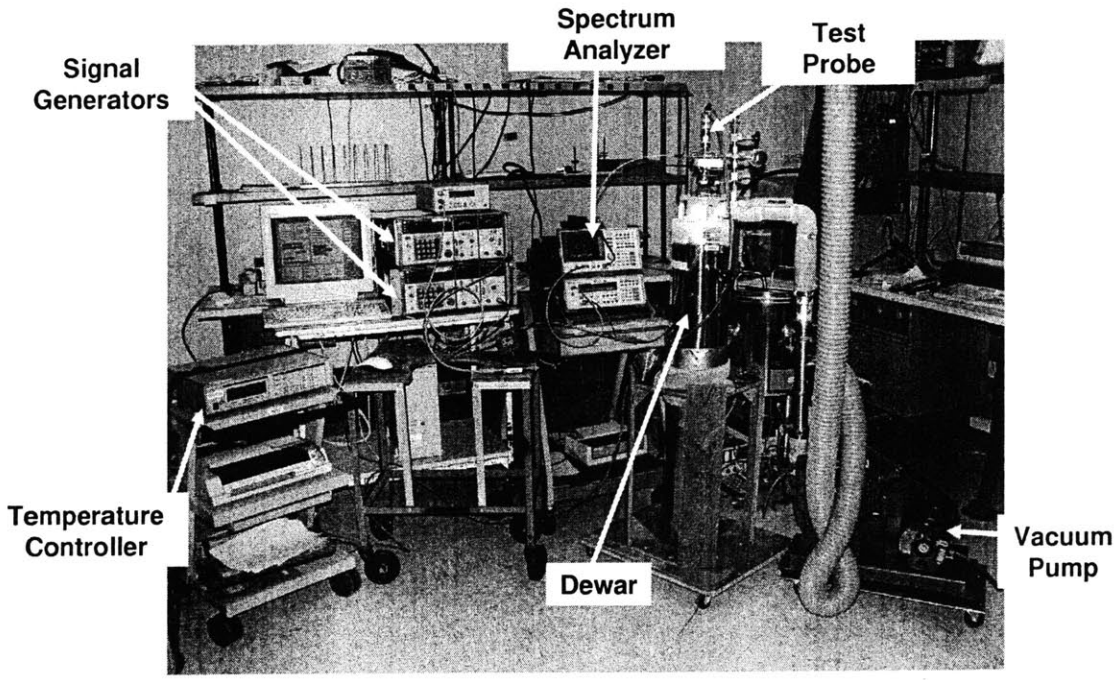

Figure 3-2: IMD setup photo

shows a schematic diagram of the Dewar and test probe immersed in liquid helium. The S-shaped stripline resonator is shown inside the test probe. The interior of test probe was filled with 1 atm helium gas at room temperature, to act as a heat exchange. The right side of Figure 3-3 is a magnified view of a resonator in an Au-plated copper package mounted on a copper thermal block, together with a diode temperature sensor and 2 resistive heaters. Input and output microwave power was transferred through the coax cables. If the temperature fluctuates the resonance frequency of the resonator changes due to the change in penetration depth. It turns out that the IMD measurements were quite sensitive to the resonance frequency shift. Figure 3-4 shows that the position of the input signals at f_1 and f_2 on the resonance curve and the resonance frequency shift as a result of temperature drift. After the resonance frequency is shifted, the input signals at f_1 and f_2 are no longer near the peak of the resonance curve. As a result, the reduced level of the circulating current leads to a reduced IMD. So, the temperature must be controlled precisely. For example, the resonance frequency shift from PLD YBCO was measured to be 3.6 Hz / mK from

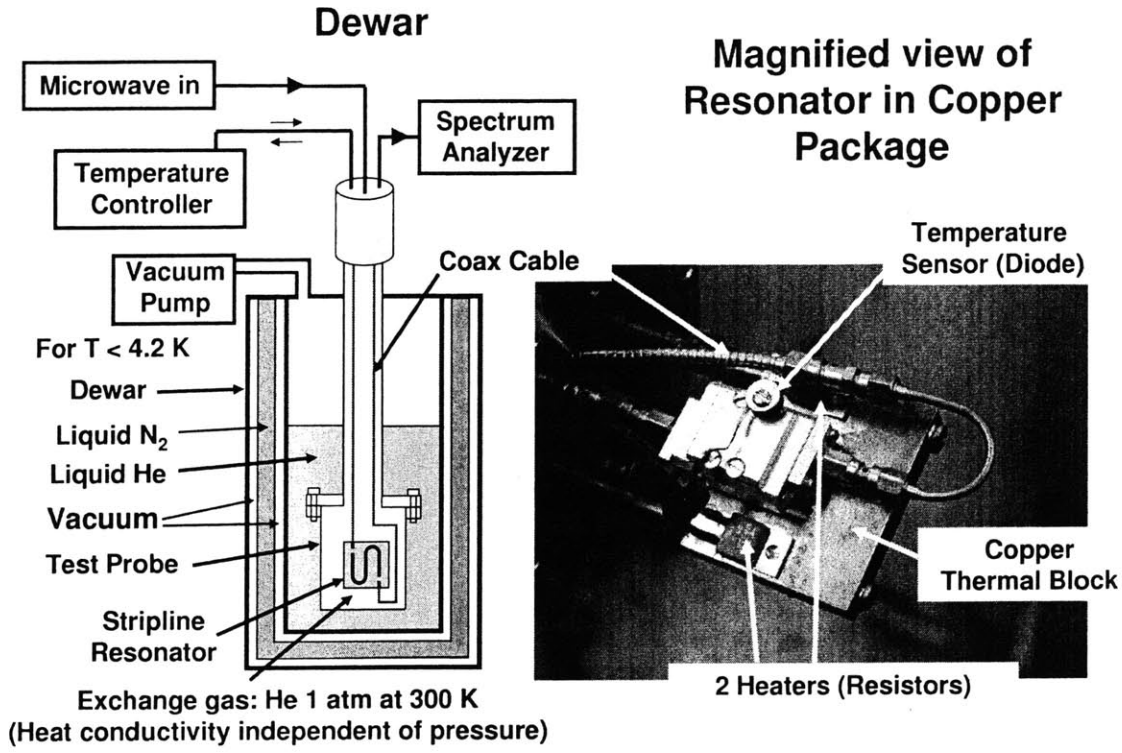

Figure 3-3: Dewar, test probe and resonator package

5 K down to 1.7 K. The smallest $\Delta f = f_2 - f_1$ used in this temperature range was 300Hz. So, the temperature change ΔT corresponding to 300 Hz is obtained as

$$\Delta T = 300\text{Hz} \times \frac{\text{mK}}{3.6\text{Hz}} \simeq 83.3\text{mK} \tag{3.6}$$

Therefore, the temperature drift of the device must be less than 83.3 mK. In our study, a precise temperature was achieved through feedback control using a sensor, two heaters, and temperature controller adopting P, I, and D parameters. The P term is a gain factor of the feedback control loop. If it is too high, the system will oscillate. The I term is an integrator term and D term is a derivative term of feedback control loop. I and D terms work in different ways in controlling temperatures. The achieved temperature drift was from 0.5 mK to 5 mK. As a result, we were able to measure very precise IMD values. Table 3.2 shows the definitions, ranges, and roles of P, I and D parameters.

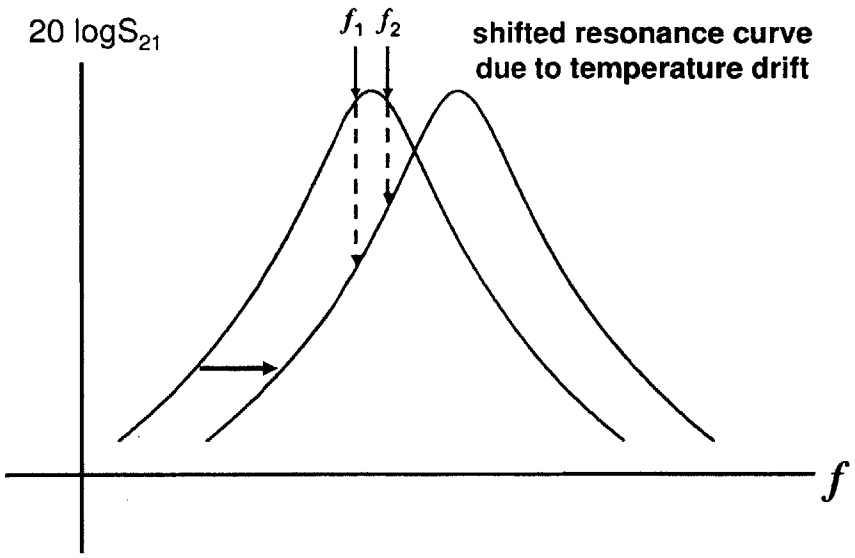

Figure 3-4: Temperature instability shifts the resonance curve. Input frequencies f_1 and f_2 are no longer near the peak of the shifted resonance curve.

	definition	range	if too large	if too small
P	gain factor	0.1-1000	oscillation	slow response
I	integrator term (sec)	0.1-10000 (sec)	slow response	sensitive to noise
D	derivative term (sec)	0-1000 (sec)	sensitive to noise	slow response

Table 3.2: P, I, and D parameters of temperature controller.

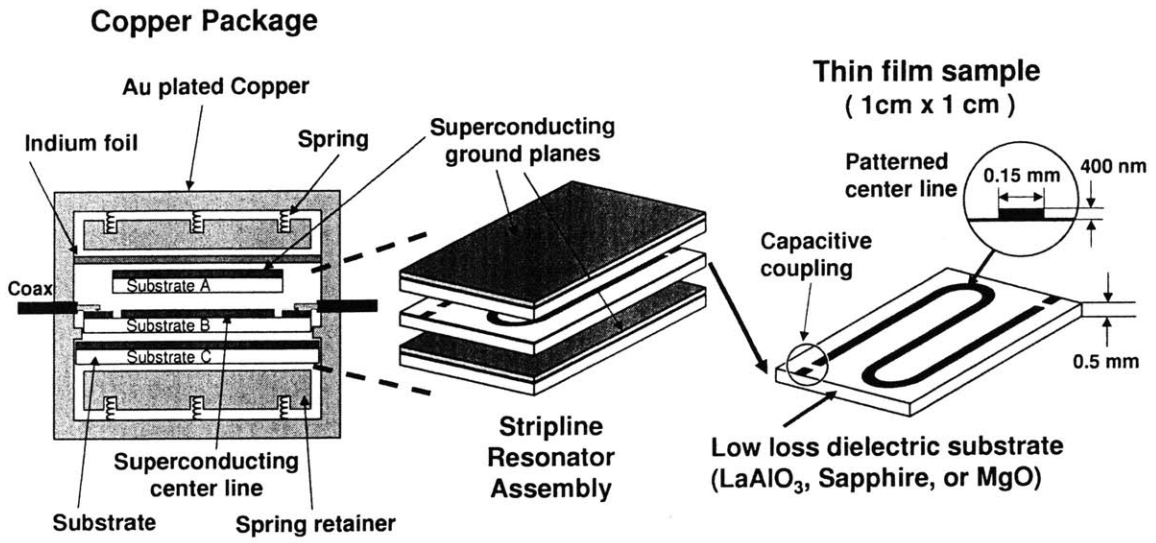

Figure 3-5: Stripline resonator used for measurement of the surface impedance Z_s and intermodulation distortion. The gaps between ground planes and substrate are shown for clarity. In practice there is no gap.

Figure 3-5 shows the $\lambda/2$ transmission line resonator inside an Au-plated copper package with S-shaped thin-film sample inside. The stripline resonator is enclosed by upper and lower superconducting ground planes. It has very low loss and consequently very high quality factor Q due to minimization of the radiation loss. A stripline resonator was also used since it is a planar transmission line which is compatible with microwave integrated circuitry. As shown in Figure 3-5, our stripline was made by etching the center conductor on a substrate B, and then placing two grounded substrates A and C of the same thickness over and under the substrate B. The substrate size was 1 cm x 1 cm x 0.5 mm. Standard photo lithography and wet etching were used to pattern the films [42, 43]. The cross section of the superconducting center conductor was either 0.15 mm x 400 nm or 0.15 mm x 350 nm.

We model the stripline resonator as a TEM waveguide and assume that there is very little interaction between meandering centerline segments since the line sep-

aration is large compared with the substrate thickness. The two superconducting ground planes are shorted through the copper package and the spacing is less than $\lambda_g/4$ where λ_g is the wavelength propagating inside the dielectric substrate. So, the higher-order TM and TE modes are suppressed. The fundamental mode of operation is TEM which is a propagation of a plane wave. The electric field is perpendicular to the propagation direction. The length ℓ of the superconducting meandering center line used was 2 cm. The resonance frequency f_o is determined by the relationship

$$\ell = \frac{\lambda_g}{2} = \frac{c}{2\sqrt{\varepsilon_r} f_o} \tag{3.7}$$

where c is speed of light and ε_r is the relative dielectric constant of the substrate used. The ε_r is 23.5 for $LaAlO_3$, 10.6 for sapphire and 11.1 for MgO. So, the resonance frequencies for $LaAlO_3$, sapphire, and MgO were 1.5 GHz, 2.3 GHz, and 2.25 GHz, respectively. The microwave power was transferred in and out of the sample through a capacitive coupling. The weak capacitive coupling acts like an open end. Because of the open end nature of resonator, the electric field is maximum at both ends, and the magnetic field and current are maximum in the middle of the center-conductor line for the fundamental mode.

3.2 Background

3.2.1 Parallel equivalent resonant circuit model

The parallel equivalent-circuit model of the stripline resonator, including the source and the load is shown in Figure 3-6. We measured the transmission coefficient S_{21} using a vector network analyzer. The S_{21} is found by driving the input port with an incident wave and measuring the transmitted wave amplitude to a 50-Ω load. Another important parameter to describe a resonator is the quality factor Q which is a measure of the loss of a resonant circuit. The definition is

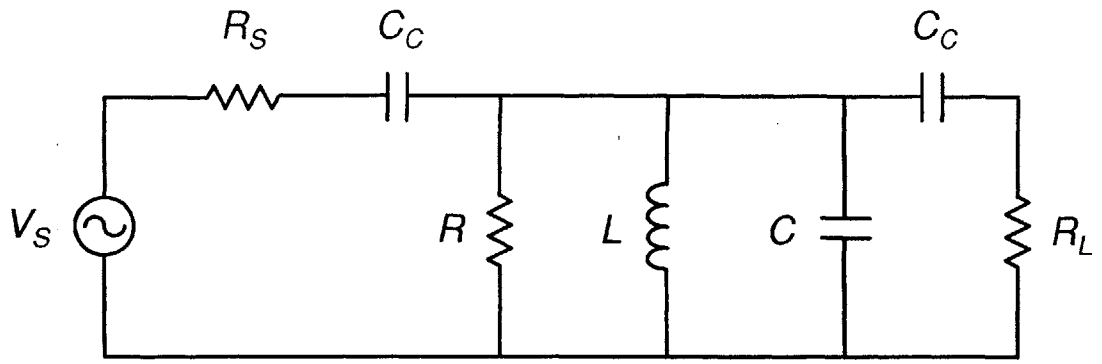

Figure 3-6: Parallel equivalent resonant circuit model of the stripline resonator is shown. V_S is the signal source, C_C the coupling capacitance, R_S the source resistance, R_L the load resistance. R, L, and C describes the resistance, the inductance, and capacitance of the stripline resonator used.

$$Q = \omega_o \frac{\text{average energy stored}}{\text{energy loss/sec}} = \frac{f_o}{\Delta f_{3dB}}, \tag{3.8}$$

where $\omega_o = 2\pi f_o$ is the angular resonance frequency,

$$f_o = \frac{1}{2\pi\sqrt{LC}} \tag{3.9}$$

the resonance frequency, L the inductance, C the capacitance in Figure 3-6, and Δf_{3dB} = 3 dB bandwidth.

Figure 3-7 shows the resonance curve and defined parameters.

Mathematically, the resonance curve is given by the Lorentzian distribution as

$$L(f) = \frac{\Delta f_{3dB}/2}{\pi[(f - f_o)^2 + (\Delta f_{3dB}/2)^2]}. \tag{3.10}$$

Any resonance circuit is inevitably coupled (loaded) to an external circuit to transfer power in and out. Therefore, the actual loaded quality factor Q_L of a resonant circuit is expressed as

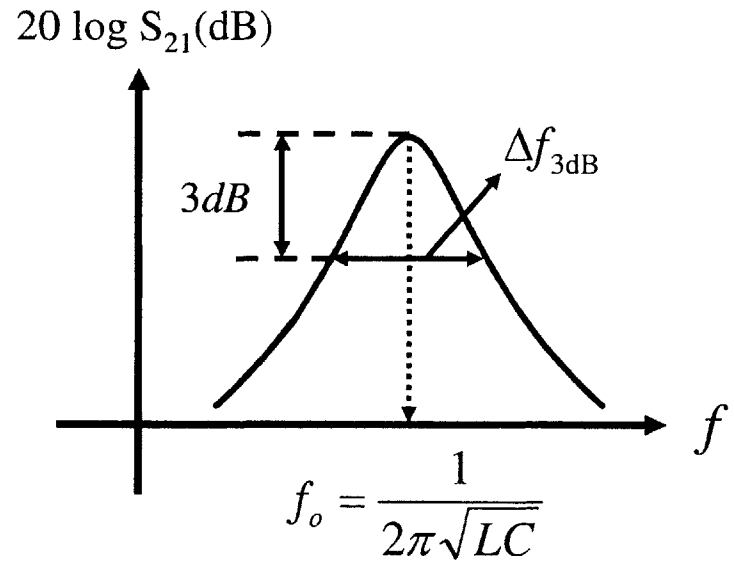

Figure 3-7: Resonance curve

$$\frac{1}{Q_L} = \frac{1}{Q_o} + \frac{1}{Q_D} + \frac{1}{Q_{ext}}, \tag{3.11}$$

where Q_o is the unloaded quality factor due to losses in the superconductor, Q_D is the quality factor representing dielectric loss, and Q_{ext} is the quality factor due to external coupling loss. The physical meaning of the equation 3.11 is that total loss = superconductor loss + dielectric loss + energy loss due to external coupling. The loss for the dielectrics used here is very low ($1/Q_D \simeq 0$). So, when we reduce energy loss due to external loading by weakly coupling ($1/Q_{ext} \simeq 0$) the above equation 3.11 becomes $1/Q_L \simeq 1/Q_o$. In practice $1/Q_{ext} > 0$, so a small correction was needed to obtain Q_o. In our study, Q_L and f_o were measured as a function of input power at different temperatures from 1.7 K to near T_c. Then, Q_L was converted to Q_o using [44]

$$Q_o = Q_L \frac{1}{1 - |S_{21}|} \tag{3.12}$$

where $|S_{21}| = \sqrt{P_L/P_o}$ is transmission coefficient, P_o the available power from the

source and P_L is the power delivered to the load.

This relationship holds when the coupling for both input and output is the same [44].

The insertion loss IL is defined as

$$IL = 10\log(\frac{P_o}{P_L})dB = -20\log(S_{21})dB \tag{3.13}$$

3.2.2 Extraction of the surface resistance and reactance

Whenever most of the current flows near the surface, the loss is concentrated on the surface. So, it has been a general practice to use the surface impedance concept. The penetration depth in a superconductor and the skin depth in a metal are used to specify how close the current flows from the surface. The surface impedance Z_s in superconductor is given by equation 1.5. To get R_s and X_s, the quality factor and the resonance frequency were measured as a function of input power at different temperatures. Figure 3-8 shows a typical f_o vs temperature plot. The sample was the high quality PLD YBCO on $LaAlO_3$ shown as No. 1 in Table 3.1.

The solid line is a least-squares fit to the data using

$$f_o(T) = f_o(T_o)\sqrt{\frac{L[\lambda(T_o)]}{L[\lambda(T)]}} \tag{3.14}$$

where T_o is the reference temperature and the inductance per unit length was obtained by integrating over the cross section of the line as

$$L(\lambda) = \frac{\mu_o \int_s (H^2 + \lambda^2 j^2(x,y))dS}{(\int_s j dS)^2} = \frac{\mu_o \int_s (H^2 + \lambda^2 j^2(x,y))dS}{I^2} \tag{3.15}$$

and the penetration depth

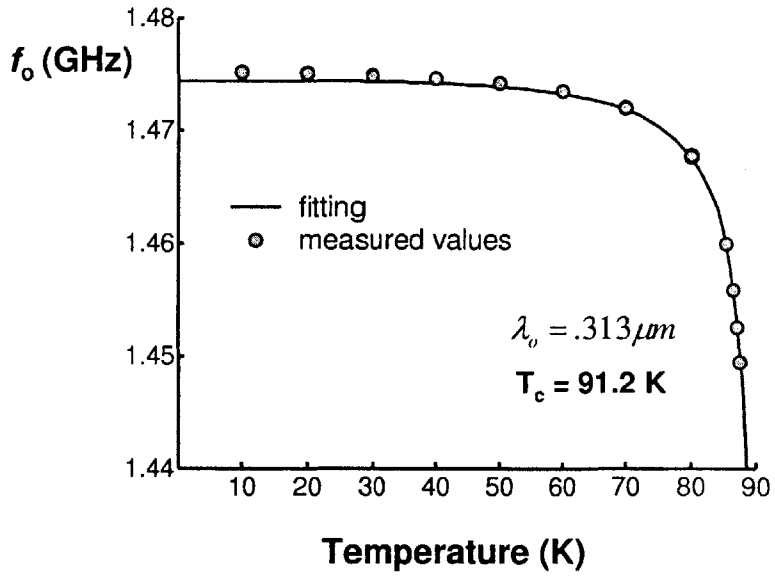

Figure 3-8: The resonance frequency vs temperature for the high quality PLD YBCO on $LaAlO_3$ shown as No. 1 in Table 3.1. The circles are measured values and line is fitted values with $\lambda_o = 0.313$ μm, $T_c = 91.2$ K.

$$\lambda(T) = \frac{\lambda_o(0)}{\sqrt{1-(T/T_c)^4}} \tag{3.16}$$

from the two fluid model. In equation 3.15, $j(x,y)$ was obtained from [45], $dS = dxdy$, and S is the cross section of the line.

Fitting process gave $\lambda_o(0) = 0.313$ μm and $T_c = 91.2$ K.

Now, we have all necessary parameters: the measured unloaded quality factor Q_o from equation 3.12, f_o from Figure 3-8, $L(\lambda)$ computed from equation 3.15, and $\lambda(T)$ with $\lambda_o(T)$ and T_c from equation 3.16. Then, R_s and X_s are obtained following the procedures in [46, 47]. The unloaded Q_o is given for the parallel resonance circuit shown in Figure 3-6,

$$Q_o = \frac{\omega_o L}{R} \tag{3.17}$$

Substituting Q_o, ω_o, and L into equation 3.17 gives R the resistance per unit length. Two fluid model [2] says that the conductivity of the superconductor is given by

$$\sigma_s = \sigma_1 - j\sigma_2 = \frac{n_{qp}e^2\tau}{m} - j\frac{1}{\omega\mu_o\lambda^2} \simeq \frac{n_{qp}}{n}\sigma_n - j\frac{1}{\omega\mu_o\lambda^2}, \tag{3.18}$$

where $n_{qp} = n - n_s$ is the number density of quasiparticles, n the total density of conduction electrons, n_s the number density of superelectrons, τ the average quasiparticle relaxation time, m the electron mass, and σ_n is the conductivity of the normal state. σ_2 is obtained by substituting λ into the imaginary part of equation 3.17. The loss in the superconducting lines is defined by

$$\frac{1}{2}R|I|^2 = \frac{1}{2}R|\int_s jdS|^2 = \frac{1}{2}\int_s \sigma_1|\vec{E}|^2dS = \frac{1}{2}\int_s (\frac{\sigma_1}{\sigma_1^2+\sigma_2^2})|j|^2dS \simeq \frac{1}{2}\int_s (\frac{\sigma_1}{\sigma_2^2})|j|^2dS \tag{3.19}$$

where I the current, $j = j(x,y)$ the current density distribution, S the cross section of superconductor, and $\vec{E}$ is the electric field. The last relationship in equation 3.19 holds when $\sigma_1 << \sigma_2$, which holds for superconductors.

Substituting R, σ_2, and the current density j into equation 3.19 gives σ_1. Finally, the surface resistance R_s is given by $\omega^2\mu^2\sigma_1\lambda^3/2$ from equation 1.5. The imaginary part X_s is given by also in equation 1.5. But, $\Delta X_s(T)$ will be computed rather than X_s since the change in X_s is very small. Then, $\Delta X_s(T)$ is obtained by $\omega_o\mu_o\Delta\lambda$ where

$$\Delta\lambda(T) = \frac{\lambda_o(0)}{\sqrt{1-(T/T_c)^4}} - \frac{\lambda_o(0)}{\sqrt{1-(T_o/T_c)^4}}. \tag{3.20}$$

The R_s and X_s extraction explained in this section was done for all films used in this thesis research.

3.2.3 IMD Normalization

The IMD power was measured as a function of temperature and output power using various resonators. The IMD power was normalized to compare the material properties of the various resonators and to account for $Q(T)$ and $IL(T)$ in each. This section shows how IMD power was normalized. The IMD generation in the resonator will be shown using the equivalent circuit in Figure 3-9.

The circulating current at f_1 and f_2 in resonator is [47]

$$|I^1_{cir}| = \sqrt{\frac{4Q_o r_v(1-r_v)P^1_{in}}{\pi Z_o}}, \tag{3.21}$$

where I^1_{cir} is circulating current at fundamental frequencies f_1 and f_2, r_v^2 is P^1_{out}/P^1_{in}, P^1_{in} the input power at f_1 and f_2, P^1_{out} output power at f_1 and f_2, and Z_o characteristic impedance of resonator. The circulating power at f_1 and f_2 inside resonator is given by

$$P^1_{cir} = |I^1_{cir}|^2 Z_o = \frac{4Q_o r_v(1-r_v)P^1_{in}}{\pi}. \tag{3.22}$$

Here, we assumed the uniform current distribution in the resonator. The IMD power due to the nonlinear inductance is discussed in [48, 49]. At low power, the nonlinear part of the penetration depth has a j^2 dependence as shown in Figure 2-5. At higher power, the nonlinear part of the penetration depth has $|j|$ dependence as in Figure 2-5. The nonlinear part of the inductance is proportional to the nonlinear part of the penetration depth [45]. The $|j|$ dependence carries over to I and consider the power exponent x as a general case.

Let the nonlinear inductance be

$$L = L_o + \Delta L = L_o + L_2 I^x \tag{3.23}$$

and the nonlinear penetration depth be

$$\lambda = \lambda_o + \Delta\lambda = \lambda_o + \lambda_2 I^x \tag{3.24}$$

where L_2 is a nonlinear inductance coefficient proportional to λ_2, I the circulating current in the resonator, and x is an exponent to the current I ranging from 1 to 2. Then, the voltage V_L across the nonlinear inductance ΔL is

$$V_L = j\omega\Delta L I = j\omega L_2 I^x I = j\omega L_2 I^{x+1} \tag{3.25}$$

We present here the result for P_{out}^{IMD} modified from [48, 49] since the general power component x is used in this thesis.

$$P_{out}^{IMD} = \omega^2 L_2^2 4^x \frac{r_v^{x+2}(1-r_v)^{x+2}Q_o^{x+2}}{\pi^x Z_o^{x+2}} P_{in}^{x+1} \tag{3.26}$$

Other authors derived similar equations in [20, 50]. Now, if we substitute equation 3.22 into equation 3.26

$$P_{out}^{IMD} \propto \omega^2 L_2^2 \frac{\pi}{4Z_o^{x+2}} Q_o r_v (1-r_v)(P_{cir}^1)^{x+1} \tag{3.27}$$

ω^2, Q_o and r_v change depending on the temperature, input power levels and resonator used. The nonlinear inductance coefficient L_2 is sample-specific and independent of ω, Q,and r_v.

After rearranging, the normalized P_{norm}^{IMD} is defined as

$$P_{norm}^{IMD} = \frac{P_{out}^{IMD}}{\omega^2 Q_o r_v (1-r_v)} \propto L_2^2 \frac{(P_{cir}^1)^{x+1}}{Z_0^{x+2}} \tag{3.28}$$

Now, the P_{norm}^{IMD} is independent of Q_o, insertion loss and resonance frequency shift for

a given P_{cir}^{1}. The slope of $\log(P_{norm}^{IMD})$ as a function of log(circulating power) is $x+1$.

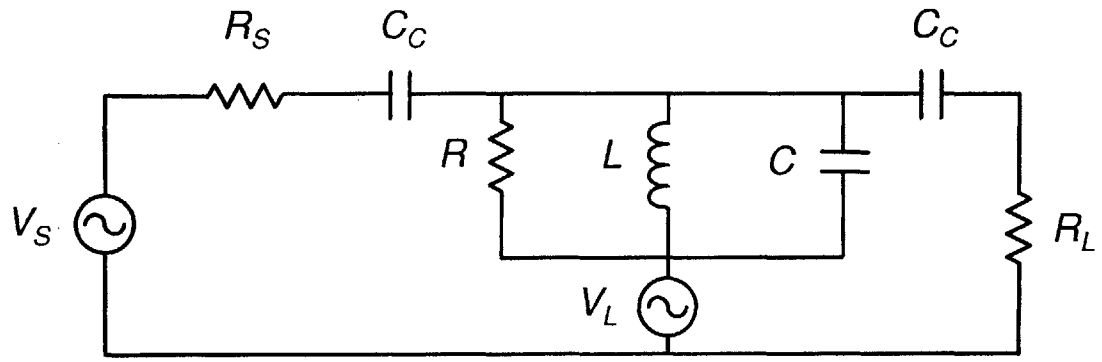

Figure 3-9: Parallel equivalent resonant circuit model of the stripline resonator is shown. V_S is the signal source, C_C the coupling capacitance, R_S the source resistance, R_L the load resistance. V_L the voltage source due to the nonlinear inductance. At low temperatures, the nonlinear voltage mainly comes from the nonlinear inductance. R, L, and C describes the resistance, the inductance, and capacitance of the stripline resonator used.

Chapter 4

Verification of d-wave symmetry using microwave intermodulation distortion

The pairing symmetry in high-T_c superconductors has been controversial. New experimental evidence from phase-sensitive tests, however, strongly supports a predominantly d-wave symmetry. So, this issue is quite settled down. Tsuei and Kirtley [25] wrote an excellent review article on this issue. Yet, proving d-wave symmetry by microwave measurements has been evading many experimentalists' efforts. Here, we report the first convincing evidence of d-wave symmetry in high-T_c superconductors using microwave intermodulation measurements.

4.1 IMD results from YBCO

Figure 4-1 shows the superconducting resonator on the dielectric substrate. The current flows along the conductor. In the left side of the Figure 4-1, there is a gap function for d-wave symmetry in momentum space. $\vec{v}_s$ is the superflow velocity and α_c is the wedge angle for the occupied quasiparticles. We don't know the directions of P_x and P_y axis in the superconductor. In addition, because of the weak coupling at the end of the superconducting line, there is a current maximum in the middle

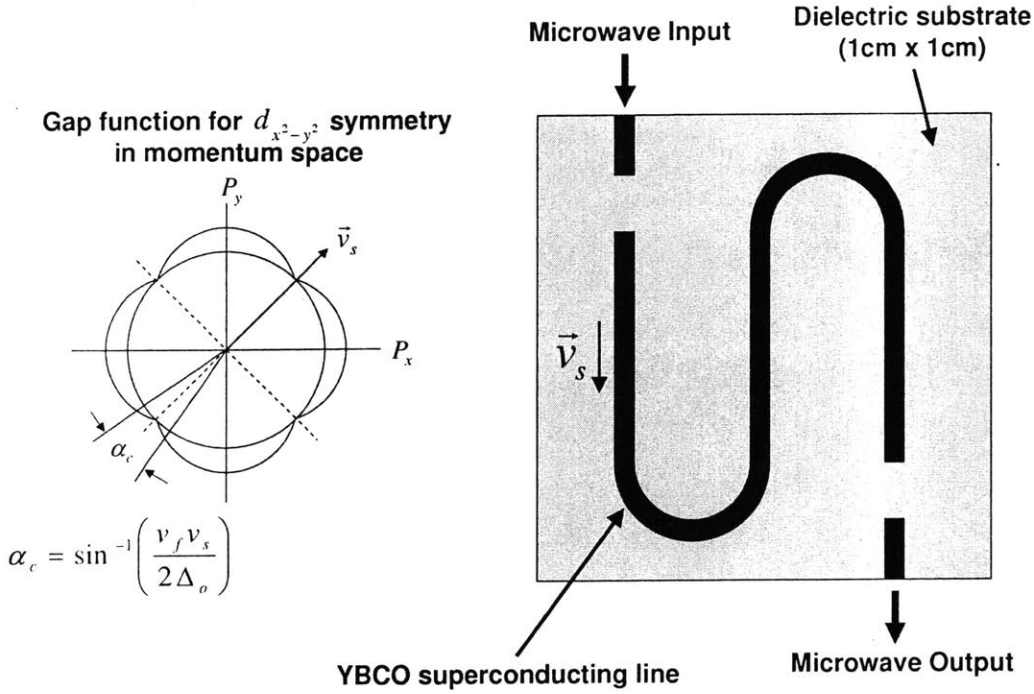

Figure 4-1: Average angular response in momentum space

of the line. So, the IMD response we measured is an average sampling from the continuously changing directions of the current, weighted more in the middle of the superconducting line.

Figure 4-2 shows the temperature and power dependence of IMD in our measurements. The unit dBm is defined as $10\log(\text{power(W)}/10^{-3}\text{W})$. We measured many temperatures, but only measurements at 1.75 K, 5 K, 50 K and 80 K are shown for clarity

The IMD increase at low temperature and low power is evident. At 1.75 K, the lowest temperature measured, the IMD was the highest at low and intermediate power levels. At this temperature, the slope was approximately 3 at low power indicating that $x = 2$ in equation 3.23 and equation 3.24. According to Dahm and Scalapino, the quadratic field dependence of the penetration depth applies to this region. The slope was 1.43 at medium power. The linear field dependence of the penetration

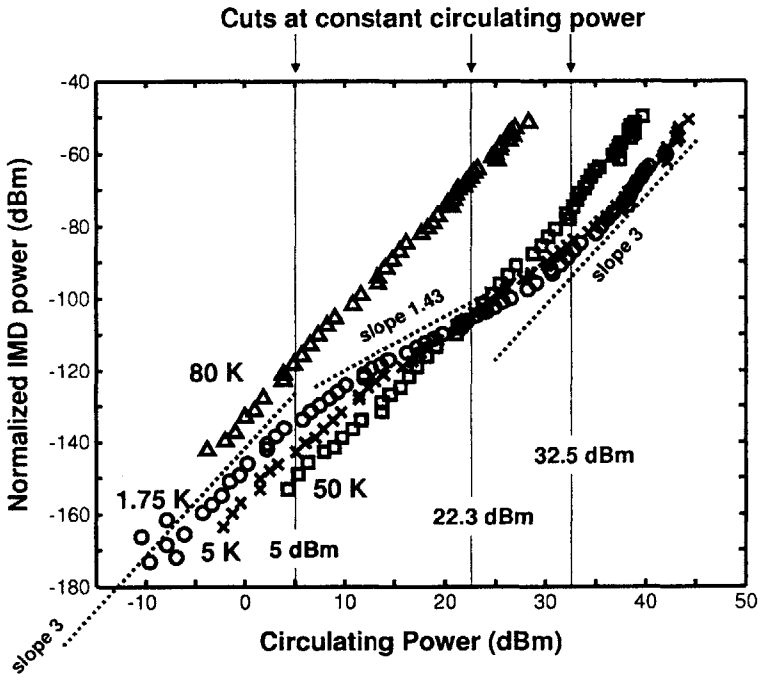

Figure 4-2: IMD vs Power and Temperature for PLD undoped YBCO on LAO

depth corresponds to this region. Equation 3.23 and equation 3.24 with $x = 0.43$ is for this region.

At the highest power, the slope was also 3. The Dahm and Scalapino theory did not address this region. As the temperature increases, the slope of IMD power approaches 3. At 80 K, the slope is 3 across all power levels. It seems that the IMD generation mechanism at 80 K is different from that of low temperatures. This region resembles the high power region at low temperatures.

Figure 4-3 shows the measured IMD as a function of temperatures at the three different circulating power cuts as shown in Figure 4-2. The IMD increases as the temperature decreases at the low circulating power $P_{cir}^{1} = 5$ dBm. At the medium circulating power $P_{cir}^{1} = 22.3$ dBm, IMD is constant as temperature decreases within experimental errors. At high circulating power $P_{cir}^{1} = 32.5$ dBm, IMD decreases as temperature decreases. It is evident there is a crossover in temperature behavior at

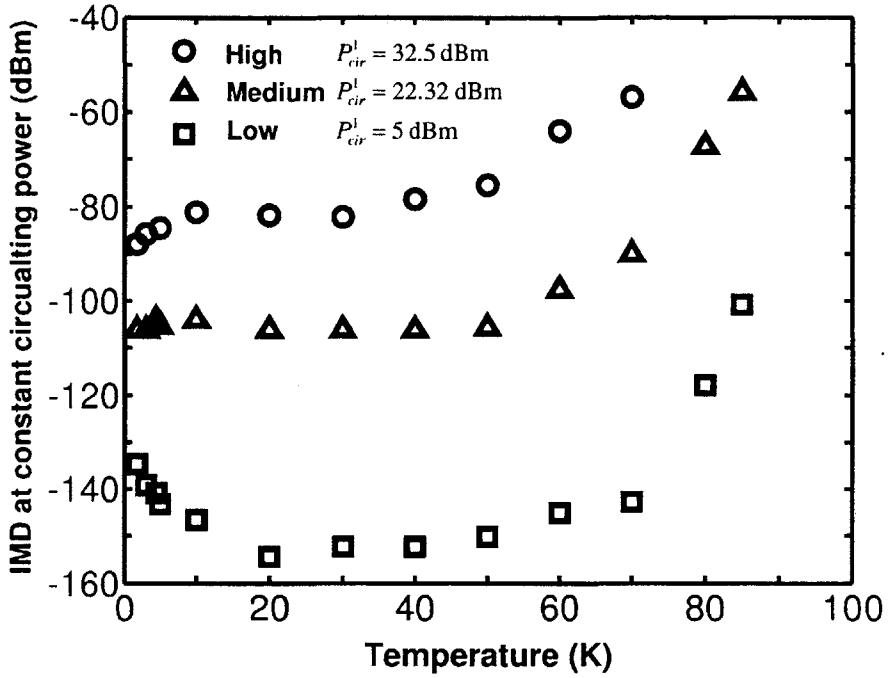

Figure 4-3: IMD vs Temperature at three different circulating powers

$P_{cir}^{1} \simeq 22.3$ dBm.

4.2 The temperature dependence of IMD power at low temperatures

Figure 4-4 shows the temperature dependence of the IMD at low temperature and at 5 dBm circulating power. We obtained the $1/T^2$ dependence predicted from $b^2(T)$ by Dahm and Scalapino. $b^2(T)$ has one free parameter. It is shifted down to show the agreement more clearly. To expand the low T behavior, the log of the reduced temperature was plotted. The agreement of the temperature dependence is excellent. In Figure 4-5, the same data was plotted as a function of $1/T^2$. The confirmation of the temperature dependence of the IMD is very strong evidence of the intrinsic

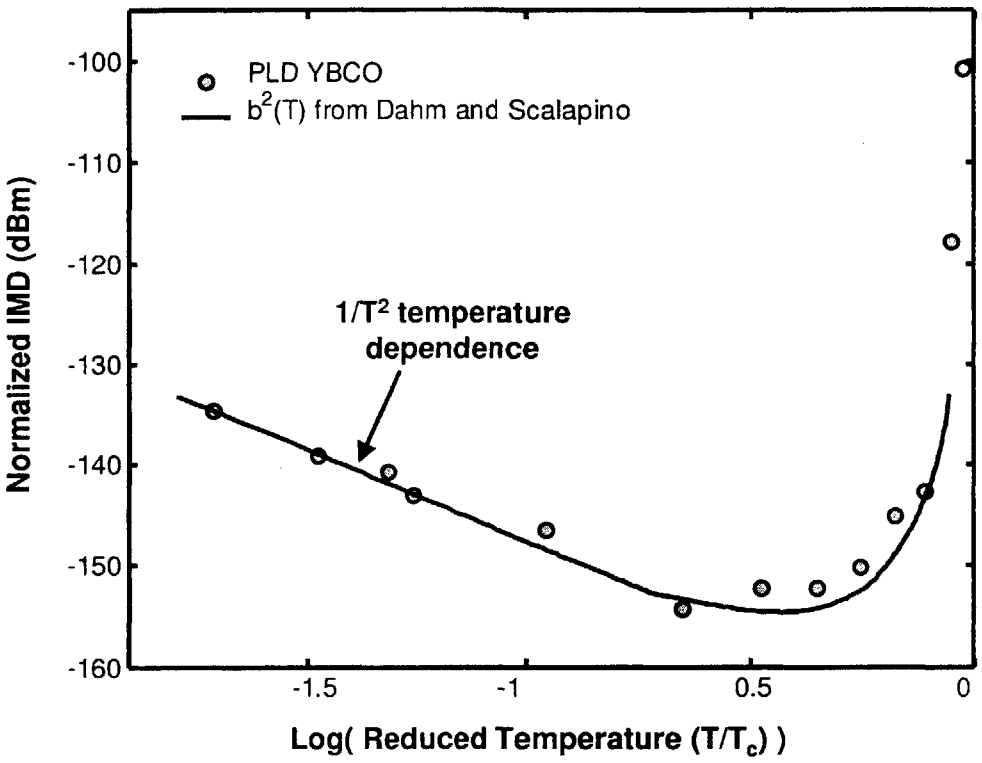

Figure 4-4: IMD vs $\log_{10}(T/T_c)$ compared with theory. PLD YBCO on $LaALO_3$ was used.

nature of IMD generation.

4.3 Effects of dopants, disorder

Figure 4-6 shows the IMD vs T/T_c for the films in Table 3.1. PLD YBCO showed the lowest level of IMD at the middle of temperatures. We obtained convincing evidence of an IMD increase at low temperatures with various samples of YBCO on $LaAlO_3$. High quality PLD YBCO on $LaAlO_3$ showed the highest IMD upturn. This IMD upturn is due to the increase in the nonlinear coefficient $b(T)$ of the quadratic current dependence of the penetration depth. The change in penetration depth correspond-

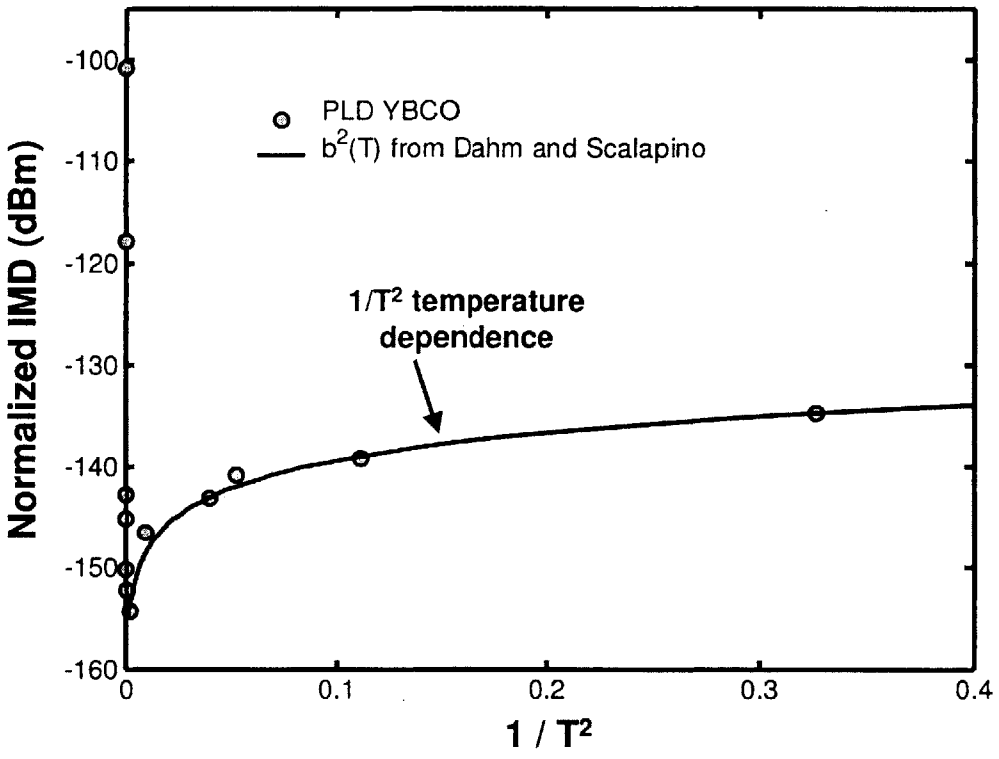

Figure 4-5: IMD vs $1/T^2$ compared with theory. PLD YBCO on $LaALO_3$ was used.

ing to the quadratic current dependent region is less than 0.01 nm at 1.7 K with high quality PLD YBCO on $LaAlO_3$. Refer to Figure 2-4. This explains why the direct measurements of the penetration depth change had been so difficult. Around 50 K, the IMD levels vary depending on dopants, disorder and defects in YBCO due to extrinsic contributions. The Ca doped YBCO raised the background IMD at the middle of the temperature range. In 6 % (not shown) and 30 % homogeneous Ca-doped YBCO, the low temperature IMD increase almost disappeared. Another finding is that Ni doped YBCO also has a similar dependence and increase comparable to the high quality PLD sample No. 1. In Ni-doped YBCO, the IMD is also comparable to the high quality YBCO sample No. 1 in the middle of the temperature range. Ni is a magnetic impurity; it is known to destroy the superconductivity in *s*-wave materials [51]. However, this data suggests that Ni does not destroy *d*-wave symmetry signature. Scanning tunnelling microscope experiments [52] also show that Ni preserves superconductivity and *d*-wave symmetry. Our IMD measurements showed that non-magnetic Zn has a stronger suppression of *d*-wave symmetry than Ni has. Our measurements also showed that the increased level of IMD in the middle of the temperature range in the Zn-doped sample. Zn locally destroys superconductivity as reported in [53]. It is consistent with the hypothesis that the pairing mechanisms for *d*-wave superconductor is magnetic unlike *s*-wave superconductor [54, 55].

YBCO on sapphire shows the highest level of IMD and a monotonic decrease towards 0 K. Maybe, epitaxially grown YBCO on sapphire has many defects and disorder because of mismatch in thermal expansion coefficient and lattice parameter between the YBCO and sapphire. YBCO grown by sputtering at Lincoln Laboratory shows a higher IMD at intermediate temperature than the PLD YBCO, probably due to the increased contribution from extrinsic origins. This sample does show an upturn and slope change in IMD vs power plot. We observe that the IMD has a tendency to converge to a universal value at 5 mK regardless of doping and defects due to the node singularity at 0 K as shown in Figure 4-7. IMD convergence at 5 mK also implies that the *d*-wave node is a true node. As the temperature decreases, the intrinsic effect becomes more evident in the case of *d*-wave superconductor.

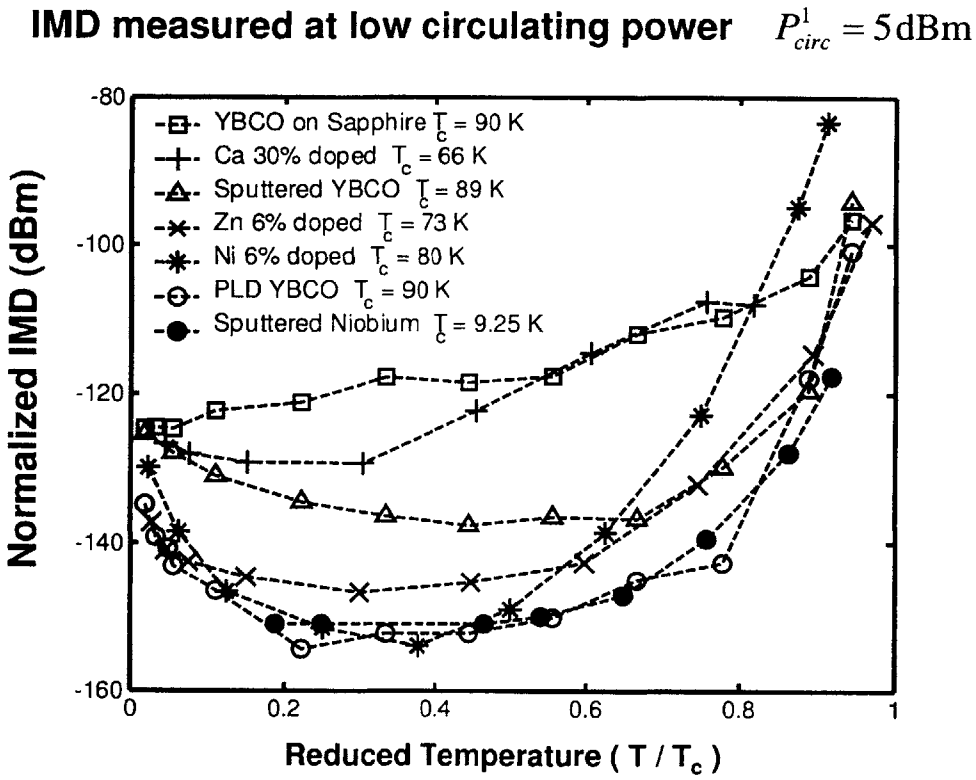

Figure 4-6: IMD vs reduced temperature for various films

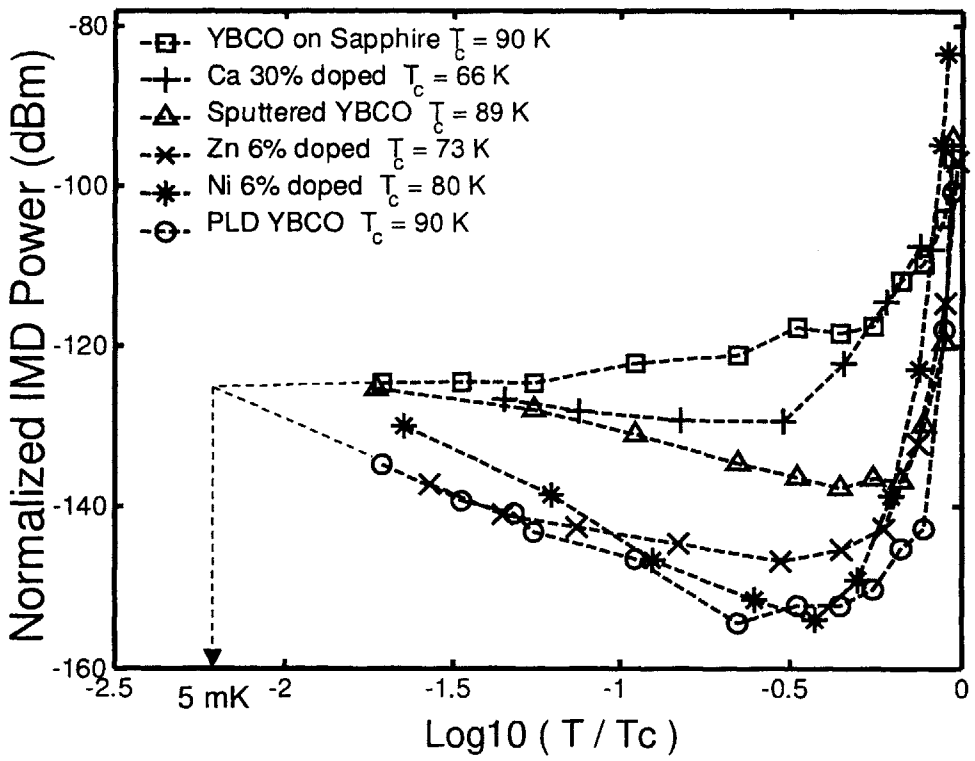

The 5 mK is very close to Node Singularity at 0 K.

Figure 4-7: IMD vs $\log_{10}(T/T_c)$ for various films. IMD converges at about 5 mK, which is very close to the node singularity at 0 K. This implies that d-wave node is a true node.

There is a similar tendency for the IMD to converge as T approaches to T_c due to the total depletion of the superelectrons at T_c.

4.4 IMD results from niobium for comparison

Theory predicts that IMD increases at low temperatures for d-wave superconductors and IMD decreases exponentially at low temperatures for s-wave superconductors. In this section we will verify the s-wave prediction with niobium on $LaAlO_3$. In addition, we will check if the substrate $LaAlO_3$ contributes to IMD. Figure 4-8 shows the normalized IMD measurements with the s-wave superconductor niobium [40] on $LaAlO_3$. The graph on the top side is plotted as a function of reduced temperatures. Even though the theoretical prediction says that IMD decreases exponentially in s-wave superconductors, the measured IMD becomes independent of temperatures below 4.3 K and deviates from theory at 6.7 K probably due to the extrinsic effects. This is polycrystalline niobium, but weak links should not be important since the Nb coherence length is long. This behavior is not well understood. We need more measurements with various Nb samples. The reduced temperature of Nb was not low enough to confirm that IMD does not increase at lower temperatures.

On the bottom side the IMD is plotted as a function of absolute temperatures. Here, IMD of Nb is constant where IMD of YBCO increases. We clearly see that the $LaAlO_3$ substrate is not a source of the IMD increase at low temperatures.

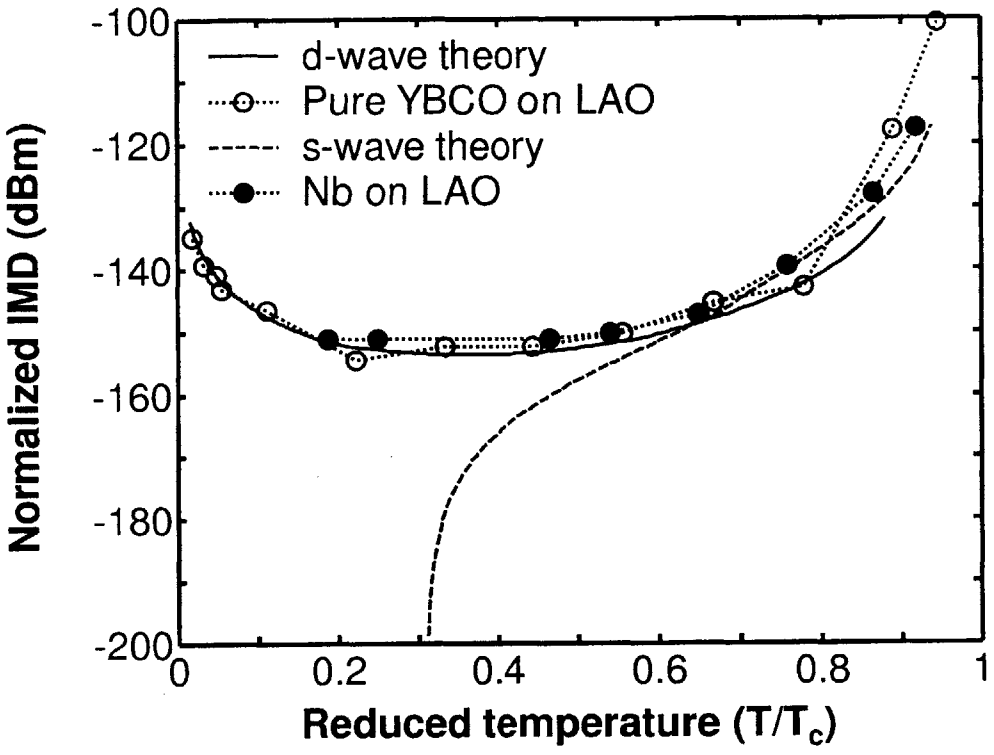

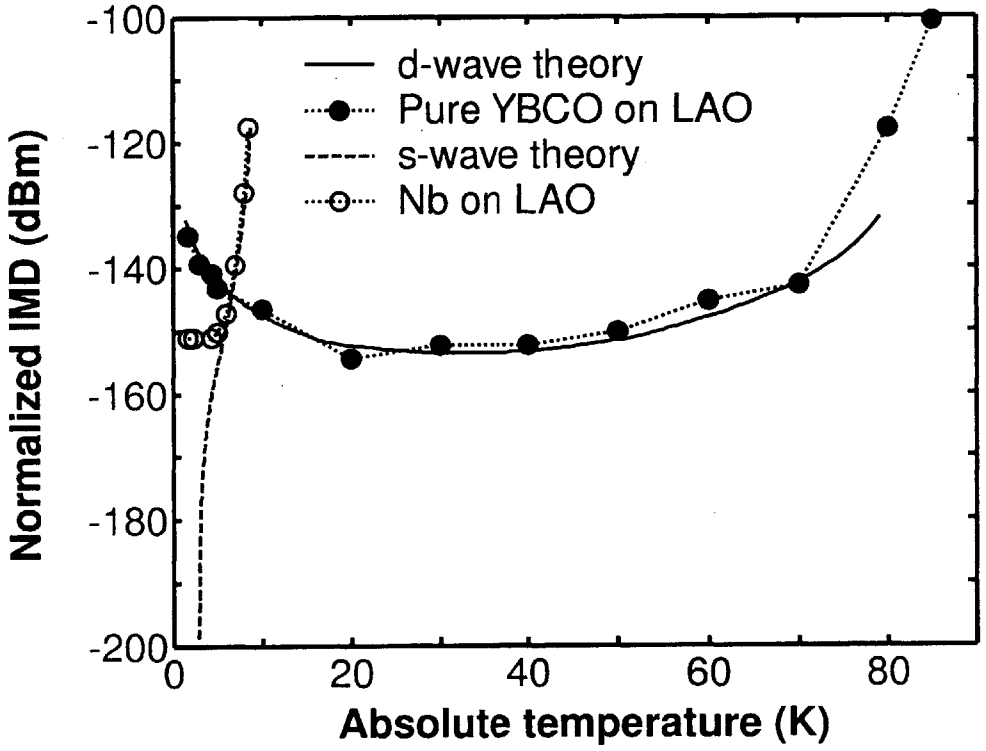

Figure 4-8: IMD vs Temperature with niobium

Chapter 5

Conclusions

We obtained convincing evidence of an IMD upturn at low temperatures with various samples of YBCO on $LaAlO_3$. High quality PLD YBCO on $LaAlO_3$ showed the highest IMD upturn. This IMD upturn is due to the increase in the nonlinear coefficient $b_\theta(T)$ of the quadratic current dependence of the penetration depth. The change in penetration depth corresponding to the quadratic current dependent region is less than 0.01 nm at 1.7 K with high quality PLD YBCO on $LaAlO_3$. This explains why the direct measurements of the penetration depth change had been so difficult. Furthermore, we were able to show the predicted temperature dependence $1/T^2$ in IMD at low temperatures in high-quality PLD YBCO on $LaAlO_3$. The confirmation of the $1/T^2$ temperature dependence is a strong evidence of the intrinsic nature of the IMD upturn. Other films do not agree with the $1/T^2$ dependence possibly due to extrinsic effects.

Dahm and Scalapino predicted that there is a crossover from j^2 to $|j|$ current dependence of the nonlinear superfluid density as the current increases. We showed that there is crossover from slope 3 (j^2 dependence) through slope 1.43 ($|j|^{0.43}$ dependence) to slope 3 (j^2 dependence) again. The j^2 dependence at the highest power is probably due to flux penetration above the lower critical field H_{c1}. At 80 K, the IMD shows the slope 3 across all power levels. It seems that IMD generation mechanism at 80 K is different from that of low temperatures.

Around 50 K, the IMD levels vary depending on dopants, disorder and defects

in YBCO due to extrinsic contributions. Epitaxially grown YBCO on sapphire has many defects and disorder because of the mismatch in thermal expansion coefficient and lattice parameter. The film on sapphire shows no upturn in IMD and only a monotonic decrease towards 0 K.

A closer look at the IMD vs temperature plot reveals that in all samples the IMD values converge to a single universal value towards 5 mK as T decreases regardless of dopants, disorder, defects in YBCO, and substrate used. This is explained by the fact that as temperature decreases, the singular behavior at the node dominates over the extrinsic contribution. Furthermore, the node singularity suggests the d-wave node is a true node. A similar converging trend is seen as T approaches T_c since the quasiparticles become totally depleted at T_c in this case. Niobium on $LaAlO_3$ does not show an IMD upturn. It rules out that the IMD increase is due to the $LaAlO_3$ substrate. Theory predicts that IMD from s-wave superconductor such as niobium decreases exponentially. Therefore, the temperature independence of the measured IMD from niobium at low temperatures suggests that this IMD is coming from extrinsic sources such as weak links [56]. Lower-temperature measurements down to 0.3 K using helium 3 cooler are desired to extend experimental verification at the further reduced temperatures.

Magnetic interactions and magnetic impurities destroy superconductivity in conventional s-wave superconductors [51]. But, our IMD measurements revealed that Ni-doped YBCO has an increase in IMD at low temperature that is a characteristic of d-wave symmetry. Our IMD measurements also showed that non-magnetic Zn has a stronger effect to suppress d-wave symmetry than Ni has. Our findings agree with scanning tunneling microscope results. They reported that Ni preserves superconductivity and d-wave symmetry [52]. Also, Zn locally destroys superconductivity [53]. It is consistent with the hypothesis that the pairing mechanisms for d-wave superconductor is magnetic unlike s-wave superconductor [54, 55].

Chapter 6

Future Studies

For further verification of d-wave signature, measurements on YBCO using a helium 3 cooler are desired for the reduced temperatures possible with such a system. To test the effects of thickness of superconducting film on d-wave signature, more sample measurements are needed. To confirm the Abrikosov vortex state, the careful computation of H_{c1} value are desired. Systemetic variation of dopants in YBCO is required to further verify the node singularity. IMD measurements with more Nb samples at lower temperatures are strongly desired to compare s-wave and d-wave signatures.

Appendix A

Investigation of the substrate effects on the time response of IMD generation

A.1 The Description of the off-the-resonance excitation Method

This experimental method investigates the IMD generation time scale τ_{IMD} of the nonlinearity [57] by varying $\Delta f = f_2 - f_1$ while keeping circulating powers P^1_{cir} and P^2_{cir} at f_1 and f_2 constant in the resonator. Also, this method will test the validity of the IMD generation model.

Here, we will introduce another time scale τ_{input} as follows. The current in the power combiner is expressed using trigonometric identity as

$$\cos(\omega_1 t) + \cos(\omega_2 t) = 2\cos(\frac{(\omega_2 - \omega_1)}{2}t)\cos(\frac{(\omega_2 + \omega_1)}{2}t) = 2\cos(\frac{\Delta\omega}{2}t)\cos(\omega_o t) \quad \text{(A.1)}$$

where the identical amplitudes for both signals were assumed. This is an amplitude

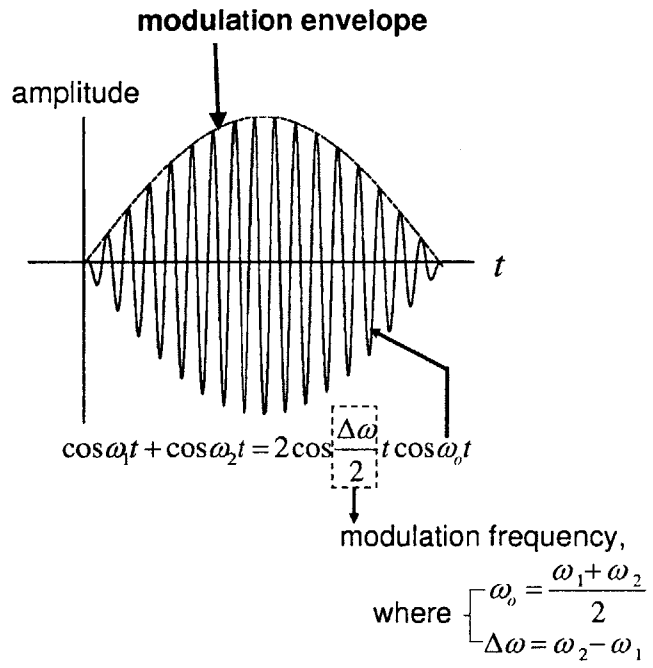

Figure A-1: modulation envelope

modulation by frequency $\Delta\omega/2$ and the carrier frequency is ω_o. Figure A-1 shows the modulation envelope and carrier frequency. The modulation time scale τ_{input} is defined as the reciprocal of the modulation frequency as

$$\tau_{input} = \frac{2}{\Delta\omega} = \frac{2}{2\pi\Delta f} = \frac{1}{\pi\Delta f} \tag{A.2}$$

Figure A-2 shows how τ_{input} decreases as Δf increases.

The left side of Figure A-3 shows how the input powers at f_1 and f_2 were applied on both sides of the resonance peak. As the $\Delta f = f_2 - f_1$ increases, the time scale τ_{input} decreases. If the IMD output power traces the Lorentzian resonance curve while varying $\Delta f = f_2 - f_1$ as shown here, $\tau_{IMD} \leq \tau_{input}$. We can say that the response time scale of the nonlinearity in the IMD generation is faster than the modulation time scale τ_{input}. The right side shows how the input powers at f_1 and f_2 were applied

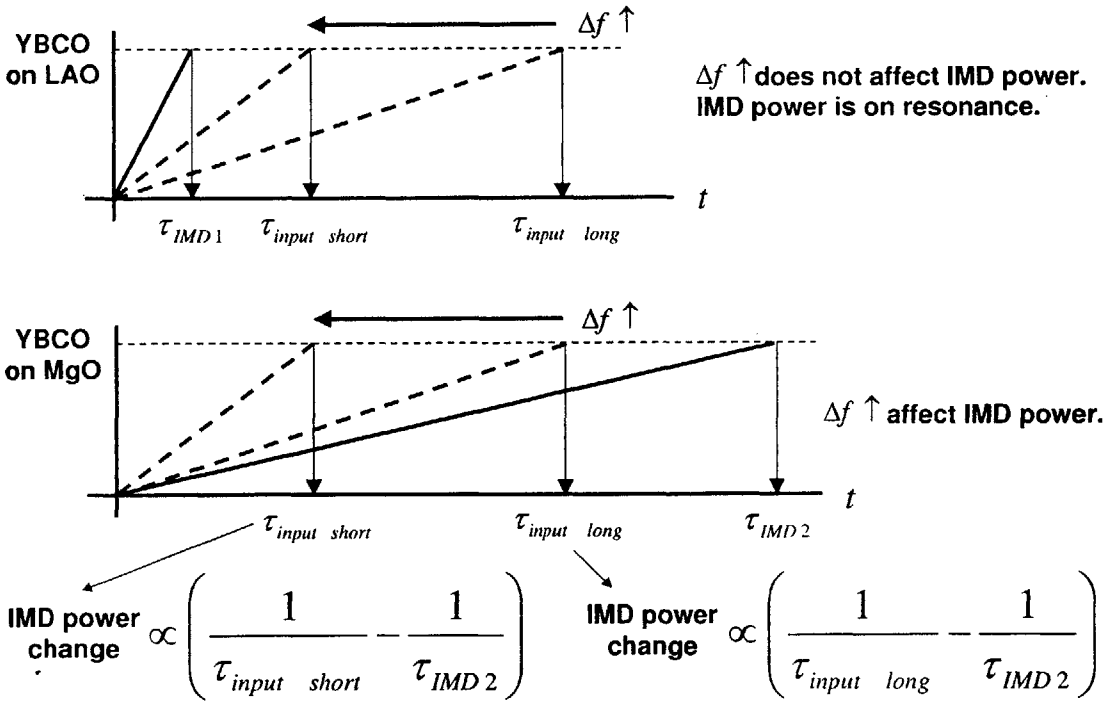

Figure A-2: Graphical representation of τ_{input} and τ_{IMD}

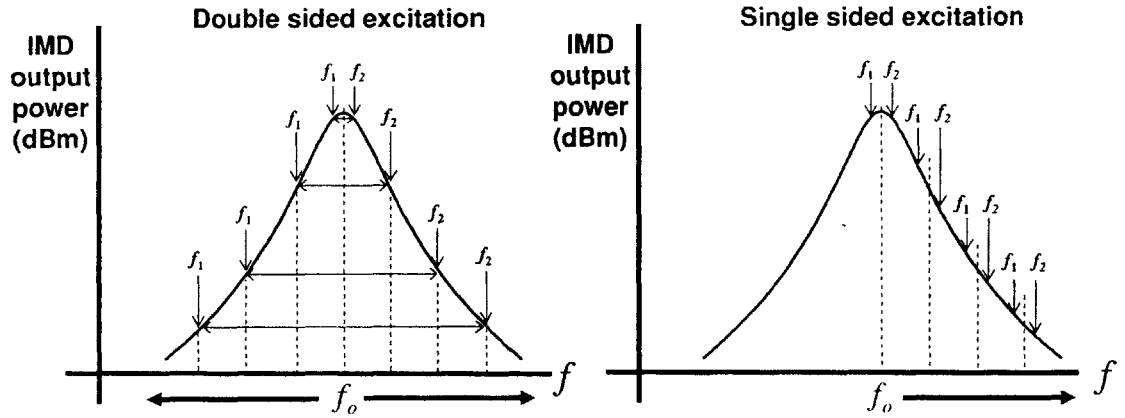

When IMD output power was not affected by τ_{input}, it traces the resonance curve.
$\because P_{out}^{IMD} \propto \left(P_{cir}^{1}\right)^3 \mathcal{L}(f)$ where $\mathcal{L}(f)$ is Lorentzian distribution function.

Figure A-3: Double sided vs Single sided off-the-Resonance excitation

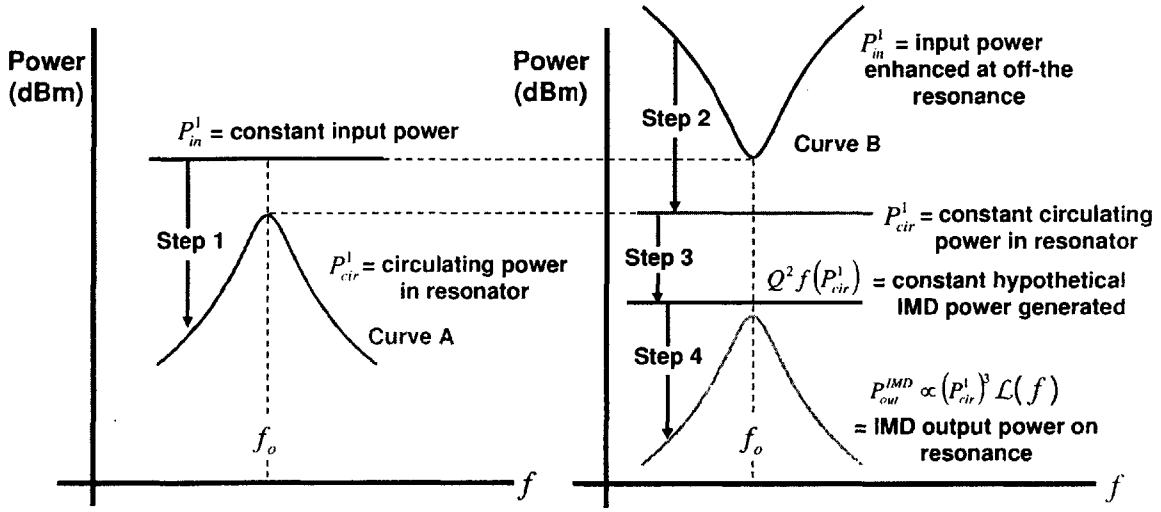

Step 1 and step 2: Fundamental input signal enters into resonator.
$\left|P_{in}^1 - P_{cir}^1\right|$ = constant at each off-the-resonance frequency. Therefore, Curve B is an upside down version of Curve A.

Step 3: IMD generation in YBCO.

Step 4: IMD output signal is on resonance and exactly traces Curve A in the absence of substrate effect. Experimentally verified.

Figure A-4: Off-the Resonance excitation to generate IMD

on only one side of the resonance peak. $\Delta f = f_2 - f_1$ is kept constant. The IMD output power in this case traces a Lorentzian resonance curve, too.

Figure A-4 shows the various power levels in and out of the resonator. In the left side of Figure A-4, when a constant input power P_{in}^1 is swept in frequency, the circulating power P_{cir}^1 in resonator traces the familiar Lorentzian resonance curve. Therefore, to keep a constant P_{cir}^1 as f_o is swept we must apply the input power P_{in}^1 that is the inverse version of the Lorentzian curve, which is the top curve in the right side in Figure A-4. Now, the constant circulating power P_{cir}^1 generates a constant hypothetical IMD power. In another words, the nonlinear voltage generator in equivalent circuit is constant. But, the circulating IMD power is governed by resonance phenomena. Thus, the measured output IMD power traces the resonance curve (the bottom curve in the right side).

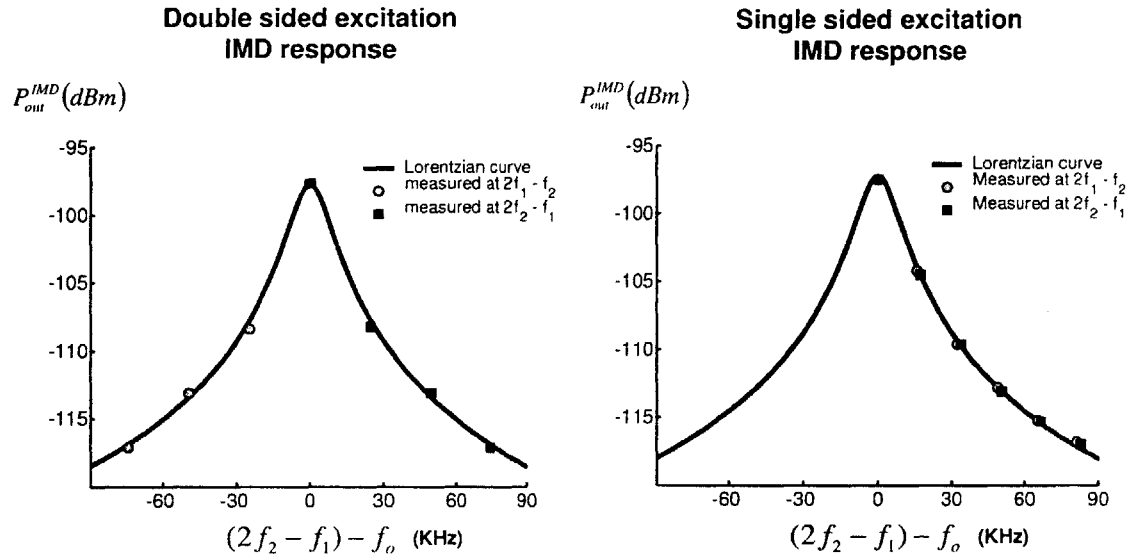

Figure A-5: IMD measurements by off-the-resonance excitation with YBCO on $LaALO_3$ at 5 K. For both plots, f_o=1.47330117 GHz, f_{3dB} = 16.5 KHz, and matching power = -51.6 dBm

A.2 Effects of $LaAlO_3$ on the time response of IMD generation

Figure A-5 shows the measurement data for YBCO on $LaAlO_3$. IMD power curve closely traces the Lorentzian resonance curve since $\tau_{IMD} \leq \tau_{input}$. This experiment not only explores the response time scale τ_{IMD} of IMD generation compared to modulation time scale τ_{input}, but also confirms that the IMD is indeed coming from the resonator. Other sources of IMD such as the spectrum analyzer would not show the frequency dependence that is observed.

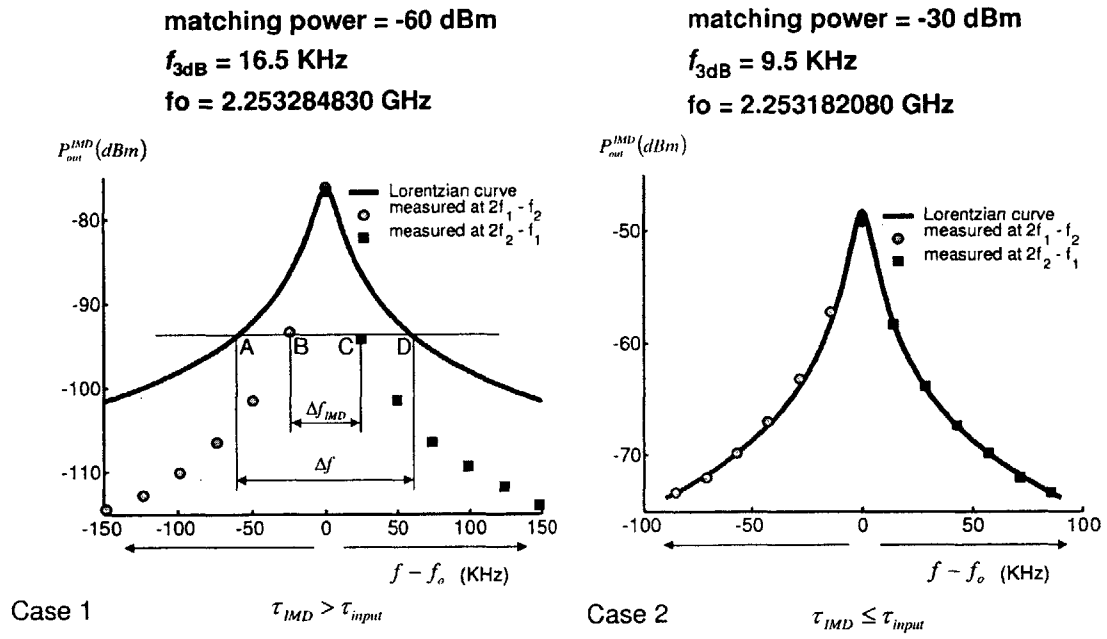

Figure A-6: IMD measurements by off-the-resonance excitation with YBCO on MgO at 5 K.

A.3 Effects of MgO on the time response of IMD generation

Figure A-6 shows the measurement data for YBCO on MgO at 5 K. At this temperature, YBCO on MgO at low power does not trace the resonance curve since there is a slow time process in IMD generation ($\tau_{IMD} > \tau_{input}$). On the other hand, at high power, this slow time process disappears. In another word, $\tau_{IMD} \leq \tau_{input}$. So, we are able to investigate the time scale in IMD generation involving the substrate. This MgO substrate effect increases as the temperature decreases below 20 K and input power decreases. We already know that MgO is not linear at low power [58]. Our off-the-resonance excitation measurements indicate that generation of nonlinearities in MgO is a slow process.

A.4 Conclusion

Off-the-resonance excitation showed that $\tau_{IMD} \leq \tau_{input}$ as long as the substrate is $LaAlO_3$. Generation of a Lorentzian distribution curve with the same "Q" as resonator by the IMD output power conclusively confirmed that the only source of the IMD is the resonator. When $\tau_{IMD} > \tau_{input}$, the same method showed that IMD output power is lower than that of Lorentzian resonance curve. YBCO on MgO substrate at low temperature ($T < 20K$) and low power ($P^1_{out} < -30dBm$) showed this property. This indicates that generation of nonlinearities in MgO is a slow process.

Appendix B

Tables

Dewar 1 (From 1.7 K to 4.2 K)

T (K)	*1.7	1.8	1.9	2.3	2.5	2.7	3	4.3
P	600	600	600	50	50	50	50	50
I (sec)	4	4	4	4	4	4	4	4
D (sec)	1	1	1	1	1	1	1	1
Heater usage (%)	4	4	9	2	5	7	11	2
Heater capacity (W)	0.05	0.05	0.05	0.5	0.5	0.5	0.5	0.5

Dewar 2 (From 4.2 K to T_c)

T	4.3	5	7	8	10	15	20	30	40	50	55	60	65	70	80	85
P	50	50	50	50	50	100	150	300	400	400	600	600	900	900	900	900
I	4	4	4	4	4	4	4	4	10	12	12	12	12	12	12	12
D	1	1	1	1	1	1	1	1	3	3	3	3	3	3	3	3
%	2	2	11	13	27	68	16	21	35	44	33	43	12	34	40	45
W	0.5	0.5	0.5	0.5	0.5	0.5	5	5	5	5	5	5	5	5	5	5

Table B.1: Typical values of P, I, and D coefficients.

Single sided excitation

f_1	f_1	$2f_1 - f_2$	$2f_2 - f_1$
$f_o - \frac{1}{64}\Delta f_{3dB}$	$f_o + \frac{1}{64}\Delta f_{3dB}$	$f_o - \frac{3}{64}\Delta f_{3dB}$	$f_o + \frac{3}{64}\Delta f_{3dB}$
$f_o + \Delta f_{3dB} - \frac{1}{64}\Delta f_{3dB}$	$f_o + \Delta f_{3dB} + \frac{1}{64}\Delta f_{3dB}$	$f_o + \Delta f_{3dB} - \frac{3}{64}\Delta f_{3dB}$	$f_o + \Delta f_{3dB} + \frac{3}{64}\Delta f_{3dB}$
$f_o + 2\Delta f_{3dB} - \frac{1}{64}\Delta f_{3dB}$	$f_o + 2\Delta f_{3dB} + \frac{1}{64}\Delta f_{3dB}$	$f_o + 2\Delta f_{3dB} - \frac{3}{64}\Delta f_{3dB}$	$f_o + 2\Delta f_{3dB} + \frac{3}{64}\Delta f_{3dB}$
$f_o + 3\Delta f_{3dB} - \frac{1}{64}\Delta f_{3dB}$	$f_o + 3\Delta f_{3dB} + \frac{1}{64}\Delta f_{3dB}$	$f_o + 3\Delta f_{3dB} - \frac{3}{64}\Delta f_{3dB}$	$f_o + 3\Delta f_{3dB} + \frac{3}{64}\Delta f_{3dB}$
$f_o + 4\Delta f_{3dB} - \frac{1}{64}\Delta f_{3dB}$	$f_o + 4\Delta f_{3dB} + \frac{1}{64}\Delta f_{3dB}$	$f_o + 4\Delta f_{3dB} - \frac{3}{64}\Delta f_{3dB}$	$f_o + 4\Delta f_{3dB} + \frac{3}{64}\Delta f_{3dB}$
$f_o + 5\Delta f_{3dB} - \frac{1}{64}\Delta f_{3dB}$	$f_o + 5\Delta f_{3dB} + \frac{1}{64}\Delta f_{3dB}$	$f_o + 5\Delta f_{3dB} - \frac{3}{64}\Delta f_{3dB}$	$f_o + 5\Delta f_{3dB} + \frac{3}{64}\Delta f_{3dB}$

Double sided excitation

f_1	f_2	$2f_1 - f_2$	$2f_2 - f_1$
$f_o - \frac{1}{64}\Delta f_{3dB}$	$f_o + \frac{1}{64}\Delta f_{3dB}$	$f_o - \frac{3}{64}\Delta f_{3dB}$	$f_o + \frac{3}{64}\Delta f_{3dB}$
$f_o - \Delta f_{3dB}$	$f_o + \Delta f_{3dB}$	$f_o - 3\Delta f_{3dB}$	$f_o + 3\Delta f_{3dB}$
$f_o - 1.5\Delta f_{3dB}$	$f_o + 1.5\Delta f_{3dB}$	$f_o - 4.5\Delta f_{3dB}$	$f_o + 4.5\Delta f_{3dB}$
$f_o - 2\Delta f_{3dB}$	$f_o + 2\Delta f_{3dB}$	$f_o - 6\Delta f_{3dB}$	$f_o + 6\Delta f_{3dB}$
$f_o - 2.5\Delta f_{3dB}$	$f_o + 2.5\Delta f_{3dB}$	$f_o - 7.5\Delta f_{3dB}$	$f_o + 7.5\Delta f_{3dB}$
$f_o - 3\Delta f_{3dB}$	$f_o + 3\Delta f_{3dB}$	$f_o - 9\Delta f_{3dB}$	$f_o + 9\Delta f_{3dB}$

Table B.2: Off-the-excitation frequency values for input and IMD.

Appendix C

Figures

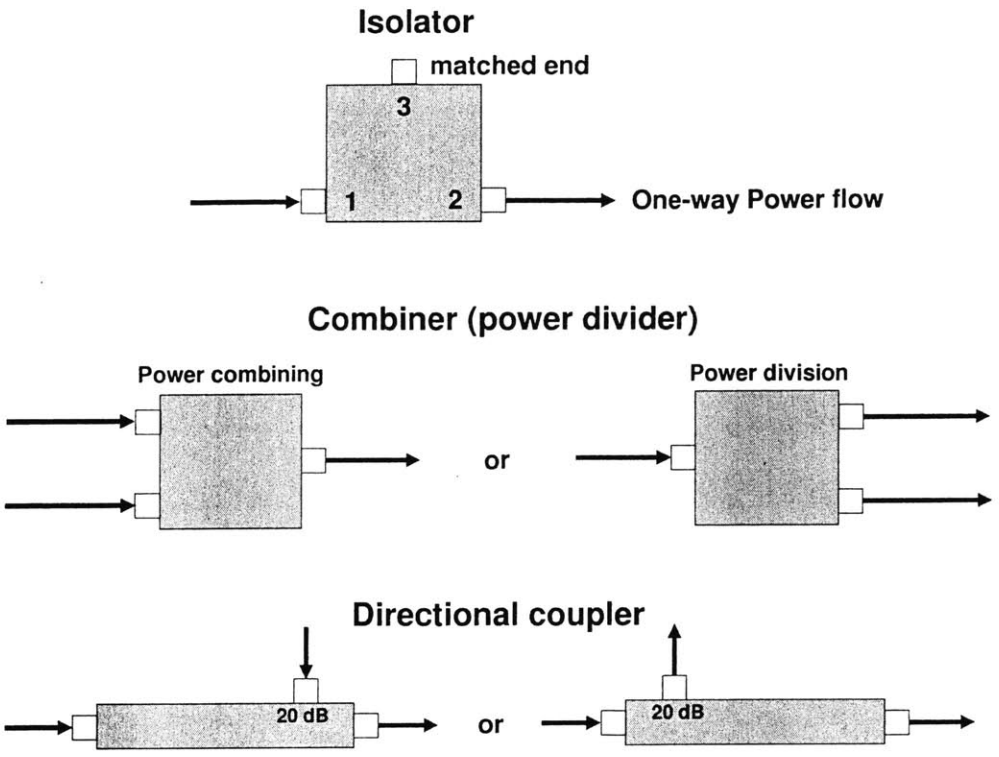

Figure C-1: Passive microwave devices

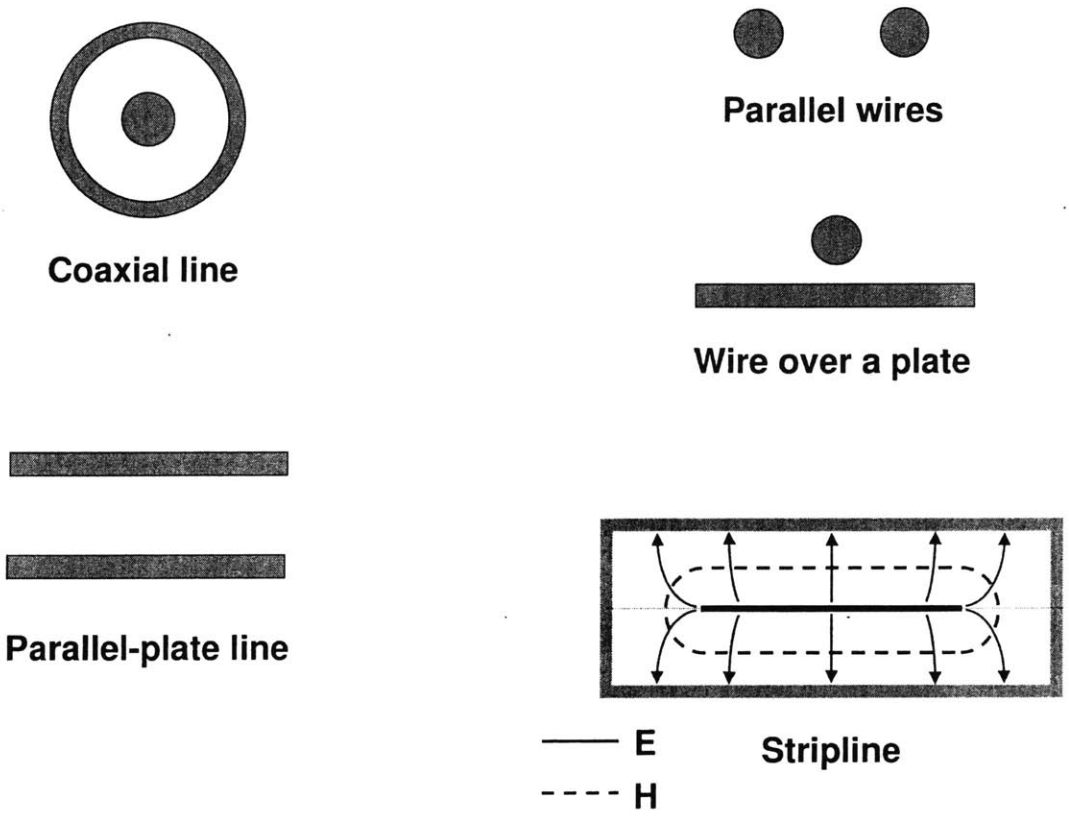

Figure C-2: General TEM transmission lines: cross-section does not vary along the direction of wave propagation

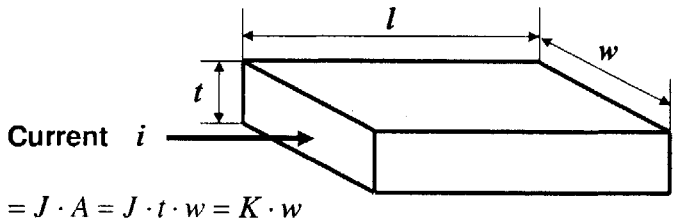

$$i = J \cdot A = J \cdot t \cdot w = K \cdot w$$

where J **(A/m²) : volume current**
K **(A/m) : surface current**
A **(m²) : crosssectional area**

Resistance $R(\Omega) \equiv \dfrac{\rho \cdot l}{A} = \dfrac{l}{\sigma \cdot A} = \dfrac{l}{\sigma \cdot t \cdot w}$

where $\rho(\Omega \cdot m)$ **resistivity**
$\sigma(\Omega^{-1} m^{-1})$ **conductivity**

Power dissipation per unit area

$$P_{dis} = \frac{\frac{1}{2} i^2 R}{l \cdot w} = \frac{\frac{1}{2}(K \cdot w)^2}{l \cdot w} \cdot \frac{l}{\sigma \cdot t \cdot w} = \frac{1}{2} K^2 \frac{1}{\sigma \cdot t} = \frac{1}{2} K^2 R_S$$

Therefore, surface resistance $R_S(\Omega/\square) = R\dfrac{w}{l}$

Figure C-3: Comparison between the resistance and the surface resistance

2-port microwave network

Scattering Matrix

$$\begin{bmatrix} V_1^- \\ V_2^- \end{bmatrix} = \begin{bmatrix} S_{11} & S_{12} \\ S_{21} & S_{22} \end{bmatrix} \begin{bmatrix} V_1^+ \\ V_2^+ \end{bmatrix} \quad \begin{aligned} V_1^- &= S_{11}V_1^+ + S_{12}V_2^+ \\ V_2^- &= S_{21}V_1^+ + S_{22}V_2^+ \end{aligned}$$

Transmission coefficient $T = S_{21} = \left.\frac{V_2^-}{V_1^+}\right|_{V_2^+ = 0}$ *means matched load*

Insertion loss $IL = -20\log(T)\,dB = -20\log(S_{21})dB = 10\log\left(\frac{P_{inc}}{P_{load}}\right)dB$

Figure C-4: Definition of S-parameters

$$Q_L = \frac{f_o}{\Delta f} \qquad \frac{1}{Q_L} = \frac{1}{Q_o} + \frac{1}{Q_{ext\,1}} + \frac{1}{Q_{ext\,2}}$$

$$\therefore \frac{1}{Q_L} = \frac{1}{Q_o} + \frac{\beta_1}{Q_o} + \frac{\beta_2}{Q_o} \longrightarrow Q_o = Q_L(1+\beta_1+\beta_2)$$

Prove $Q_o = Q_L(1+\beta_1+\beta_2) = Q_L \dfrac{1}{1-S_{21}}$

Define $\beta = \dfrac{\text{externally dissipated power}}{\text{internally dissipated power}}$

$\beta_1 = \dfrac{Q_o}{Q_{ext\,1}} \qquad \beta_2 = \dfrac{Q_o}{Q_{ext\,2}}$

$\beta < 1$ **undercoupled**
$\beta = 1$ **critically coupled**
$\beta > 1$ **overcoupled**

Definition: Insertion loss (in dB) at resonance = 10 $\log_{10}(P_o/P_L)$

where, power transmission = $\dfrac{\text{power delevered to load}}{\text{availabe power from source}} = \dfrac{P_L}{P_o} = \dfrac{4\beta_1\beta_2}{(1+\beta_1+\beta_2)}$

$$\therefore S_{21} = \mathrm{T} = \sqrt{\frac{P_L}{P_o}} = \frac{2\sqrt{\beta_1\beta_2}}{(1+\beta_1+\beta_2)} \quad \text{--- (A)}$$

Therefore, Insertion loss, IL = -20 log |T| dB

Substitute (A) into $\dfrac{1}{1-S_{21}}$

Then, $$\frac{1}{1-S_{21}} = \frac{1}{1-\dfrac{2\sqrt{\beta_1\beta_2}}{(1+\beta_1+\beta_2)}} = \frac{1}{\dfrac{1+\beta_1+\beta_2-2\sqrt{\beta_1\beta_2}}{(1+\beta_1+\beta_2)}} = \frac{1+\beta_1+\beta_2}{1+(\sqrt{\beta_1}-\sqrt{\beta_2})^2} = 1+\beta_1+\beta_2$$

if $\beta_1 = \beta_2$

Figure C-5: Derivation of the unloaded quality factor Q_o from the loaded quality factor Q_L

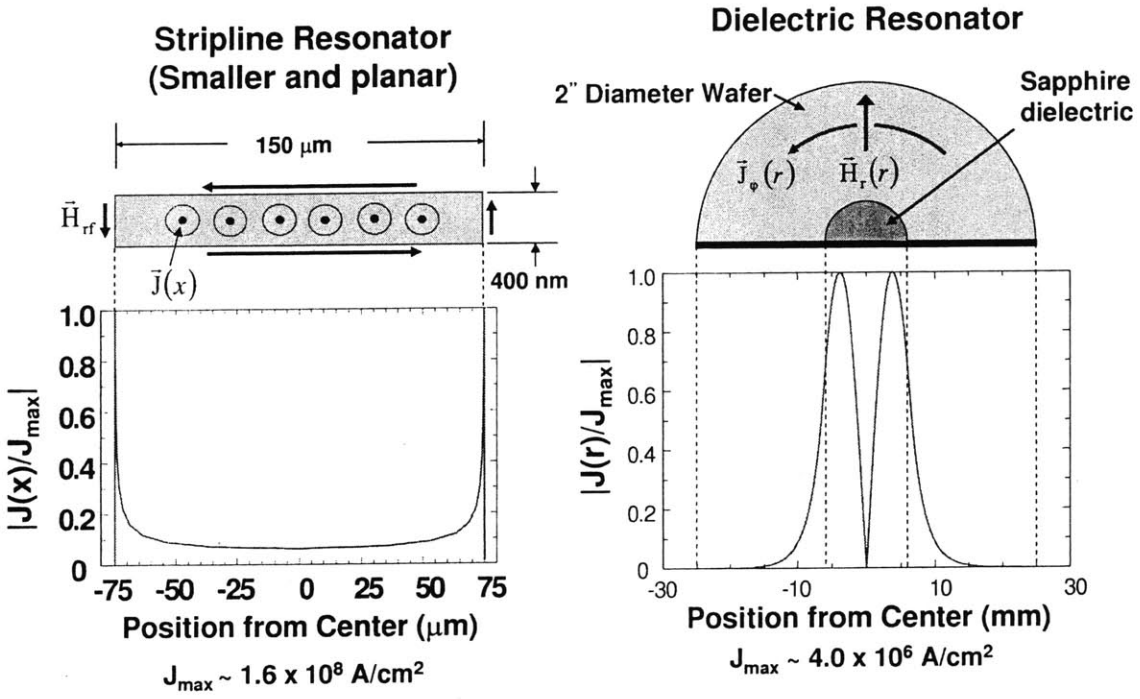

Figure C-6: Comparison of the current density distribution between stripline resonator and dielectric resonator

Using $IL = \frac{P_{out}}{P_{in}} = r_v^2$ eq (1)

$IL = \frac{4Q_L^2}{Q_{coupl}^2}$ eq (2)

by equating eq (1) and eq (2)

We have $r_v^2 = \frac{4Q_L^2}{Q_{coupl}^2}$.

Rearranging gives $\frac{Q_L}{r_v} = \frac{Q_{coupl}}{2} \cong \text{constant}$

Figure C-7: Derivation of $Q/r_v \simeq 10^6$ nearly constant in our resonator regardless of input power and temperature. Eq (2) was obained from combining eq (2.17b) and eq (2.24) in p.151, Matthias Hein, High-Temperature-Superconductor Thin Films at Microwave Frequencies, Springer-Verlag, Berlin, Germany, 1999.

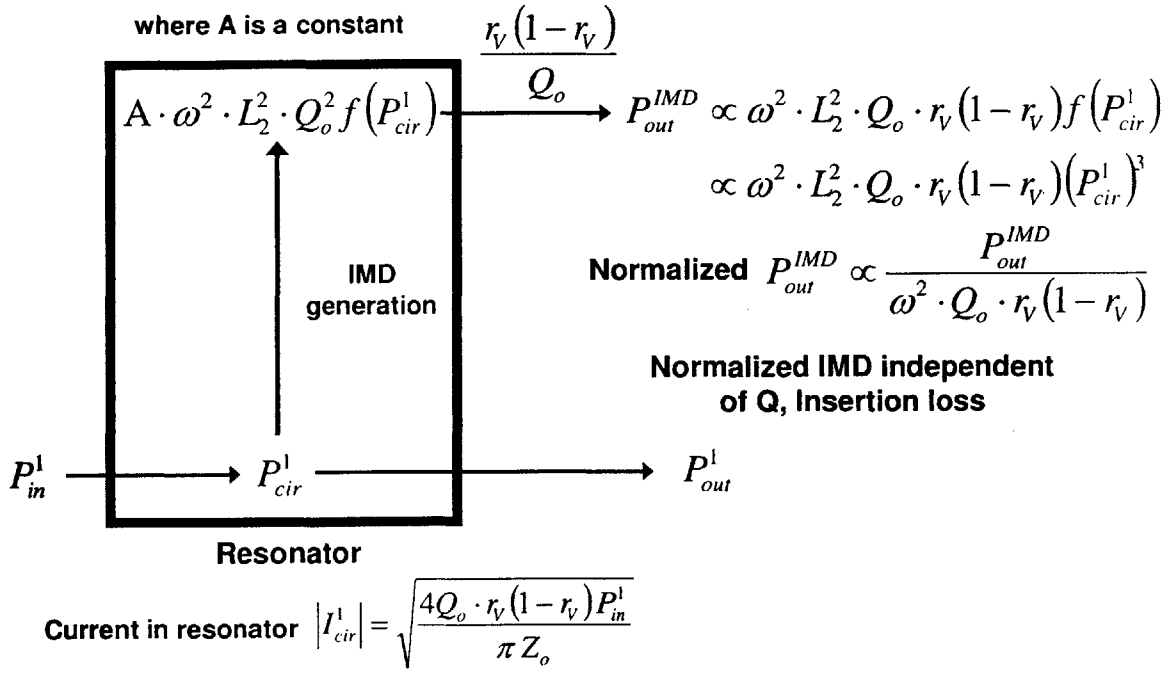

Figure C-8: IMD generation diagram.

In combiner $I(t) = I_1(t) + I_2(t) = A\cos\omega_1 t + B\cos\omega_2 t$

$$\therefore I^2(t) = (A\cos\omega_1 t + B\cos\omega_2 t)(A\cos\omega_1 t + B\cos\omega_2 t)$$

$$= A^2\cos^2\omega_1 t + B^2\cos^2\omega_2 t + 2AB\cos\omega_1 t\cos\omega_2 t = A^2\cos^2\omega_1 t + B^2\cos^2\omega_2 t + AB\{\cos(\omega_1+\omega_2)t + \cos(\omega_1-\omega_2)t\}$$

$$\therefore I^3(t) = (A\cos\omega_1 t + B\cos\omega_2 t)\cdot[A^2\cos^2\omega_1 t + B^2\cos^2\omega_2 t + AB\{\cos(\omega_1+\omega_2)t + \cos(\omega_1-\omega_2)t\}]$$

$$= \underbrace{A^3\cos^3\omega_1 t}_{\mathbf{1}} + \underbrace{AB^2\cos\omega_1 t\cos^2\omega_2 t}_{\mathbf{2}} + \underbrace{A^2B\{\cos\omega_1 t\cos(\omega_1+\omega_2)t}_{\mathbf{3}} + \underbrace{\cos\omega_1 t\cos(\omega_1-\omega_2)t\}}_{\mathbf{4}}$$

$$+ \underbrace{B^3\cos^3\omega_2 t}_{\mathbf{5}} + \underbrace{A^2B\cos^2\omega_1 t\cos\omega_2 t}_{\mathbf{6}} + \underbrace{AB^2\{\cos\omega_2 t\cos(\omega_1+\omega_2)t}_{\mathbf{7}} + \underbrace{\cos\omega_2 t\cos(\omega_1-\omega_2)t\}}_{\mathbf{8}}$$

1 $A^3\cos^3\omega_1 t = \frac{A^3}{4}(\cos 3\omega_1 t + 3\cos\omega_1 t)$

2 $AB^2\cos\omega_1 t\cos^2\omega_2 t = AB^2\cos\omega_1 t\frac{1+\cos 2\omega_2 t}{2} = \frac{AB^2}{2}\{\cos\omega_1 t + \cos\omega_1 t\cos 2\omega_2 t\} = \frac{AB^2}{2}\left\{\cos\omega_1 t + \frac{\cos(\omega_1+2\omega_2)t + \cos(2\omega_2-\omega_1)t}{2}\right\}$

3 $A^2B\{\cos\omega_1 t\cos(\omega_1+\omega_2)t = A^2B\frac{\cos(2\omega_1+\omega_2)t + \cos\omega_2 t}{2}$

4 $A^2B\cos\omega_1 t\cos(\omega_1-\omega_2)t = A^2B\frac{\cos(2\omega_1-\omega_2)t + \cos\omega_2 t}{2}$

5 $B^3\cos^3\omega_2 t = \frac{B^3}{4}(\cos 3\omega_2 t + 3\cos\omega_2 t)$

6 $A^2B\cos\omega_2 t\cos^2\omega_1 t = A^2B\cos\omega_2 t\frac{1+\cos 2\omega_1 t}{2} = \frac{A^2B}{2}\{\cos\omega_2 t + \cos\omega_2 t\cos 2\omega_1 t\} = \frac{A^2B}{2}\left\{\cos\omega_2 t + \frac{\cos(\omega_2+2\omega_1)t + \cos(2\omega_1-\omega_2)t}{2}\right\}$

7 $AB^2\{\cos\omega_2 t\cos(\omega_1+\omega_2)t = AB^2\frac{\cos(2\omega_2+\omega_1)t + \cos\omega_1 t}{2}$

8 $AB^2\cos\omega_2 t\cos(\omega_1-\omega_2)t = AB^2\frac{\cos\omega_1 t + \cos(2\omega_2-\omega_1)t}{2}$

Therefeore $I^3(t) = \underbrace{\frac{3}{4}A^2B\cos(2\omega_1-\omega_2)t}_{\text{from 4 and 6}} + \underbrace{\frac{3}{4}AB^2\cos(2\omega_2-\omega_1)}_{\text{from 2 and 8}} + \cdots$

Figure C-9: The derivation of IMD frequencies.

1. Measure f_o, Q_L as a function of input power and T.

$$f_o(T) = f_o(T_o)\sqrt{\frac{L[\lambda(T_o)]}{L[\lambda(T)]}} \qquad \because f_o = \frac{1}{2\pi\sqrt{LC}}$$

$$L(\lambda) = \frac{\mu_o \int_S \left(H^2 + \lambda^2 j^2(x)\right) dS}{\left(\int_S j dS\right)^2} = \frac{\mu_o \int_S \left(H^2 + \lambda^2 j^2(x)\right) dS}{I^2}$$

$$\lambda(T) = \frac{\lambda_o(T_o)}{\sqrt{1 - \left(\frac{T}{T_C}\right)^4}}$$

Get $\lambda_o(T_o)$ and T_C from fitting all three equations with f_o vs T data.

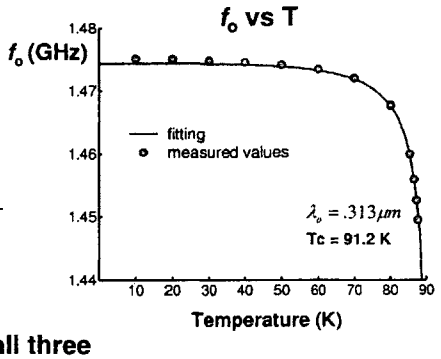

2. Get R from $Q_o = \omega_o L / R$ where $Q_o = Q_L \frac{1}{1 - |S_{21}|}$ and $|S_{21}| = \sqrt{\frac{P_{out}^1}{P_{in}^1}}$

Get $\sigma_2 = \frac{1}{\omega\mu_o\lambda^2}$

Get σ_1 from $\frac{1}{2}R\left|\int_S j dS\right|^2 = \frac{1}{2}R|I|^2 = \frac{1}{2}\int_S \left(\frac{\sigma_1}{\sigma_2^2}\right)|j|^2 dS$

3. Using σ_1, λ, get $R_S = \frac{\omega^2\mu_o^2\sigma_1\lambda^3}{2}$ and $X_S(T) = \omega\mu_o\lambda(T)$ from Two Fluid Model

Figure C-10: Summary of the extraction of R_s and X_s from Q and f_o vs Power and T.

Appendix D

Selected Reprints

Intermodulation Distortion and Third-Harmonic Generation in YBCO Films of Varying Oxygen Content

D. E. Oates, S.-H. Park, M. A. Hein, P. J. Hirst, and R. G. Humphreys

Abstract—**We have measured the nonlinear surface impedance, intermodulation distortion (IMD), and third-harmonic generation (THG) in a series of identically prepared YBaCuO films that have been carefully annealed to produce a controlled oxygen stoichiometry. These are also compared with an unannealed film. The measurements were performed using a stripline-resonator technique as a function of temperature at a fundamental frequency of 2.3 GHz; the IMD tone separation was 10 kHz. We have found that overdoping films with oxygen substantially lowers the IMD relative to optimally and underdoped films. We have also observed differences in the slopes of the THG and IMD, with IMD slope of close to 2:1 while the same film shows THG slope of 3:1. A possible explanation of the differences lies in the different time scales to which IMD and THG are sensitive.**

Index Terms—**Intermodulation distortion, microwave surface impedance, nonlinear surface impedance, YBCO films.**

I. Introduction

NONLINEAR effects are still one of the limits to more widespread application of high-T_c materials in microwave frequency devices. Two-tone intermodulation distortion (IMD) and third-harmonic generation (THG) are deleterious effects observed in all superconducting materials, especially high-T_c superconductors. In practical devices such as filters, these effects can degrade performance, even at relatively low power for filters with narrow bandwidth or very sharp skirts. The IMD and THG are believed to arise from the same nonlinear current–voltage characteristic that also leads to the nonlinear surface impedance. Understanding of their origins, however, is lacking. It has been generally accepted that measured IMD is larger than intrinsic values inferred from theoretical considerations. We present measurements of IMD and THG for some representative films from the series of films of varying oxygen content that we have been characterizing [1], [2]. We find that oxygen content strongly influences the nonlinear effects, and overdoped films perform substantially better than optimally or underdoped material.

Manuscript received August 6, 2002. This work was supported in part by AFOSR, USA, EOARD, U.K., Contract F61775-01-WE033, and MOD, U.K.

D. E. Oates and S.-H. Park are with the MIT Lincoln Laboratory, Lexington, MA 02420 USA (e-mail: oates@ll.mit.edu).

M. A. Hein was with the Department of Physics, University of Wuppertal, Germany. He is now with the Faculty of Electrical Engineering and Information Technology, Technical University of Ilmenau, Germany.

P. J. Hirst and R. G. Humphreys are with QinetiQ, Malvern, U.K.

Digital Object Identifier 10.1109/TASC.2003.813717

II. Film Deposition and Annealing

The 350-nm-thick single-sided epitaxial YBCO films used in this study were electron-beam coevaporated at 700 °C, close to the 1:2:3 cation stoichiometry, onto commercially available 1 cm × 1 cm × 0.5 mm MgO substrates [3], [4]. The oxygenation level of the as-grown films was adjusted by sequential annealing in argon or plasma-activated oxygen, and characterized by DC magnetization measurements of the critical temperature T_c and current density J_c. The doping level could be inferred from the qualitatively different dependences of T_c and J_c on the oxygen deficiency. In addition, the c-axis lattice parameter was determined by the usual θ–2θ X-ray scans. While the absolute value of the c-axis parameter depends on the film deposition technique, it has been found to be a reliable indicator of relative changes of the oxygenation level [5]. The films of each of three batches were deposited simultaneously in the same run, ensuring equivalent deposition and growth conditions. The final oxygenation level of the films ranged from strongly underdoped (strongly reduced T_c, low J_c) to overdoped (moderately reduced T_c, high J_c). Nine samples from 3 different batches have been characterized, ranging from strongly underdoped (69 K) to strongly overdoped (85 K) including as-grown and annealed samples. The different batches have slightly different stoichiometry, and we see small differences in microwave properties from batch to batch, but the behavior is quite similar, especially the differences due to varying oxygen content. Space does not permit a full report of the findings on all films. Here we summarize the most important results on representative films.

III. Measurement Techniques

The films were patterned using standard photolithography and wet etching in dilute phosphoric acid. After patterning, they were assembled as stripline resonators with two YBCO ground planes on MgO substrates, mounted in a connectorized copper package, and characterized at microwave frequencies. Detailed resonator description can be found in [6]. For MgO substrates, the fundamental frequency of the stripline resonator is 2.3 GHz. The characterization comprises measurement of the nonlinear surface impedance $Z_S(T, f, I_{rf})$ as a function of temperature, frequency, and rf current. The resonator is weakly-coupled so that the unloaded Q is measured directly. The same resonator is also used for the IMD and THG measurements. In the following, it will be important to note that the THG measurements, in contrast to the IMD measurements, are nonresonant. While the stripline geometry is a TEM structure, and the third-over-

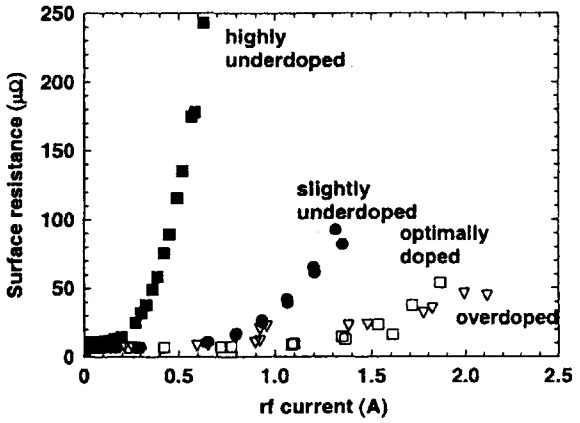

Fig. 1. Plot of R_S versus I_{rf} for films with various oxygen-doping levels at comparable reduced temperatures. $f = 2.2$ GHz. Legend: ■ highly underdoped film $T_c = 69.3$; • slightly underdoped $T_c = 90.7$; □ optimally doped $T_c = 91.7$; ▽ overdoped $T_c = 84.2$. $T = 50$ K except for the highly underdoped film for which $T = 40$ K, $t = 0.57$ to agree with the others.

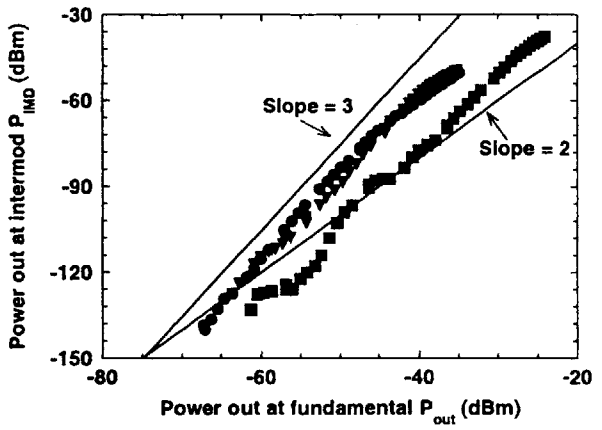

Fig. 2. IMD of three films. ▼ underdoped • as grown ■ overdoped frequency 2.3 GHz $T = 60$ K. Lines of slope = 2 and 3 have been added to the plot for reference.

tone resonance is expected at $3f_0$, three times the fundamental resonance, in practice, enough dispersion is present due to fabrication imperfections that the third overtone does not correspond to $3f_0$. The difference is large enough that the third harmonic can be considered completely nonresonant. This limits the sensitivity of the THG measurements as compared with IMD.

IV. Experimental Results

A. Nonlinear Surface Impedance

Fig. 1 shows typical results of R_S vs I_{rf} for four films: overdoped, $T_c = 90.7$ K, optimally doped $T_c = 91.7$ K, slightly underdoped $T_c = 89$ K, and highly underdoped $T_c = 69$ K. The temperature of the measurements was 50 K except for the film with T_c of 69 K, which was measured at 40 K giving a reduced temperature $t \approx 0.57$ for all films. Clearly, underdoping increases the nonlinear R_S but affects the low power linear surface impedance very little if at all. The optimally doped film and the overdoped film exhibit nearly the same nonlinearity, but the overdoped film shows a slight indication of better performance at high power. Similar results were obtained for other temperatures [1].

B. Intermodulation Distortion

The third-order intermodulation distortion was measured in the usual way, in which two closely spaced tones of equal power at frequencies f_1 and f_2 are combined and applied to the resonator. The frequencies are centered about the resonant frequency and within the 3-dB bandwidth of the resonator. In our case, the tone separation Δf of approximately 10 kHz was used. The third-order mixing products at frequencies $2f_1 - f_2$ and $2f_2 - f_1$ are then measured in a spectrum analyzer as a function of the input power to the resonator.

Fig. 2 shows the results of the measurements for three films from a batch for which IMD measurements are available. These are from a different batch than those shown in Fig. 1, whose IMD measurements have not been analyzed as completely yet. These films include a slightly overdoped film with $T_c = 91.8$ K, an as-grown film with near optimal doping with $T_c = 90.5$ K, and an underdoped film with $T_c = 69$ K. In this case, we have used the c-axis lattice parameter rather than T_c as the measure of overdoping. Those values are 1.1702, 1.1734, and 1.1752 nm, respectively.

To present the data, we plot P_{IMD}, the measured output power at the third-order IMD, as a function of P_{out}, the output power at the fundamental frequencies f_1 and f_2. The P_{out} is proportional to the circulating power at the fundamental P_{circ}. The usual assumption is that the IMD is proportional to the third power of P_{circ}. Therefore, plotting P_{IMD} vs P_{out} is a more meaningful way to compare different films, which might be studied using resonators with different Q and different coupling.

As can be seen in Fig. 2, the IMD of the overdoped film is substantially lower than the IMD of the underdoped and as-grown film. The difference is greater than 10 dB over most of the range, and approaches 20 dB in many places. This improvement by overdoping is the first observation of a method to lower IMD by means of steps in the film fabrication process. In addition, none of the data sets show the 3:1 slope expected from simple arguments for the third order IMD. The slope lines shown on the plot are only for reference. In particular, the overdoped film does not show a well-defined slope.

To further understand the differences in IMD among these films, we have also measured the nonlinear surface impedance of the films. Fig. 3 shows the results of those measurements. These results are similar to those in Fig. 1, which came from a different batch. Although the composition of the two batches is slightly different and the films were deposited in different runs, the behavior is quite similar indicating reproducible behavior form batch to batch. Plotted in Fig. 3 on the same vertical scale is the R_S and ΔX_S vs I_{rf} for the films. The the R_S and ΔX_S. values show considerable differences in nonlinearity. There is at this time no accepted detailed theory relating IMD to Z_S. Since presumably the IMD arises from the nonlinear Z_S, however, an estimate of the magnitude of the IMD can be made by comparing the corresponding coefficients of a quadratic fit to the Z_S vs I_{rf} measurements. The fits are shown in Fig. 3(a) and (b)

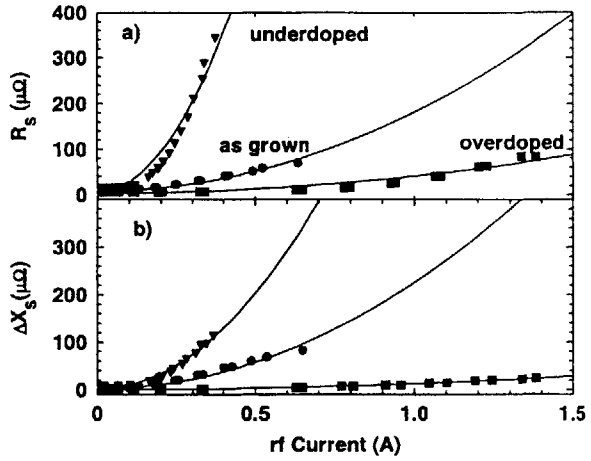

Fig. 3. (a) R_s vs I_{rf} and (b) ΔX_s vs I_{rf} for the films in Fig. 2. The plots use the same vertical scale. The sme symbols are used in both figures. The fits in part a) are $\Delta R_s = \Delta R_{s0} + a_R I_{rf}^2$ with ΔR_{s0} and a_R as free parameters. The values of a_R for the underdoped, as-grown and overdoped are 2002, 172, and 37.6 Ω/A^2, respectively. The fits in part b) are $\Delta X_S = \Delta X_{S0} + a_x I_{rf}^2$ with ΔX_{S0} and a as free parameters. The value of a_X for the underdoped, as-grown and overdoped are 805,223, 12.4 Ω/A^2, respectively.

and the coefficients of the fits for the three films are given in the caption. Since we assume that

$$Z_s = Z_{s0} + aI_{rf}^2 \tag{1}$$

where

$$a = a_R + ja_x \tag{2}$$

and

$$V_{\text{IMD}} = I_{rf}(Z_{s0} + aI_{rf}^2) \tag{3}$$

the third-order IMD power is proportional to a^2. The difference in the quadratic coefficients of the fits to the reactance data in Fig. 3 for the overdoped and as-grown films is approximately the same as the difference in IMD power that is observed experimentally in Fig. 2. The IMD difference is greater than 20 dB. However, more detailed models are required to make a convincing argument and to fully understand the IMD.

C. Third-Harmonic Generation

The third-harmonic generation is measured by applying a CW tone at the center frequency f_0 of the resonator and measuring the power out at both f_0 and $3f_0$. As noted above, the frequency of the third harmonic does not correspond to the frequency of the third overtone resonance of the resonator.

Measurements of THG at a series of temperatures on a representative film are shown in Fig. 4 along with measurements of the IMD for the same film at the same temperatures. This film is an overdoped film with $T_c = 84$ K. As seen, the THG measurements are much less sensitive than the IMD measurements, because as derived by Dahm and Scalapino [7], the IMD measurements are enhanced by the Q of the resonator. Thus, to make a direct comparison between the THG and IMD, it is necessary to first divide the P_{IMD} by the Q of the resonator. In principle, the output coupling of the resonator should also require an adjustment for the different frequencies. This is a small adjustment for the weakly coupled resonator and is neglected here.

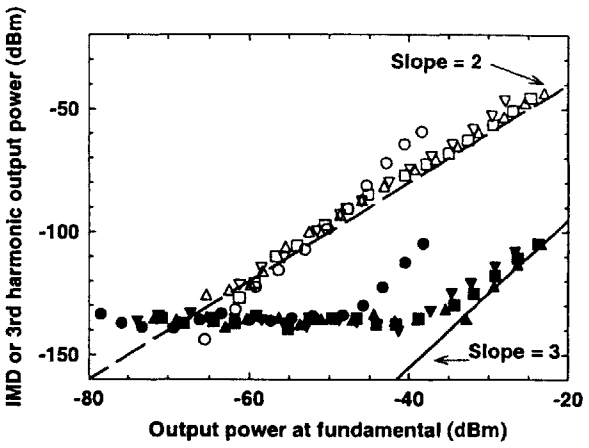

Fig. 4. Measurements of THG and IMD at various temperatures. The open symbol are the IMD and the solid symbols are the THG. Legend: •, ▼, ■, and ▲, T = 80, 60, 40, and 20 K, respectively. The dashed line is slope = 2 and the solid line is slope = 3, both for reference.

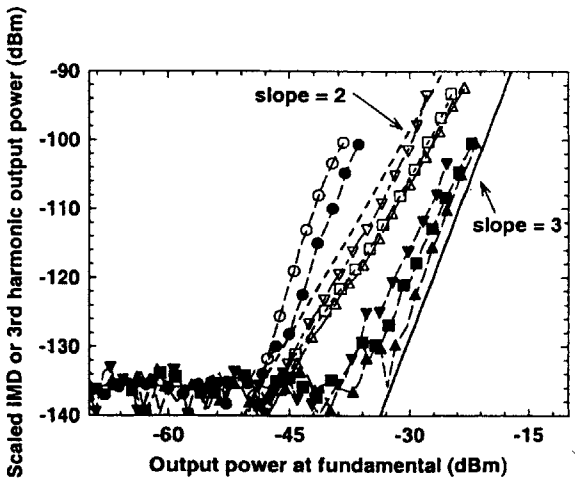

Fig. 5. Comparison of measured THG with the IMD reduced by the resonator Q. Legend is the same as Fig. 4.

The result of dividing the IMD by Q is shown in Fig. 5. While the IMD and THG are now comparable, agreement is nonetheless absent. The reduced IMD does show similar temperature dependence to the THG in that the measurements of IMD at T = 80 K show an increase which is not evident in the raw data of Fig. 4. The IMD seems to be higher than the THG for all temperatures, and more importantly, the IMD at $T \leq 60$ K exhibits a slope of approximately two while the THG for all temperatures shows a slope of approximately three. The dashed line in the figure has a slope of two to indicate the trend of the data. The solid line has a slope of three. While neither IMD nor THG shows exactly slope two or three, respectively, the data do show a disparity in slope. While not a detailed explanation, we suggest that the source of the disparity lies in the different time scales that are relevant to the two signals. The IMD is governed by processes on the time scale of the difference frequency

of the two input tones, in this case approximately 10 kHz. The third-harmonic generation on the other hand requires processes that respond to the frequency of the third harmonic, which is 6.9 GHz in this case.

As has been suggested by Willemsen *et al.* [8], a slope of two for the IMD dependence on power can be explained by a nonlinear impedance of the form

$$Z_s = Z_{s0} + a|J_{rf}| \tag{4}$$

rather than the usual form of

$$Z_s = Z_{s0} + aJ_{rf}^2 \tag{5}$$

which produces the usual slope-three dependence. As we have noted previously [2] the slope of the IMD is correlated to the oxygen content of these films with overdoping tending to produce slope close to two and underdoping and optimum producing slopes close to three. This is an experimental observation without any explanation at this time, suggesting that a simple power law I–V characteristic is not sufficient to describe the IMD in YBaCuO.

V. Conclusion

The most important finding of this investigation so far is that overdoping reduces the nonlinearities when compared to identical films with optimal doping or underdoping. This to our knowledge is the first indication of a controllable parameter that can be used to reduce the nonlinearities. There is as yet no theoretical explanation why overdoping reduces nonlinearities and especially IMD. We have, however, previously shown [1] that impurities strongly enhance nonlinear effects. We suggest that the enhanced nonlinearities from impurities result from crystalline disorder at the atomic scale, and oxygen deficiency plays a similar role to the impurities. Thus, it may be that full oxygen content (overdoping) gives better crystalline order and thus lower nonlinearities. Clearly further study of the effects of overdoping is required.

We have also observed substantial differences between IMD and THG in the same overdoped film. After normalization for the resonator Q the level of the IMD is higher than the THG and the slope of the IMD vs output power is close to 2:1 while the THG slope is close to 3:1. These differences can possibly be attributed to the different time scales that govern the two processes.

Acknowledgment

The authors would like to thank R. Heath and D. Elliner for film growth and annealing, D. Baker for device fabrication, R. P. Konieczka for device assembly, and G. Fitch for programming.

References

[1] D. E. Oates, M. A. Hein, P. J. Hirst, R. G. Humphreys, G. Koren, and E. Polturak, "Nonlinear microwave surface impedance of YBCO films: Latest results and present understanding," *Physica C*, vol. 372–376, no. P1, pp. 462–468, 2002.

[2] M. A. Hein, R. G. Humphreys, P. J. Hirst, S.-H. Park, and D. E. Oates, "Nonlinear microwave response of epitaxial YBaCuO films of varying oxygen content on MgO substrates," *J. Supercond*, submitted for publication.

[3] R. G. Humphreys *et al.*, *Mater. Sci. Eng.*, vol. B10, p. 293, 1991.

[4] N. G. Chew, S. W. Goodyear, J. A. Edwards, J. S. Satchell, S. E. Blenkinsop, and R. G. Humphreys, "Effect of small changes in composition on the electrical and structural properties of $YBa_2Cu_3O_7$ thin films," *Appl. Phys. Lett.*, vol. 57, pp. 2016–2018, 1990.

[5] N. G. Chew *et al.*, "Effect of composition and oxygen content on the microwave properties of evaporated Y–Ba–Cu–O thin films," *IEEE Trans. Appl. Supercond.*, vol. 5, p. 1167, 1995.

[6] D. E. Oates and A. C. Anderson, "Surface impedance measurements of $YBa_2Cu_3O_{7-x}$ thin films in stripline resonators," *IEEE Trans. Magn.*, vol. 27, pp. 1001–1005, 1991.

[7] T. Dahm and D. J. Scalapino, "Theory of intermodulation in a superconducting microstrip resonator," *J. Appl. Phys.*, vol. 81, pp. 2002–2009, 1997.

[8] B. A. Willemsen, B. H. King, T. Dahm, and D. J. Scalapino, "Microwave intermodulation in high-T_c superconducting microstrip resonators," *IEEE Trans. Appl. Supercond.*, vol. 9, pp. 4181–4184, 1999.

Journal of Superconductivity: Incorporating Novel Magnetism, Vol. 16, No. 5, October 2003 (© 2003)

Nonlinear Microwave Response of Epitaxial YBaCuO Films of Varying Oxygen Content on MgO Substrates

M. A. Hein,[1] R. G. Humphreys,[2] P. J. Hirst,[2] S. H. Park,[3] and D. E. Oates[3]

Received September 30, 2002

We have investigated the nonlinear microwave properties of electron-beam coevaporated $YBa_2Cu_3O_{7-x}$ films on MgO, using stripline resonators at 2.3 GHz and temperatures 1.7–80 K. The oxygen content of the films ranged from strongly underdoped to overdoped. Above 20 K, the nonlinear response of the resonators was dominated by the superconductor. We could establish clear correlations between the nonlinear surface resistance, two-tone intermodulation (IMD), and oxygen content of the films, which indicate that the superconducting order parameter is important for the nonlinearities. A power-law representation of the nonlinear current-voltage relation would not be appropriate to explain our results phenomenologically. Below 20 K, the dielectric loss tangent of MgO dominated the nonlinear response of the resonators. With increasing power, the dissipation losses decreased markedly, accompanied by enhanced IMD. The surface reactance passed through a shallow minimum at about 5 K, independent of power. We attribute these effects to resonant absorption by impurity states in MgO.

KEY WORDS: surface impedance; frequency intermodulation; dielectric loss tangent; high-temperature superconductor.

1. INTRODUCTION

While passive high-temperature superconductor (HTS) microwave devices are finding applications in systems for wireless communication, signal recognition, and medical diagnostics [1], the nonlinear surface impedance $Z_s(I_{rf})$ and third-order intermodulation distortion (IMD) limit wider application. This limitation applies especially to resonant devices in which the oscillating power P_{osc} is high, due to, e.g., enhanced group delay, high quality factors, or high operating power [2]. Understanding and controlling the nonlinear microwave response of HTS films is, therefore, important for narrowband, sharp cutoff, receive filters, which are susceptible to intermodulation, and high-power transmit filters, which suffer from power-dependent absorption. The sources of nonlinear Z_s and IMD, while related, are not well understood at present. In addition, the possible contribution of the substrates to the nonlinear response has been widely neglected until recently [3], although the dielectric loss tangent and permittivity are important parameters for the design and operation of compact microwave devices [2,4].

We have investigated the nonlinear surface impedance $Z_s(I_{rf})$ and IMD of epitaxial $YBa_2Cu_3O_{7-x}$ (YBCO) films of different oxygen deficiency x, using stripline resonators at ~2.3 GHz and temperatures 1.7–80 K. We have established clear correlations between the onset of nonlinear R_s, the dependence of the IMD power P_{IMD} on P_{osc}, and the oxygen content of the YBCO films. The results help to understand the nonlinear response theoretically, by pointing to quasiparticle scattering from defects and pair breaking. In addition, we have identified a nonlinear loss mechanism in MgO, which becomes prominent below about 20 K. This result may have important implications for the fabrication and use of MgO, which has become the substrate material of choice for HTS microwave applications.

[1]Department of RFQ Microwave Techniques, Technical University of Ilmenau, Germany.
[2]QinetiQ Malvern, Worcestershire, United Kingdom.
[3]M. I. T. Lincoln Laboratory, Lexington, Massachusetts.

0896-1107/03/1000-0895/0 © 2003 Plenum Publishing Corporation

2. EXPERIMENTAL TECHNIQUE

2.1. Film Preparation

The 350–nm-thick single-sided epitaxial YBCO films were electron-beam coevaporated at 690°C, close to the 1:2:3 cation stoichiometry, onto commercially available 1 cm × 1 cm × 0.5 mm MgO substrates [5,6]. The oxygenation level of the As-grown films was adjusted by sequential annealing in argon or plasma-activated oxygen, and characterized by DC magnetization measurements of the critical temperature T_c and current density J_c. The relative doping level could be inferred from the qualitatively different dependences of T_c and J_c on the oxygen deficiency x. In addition, the c-axis lattice parameter was determined by the usual θ–2θ X-ray scans. While the c-axis parameter depends on the substrate and film deposition technique, it has been found to be a reliable indicator of relative changes of the oxygenation level under otherwise unchanged deposition conditions [7]. The data obtained for nine YBCO films from three batches are summarized in Table I. The films of each batch were deposited simultaneously in the same run, ensuring equivalent deposition and growth conditions. The final oxygenation level of the films, which was found to depend on film morphology and the annealing history, ranged from strongly underdoped (strongly reduced T_c, low J_c) to overdoped (moderately reduced T_c, high J_c).

To separate dissipation losses in the superconductor from losses in the dielectric substrate, 400–nm-thick Nb films were fabricated for reference measurements [3]. These films were magnetron sputtered at ambient temperature onto 2–inch-diameter MgO wafers [8] and subsequently diced into 1 cm × 1 cm pieces.

2.2. Microwave Measurements

After patterning the superconductor films into 150-μm-wide meander lines by wet chemical etching, they were clamped with two equivalent ground planes to form a stripline resonator [9]. The quality factor Q and resonant frequency were measured at the fundamental resonance $f = \omega/2\pi = 2.27$ GHz for input power levels $P_{in} = -85 - +30$ dBm. For the fixed geometry of the input and output coupling capacitors, this power range corresponds to electric fields between the center strip and ground planes of $E_{rf} = 0.5$–5×10^5 V/m, or to total microwave currents flowing along the superconducting strip of $I_{rf} = 3 \times 10^{-6}$–3A.

The effective surface resistance derived from the unloaded quality factor comprises losses in the superconductor and the dielectric and is given by [2]:

$$R_{eff} = R_s + G \times \tan\delta, \tag{1}$$

where R_s is the surface resistance of the superconductor, $\tan\delta$ the loss tangent of the dielectric, and G a geometry factor, which depends on the ratio of penetration depth to film thickness [9,10] and, hence, weakly on temperature ($G \sim 0.8\Omega$ is typical for $T < T_c/2$). Changes of the effective reactance are similarly composed of changes of the penetration depth and dielectric permittivity [2]:

$$\Delta X_{eff} = \Delta X_s + G \times \frac{\Delta\varepsilon}{\varepsilon}, \tag{2}$$

where $\Delta X_s = \mu_0 \omega \Delta\lambda$, λ is the temperature-dependent superconducting penetration depth and ε the dielectric permittivity of the substrate.

IMD measurements with a noise floor of −130 dBm were performed with two tones of equal input power, separated by 10 KHz. This frequency spacing approached the full width at half maximum

Table I. Overview of the YBaCuO Films on MgO

Sample batch/ID	T_c (K)[a]	J_c(60 K) (MA/cm^2)	J_c(50 K) (MA/cm^2)	Δc (pm)	Oxygen doping level
1B	90.45	2.67	4.23	11.5	As-grown
1C	90.20	2.23	3.88	11.6	under
1D	89.00	—	—	10.3	~optimum
2A	91.74	11.40	16.20	10.3	~optimum
2B	90.68	5.82	8.62	12.5	under
2C	84.18	10.40	16.85	8.6	over
3A	90.54	2.40	4.01	13.4	As-grown
3C	69.3	0.18	0.81	15.2	under
3D	91.80	8.10	12.00	10.2	slightly over

[a] T_c = critical temperature, J_c = critical current density at 60 and 50 K, Δc = deviation of the c-axis lattice parameter from the value 1.16 nm. All but the As-grown films were postannealed, in successive steps, in argon or plasma-activated oxygen. The oxygenation level of the As-grown films was near optimum doping.

of the resonance for the highest measured Q-values, but it is considered still narrow enough to provide a reliable qualitative picture of the IMD behavior. More accurate modeling of the nonlinear response including the bandpass characteristic of the resonator is in progress.

3. NONLINEAR MICROWAVE RESPONSE OF YBCO ($T \geq 20$ K)

3.1. Power Handling and Oxygenation Level

Figure 1 compares the dependence of the surface resistance on the total RF current for three YBCO films with different oxygen deficiencies, all from batch #3, at two representative temperatures $T = 20$ K and 50 K. The plots show how the onset for a current-dependent R_s moves to lower currents, and the steepness of $R_s(I_{rf})$ increases, as the films become more oxygen deficient. The steep onset of the nonlinear response is displayed on logarithmic scales in panel b. This plot also illustrates the high quality of the films studied. The surface resistance of, e.g., the overdoped film #3D at 20 K remains constant at $R_s \sim 4\ \mu\Omega$ up to $I_{rf} \sim 1$ A, which corresponds to a magnetic flux density of about 30 mT. This value is only about a factor of 2.5 below the lower critical field expected for bulk YBCO with the RF currents flowing entirely within the Cu—O planes [2].

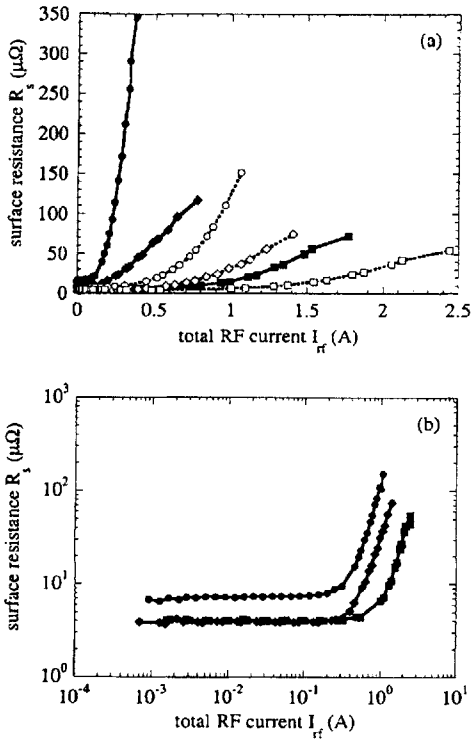

Fig. 1. RF-current dependence of R_s for the samples #3A (near optimum doping, diamonds), #3C (underdoped, circles), and #3D (overdoped, squares) at $f = 2.27$ GHz and $T = 20$ K (open symbols, dotted interpolation curves) and 50 K (full symbols, solid curves), using linear scales (panel (a)) and logarithmic scales (panel (b), $T = 20$ K only).

The RF current dependence of the surface reactance, $\Delta X_s(I_{rf})$, displayed qualitatively the same behaviour as the surface resistance, with the differential loss tangent $r \equiv (\partial R_s/\partial I_{rf})/(\partial X_s/\partial I_{rf})$ approaching at high power constant values between about 1 and 3. The constancy of r indicates that both R_s and X_s follow the same functional dependence on I_{rf} at sufficiently high power.

The observed correlation between oxygen deficiency and nonlinear surface impedance agrees with the common expectation that fully oxygenated films display superior electronic performance, and has accordingly been speculated for some time. However, due to the complicated interdependence of deposition technique, film morphology, and oxygenation level, it has neither been studied systematically nor observed until now.

3.2. Scaling of the Power Handling, Critical RF Current

In order to explore the nature of the nonlinear mechanism in greater detail, it is necessary to distinguish between qualitative changes of the $R_s(I_{rf})$-dependence brought about by different oxygenation levels, and mere changes of the current scales, on which the nonlinearities occur. For this purpose, Fig. 2 (a) shows typical $R_s(I_{rf})$-data for a set of temperatures. Figure 2b shows the same data after rescaling I_{rf} at every temperature such that the scaled $R_s(I_{rf})$-curves merged onto, say, the data for $T = 20$ K. The obvious success of this procedure demonstrates that the temperature dependence of the nonlinear Z_s is caused by that of the scaling current alone. The data in Fig. 2b are consistent with a quadratic current dependence, e.g., in the form of:

$$R_s(I_{rf}, T) = R_{s0}(T) \quad \text{for } I_{rf} < I_0, \text{ and} \tag{3}$$

$$R_s(I_{rf}, T) = R_{s0}(T) + \alpha \times \left[\frac{I_{rf}}{I_0(T)} - 1\right]^2 \quad \text{for } I_{rf} \geq I_0, \tag{4}$$

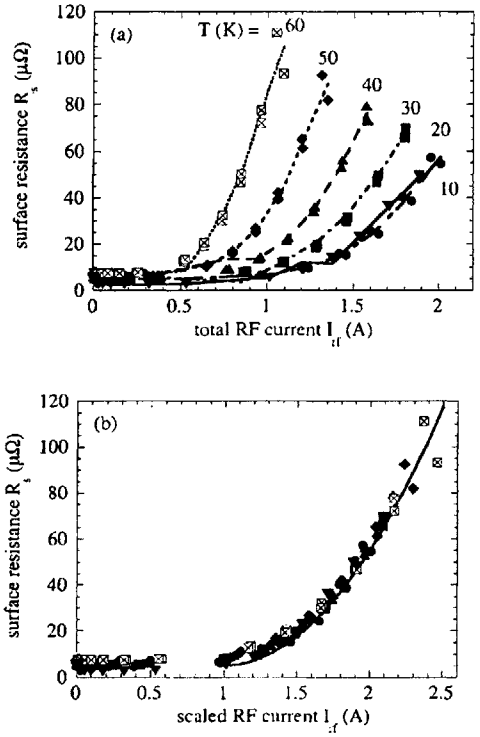

Fig. 2. (a) RF-current dependence of R_s for sample #2B at $f = 2.27$ GHz and various temperatures as indicated (different symbols and interpolation curves). (b) Same data after scaling I_{rf} such that all curves merge with the results for $T = 20$ K. The solid line represents the quadratic fit of Eq. (4).

where α is a constant and I_0 defines the appropriate current scale. The two parts of Eq. (3) emphasize the existence of a threshold current, below which $R_s(I_{rf})$ is constant. We note that at high currents $I_{rf} > I_0$ Eq. (3) is consistent with the simple quadratic approach $R_s = R_0 \times (1 + b_R \times I_{rf}^2)$ used in previous work [11]. The current-scaling of the $R_s(I_{rf})$-dependences of all other samples listed in Table I worked equally well, so that we can exclude functional changes of the $Z_s(I_{rf})$-dependence for varying oxygen deficiency x.

So far, the discussion has focused on changes of the current scale relative to that at 20 K. To derive absolute values for the scaling current, one has to define an appropriate criterion. We have found the following, implicit, definition useful for both low and high-T_c superconductors [12]:

$$R_s(I_{crit}) \equiv 2.5 \times R_{s0}(I_{rf} \to 0). \qquad (5)$$

Using I_{crit} as a criterion for a critical RF current is more versatile than using I_0 in Eq. (4). Equation (5) includes a possible variation of the surface resistance

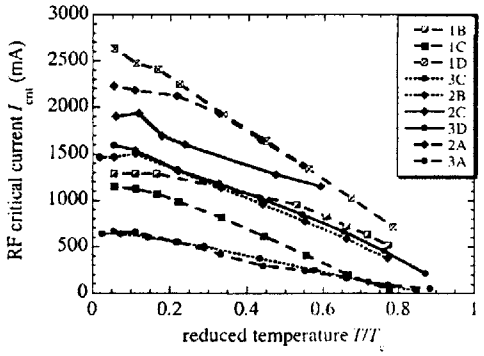

Fig. 3. Critical RF-current versus reduced temperature at $f = 2.3$ GHz for all investigated YBCO films (for details see legend): batch #1 (squares), #2 (diamonds), #3 (circles); underdoped (dotted interpolation curves), near optimum doping (dashed), overdoped (solid).

at low currents, $I_{rf} < I_0$, and combines the two parameters α and I_0 into the single parameter I_{crit}. There are obviously more possibilities to define a characteristic current scale, which, however, will not alter the conclusions to be drawn.

Figure 3 displays the results for I_{crit} versus reduced temperature $t \equiv T/T_c$, for all films studied. The properties of the samples discussed so far provide insufficient information to relate the absolute $I_{crit}(0)$-values to the film preparation. However, almost all curves have in common a nearly linear temperature dependence of I_{crit} for $T/T_c > 0.5$. Such a behaviour is expected and was observed for various types of grain-boundary Josephson junctions, where the coupling between the superconducting electrodes is believed to occur via localized states [13,14]. However, in view of the high quality of the films (high J_c-values and good power handling), we don't expect granular effects to be relevant in our samples. Another, more likely, explanation is based on the observation of a linear temperature dependence of the magnetic field at which flux penetrated a superconducting stripline [15]. We are thus led to speculate that the RF critical current I_{crit} could be related to the DC critical current density J_c. This is indeed the case, as illustrated in more detail in the following section.

3.3. Correlations Between DC and RF Nonlinearities

The critical current density J_c is a key parameter to describe the nonlinear current-voltage characteristics (IVC) of superconductors at DC or low

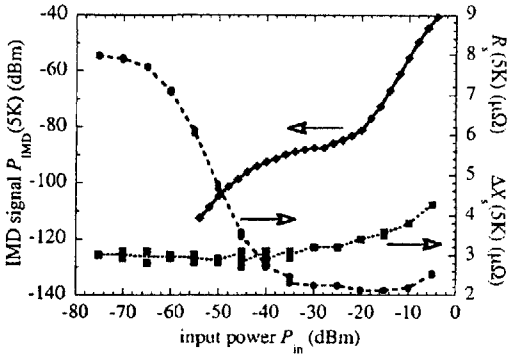

Fig. 4. Typical power dependence of the effective surface resistance (circles, dashed interpolation), change of surface reactance (squares, dotted), and IMD signal (diamonds, solid) for YBCO on MgO (sample #2B) at $f = 2.3$ GHz and $T = 5$ K.

frequencies. We have therefore examined our microwave data for correlations between characteristic RF parameters and J_c. The first parameter considered is the critical RF current introduced by Eq. (5). The other two parameters are derived from our results for IMD as follows:

1. The third-order intercept (TOI) quantifies the power level at which the extrapolated IMD signal equals the input power. To avoid complications related to the geometry of our resonators and the nonlinear compression of $P_{out}(P_{in})$, we have derived TOI-data from plotting the power measured at the two symmetric third-order IMD-sidebands, P_{IMD}, versus output power at the fundamental tone, P_{out}. We note that P_{out} is proportional to the oscillating power. Under certain experimental conditions, the measured $P_{IMD}(P_{out})$-curves were not simple straight lines but displayed curvature (for an example, see Fig. 4 and related discussion in Sec. 4). The TOI was determined in such cases from the asymptotic behavior of P_{IMD} at high power levels (e.g., above −20 dB m in Fig. 4). TOI values could be derived graphically or numerically, according to the condition $P_{IMD} = P_{out}$, using the entire set of IMD data, or just one point on the $P_{IMD}(P_{out})$-curve and the slope at that point. Both techniques yielded almost identical results (filled and open symbols in Fig. 5b), confirming the consistency of our analysis. If the IV-relation effective at microwave frequencies were described by a power series expansion, the TOI (in dB m) should scale logarithmically with the square of the characteristic current [2,16].
2. The slope m of the $P_{IMD}(P_{out})$-curves, plotted on logarithmic scales, measures the exponent of the functional dependence of P_{IMD} on P_{out}, $m = \partial \log P_{IND}/\partial \log P_{out}$. In case of a power-series representation of the IVC, third-order effects like frequency intermodulation or harmonic generation lead to a constant slope, $m = 3$.

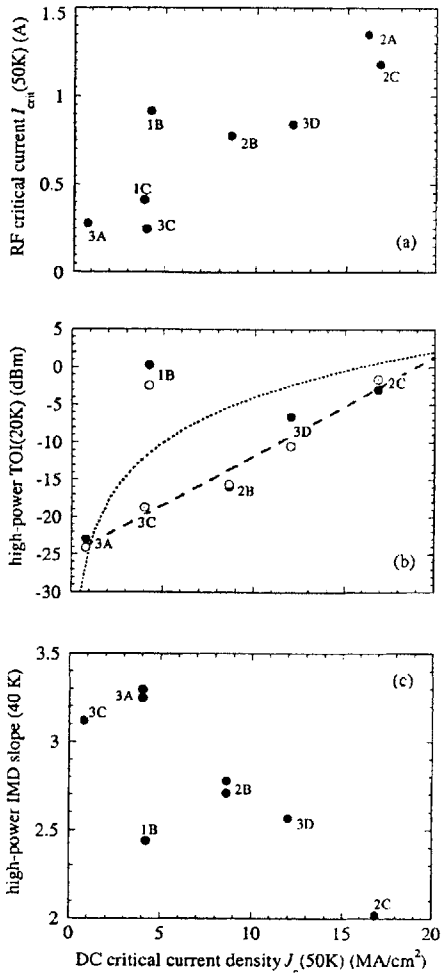

Fig. 5. Correlation between the DC critical current density J_c(50 K) and the RF critical current I_{crit}(50 K) (panel (a)), high-power third-order intercept TOI(20 K) (panel (b)), and high-power IMD slope (40 K) (panel (c)) for the samples indicated. The TOI-data were determined numerically (filled symbols) and graphically (open symbols) as explained in Sec. 3.3. The dashed and dotted lines illustrate a linear and logarithmic relation between TOI and J_c(50 K), respectively.

Figure 5 summarizes our results for I_{crit}(50 K), TOI(20 K), and m(40 K) versus the critical DC current density J_c(50 K). The different temperatures at which these parameters were evaluated are due to experimental considerations. They do not affect our conclusions, especially since we don't attempt a quantitative analysis of our results. The diagrams of Fig. 5 have two features in common: 1. We observe clear correlations between all three RF parameters and J_c, indicating that the physical significance of J_c persists well into the microwave region. 2. The samples of batch #1 fall apart from the general trends. This important result proves that good RF performance and good DC performance are not equivalent. We attribute the out-of-sequence results for batch #1 to the different annealing parameters compared to those used for batches #2 and #3. The annealing temperatures for the films of batch #1 remained below 400°C, and the final oxygenation level was approached from the as-grown state. In contrast, the films of batches #2 and #3 were sequentially de- and re-oxygenated by annealing in argon and activated oxygen, at temperatures up to 540°C. These differences certainly affect the density and homogeneity of oxygen vacancies, and hence the local variation of the superconducting order parameter. We are presently trying to reproduce the results for batch #1 with a new set of films, to achieve deeper insight into the mechanisms which are necessary to achieve good RF performance.

While the I_{crit}-J_c-correlation (top panel of Fig. 5) conforms to our intuitive expectation, the TOI-J_c-correlation (middle panel) is quite surprising. The TOI, expressed in units of dBm, should depend on the *logarithm* of J_c (dotted curve) if the IV-relation were given by a power-series. This is in contrast with the *linear* dependence of the TOI on J_c we observe (dashed curve). Our result implies that a simple power-series expansion with real coefficients is not sufficient to describe the nonlinear microwave response of HTS films. A possible solution of this dilemma is the assumption of an exponential IV-dependence like $V_{rf}(I_{rf} \propto \exp(I_{rf}/I_{scale})$, which could be associated with flux creep. However, such a speculation lacks theoretical justification at present. More sophisticated models of the IMD behavior are also under development.

Another surprising result is the systematic variation of the slope m with J_c (bottom panel of Fig. 5), which indicates that the IMD slope decreases for increasing sample quality. Such a variation of m is, again, not compatible with an IV-relation given by a power-series. Furthermore, slopes $m > 3$ seem to be possible (#3A and #3C), while the most strongly overdoped film #2C shows $m \sim 2$. A quadratic power dependence of P_{IMD} was previously observed for TlBaCaCuO films [17]. Such a behavior can result, theoretically, from a nonlinear surface impedance that depends on the modulus of the RF current, in sharp contrast to the quadratic behavior discussed in Sec. 3.2 [17,18]. The only physical mechanism known at present, which could lead to $\Delta Z_s(I_{rf}) \propto |I_{rf}|$, is the Yip–Sauls regime of d-wave superconductors, which can be experimentally accessed only at very low temperatures [18]. The persistence of $m < 3$ up to such high temperatures like 40 K is presently not understood but definitely deserves further attention.

4. NONLINEAR MICROWAVE RESPONSE OF MgO (T < 20 K)

In Sec. 3, $T = 20$ K was the lowest temperature analyzed. The reason for this choice is the occurrence of unexpected microwave properties below 20 K, which are associated with the nonlinear dielectric microwave impedance of MgO [3,19],

$$Z_d = \sqrt{\frac{\mu_0}{\varepsilon_0 \varepsilon_r}} \left(1 + \frac{1}{2} i \tan \delta\right). \tag{6}$$

As a consequence, the effective surface impedance Z_{eff}, according to Eqs. (1) and (2), can no longer be identified with Z_s of the superconductor, as in the previous section. Since our first observation and tentative interpretation in [3], we have refined our analysis and complemented by new results, as described in the following three subsections.

4.1. Temperature Dependence

Figure 6 summarizes typical results for the temperature dependence of Z_{eff}, measured for YBCO films on MgO. The different symbols represent the asymptotic behavior observed at very low and moderate power levels, respectively, as illustrated in more detail by the circles in Fig. 4. $R_{eff}(T)$ decreased at the higher power and approached 2 $\mu\Omega$. Expecting $R_s \geq 1\mu\Omega$, for high-quality epitaxial YBCO films [2], we estimate from the R_{eff}(20 K)-value an upper-limit for the loss tangent of about 10^{-6}, consistent with measured tan δ-data for MgO at 20 K [20,21]. At very low power, $R_{eff}(T)$ increased and became dominated by dielectric losses. This could be confirmed by the very similar temperature and power dependences of R_{eff} for Nb on MgO (see [3] and Figs. 7–9 below). Such an agreement for the two totally different

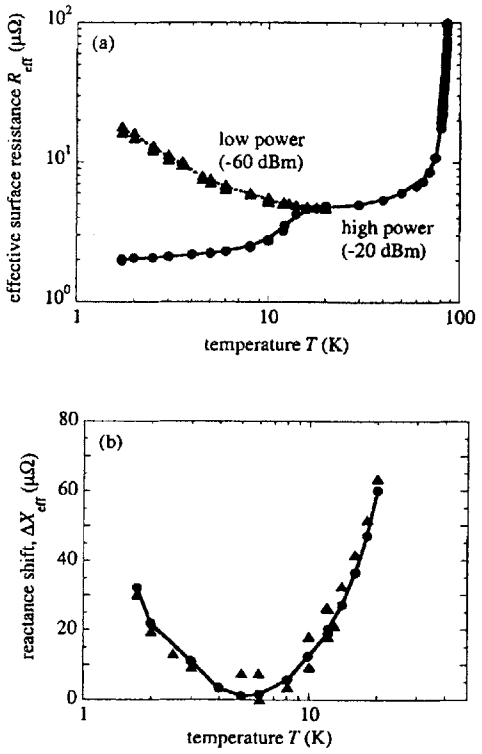

Fig. 6. Typical data for the effective surface resistance (panel (a)) and shift of surface reactance (panel (b)) at 2.3 GHz for YBCO on MgO at temperatures below 20 K. The different symbols and interpolation curves denote extreme power levels, as described in the text.

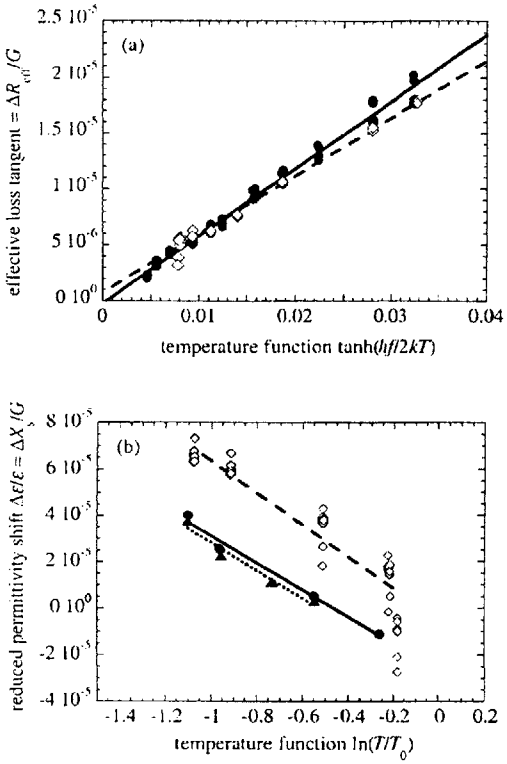

Fig. 7. Temperature dependent dielectric loss tangent (panel (a)) and permittivity (panel (b)) at $f = 2.3$ GHz for YBCO on MgO ($P_{in} = -60$ dBm: Triangles, dotted interpolation, $P_{in} = -20$ dBm: Circles, solid) and Nb on MgO (various power levels: Diamonds, dashed), as expected for resonant absorption. $T_0 = 5.2$ K. The $\Delta X_{eff}(T)$-data for Nb were corrected for the temperature variation of the superconducting penetration depth according to the BCS theory ($T_c = 9.2$ K, $\Delta(0)/kT_c = 1.8$).

superconductors on MgO, and the absence of this nonlinear behavior for other substrates like sapphire and $LaAlO_3$, proves that our observations are caused by the dielectric response of MgO. Using $R_s \sim 2\ \mu\Omega$ for YBCO and the effective value, $R_{eff} \sim 20\ \mu\Omega$, we derive $\tan\delta(1.7\text{ K}) \approx 2 \times 10^{-5}$, which is about 20 times above $\tan\delta(20\text{ K})$ (c.f., Fig. 7a).

Complementary to the loss tangent, the dielectric permittivity, monitored by changes of the effective surface reactance $\Delta X_{eff}(T)$, displayed a shallow minimum at $T \sim 5$ K, but remained independent of power up to moderate power levels (Fig. 6b and squares in Fig. 4). Reflecting again the growing influence of $Z_d(T)$ on $Z_{eff}(T)$ at low temperatures, the increase of $\Delta X_{eff}(T)$ in Fig. 6 can be entirely associated with the dielectric permittivity of MgO. Such an extremal behavior must not be confused with anomalous effects in the cuprate superconductor, which could be misinterpreted, e.g., as an indication of Andreev bound states at interfaces in d-wave superconductors [22].

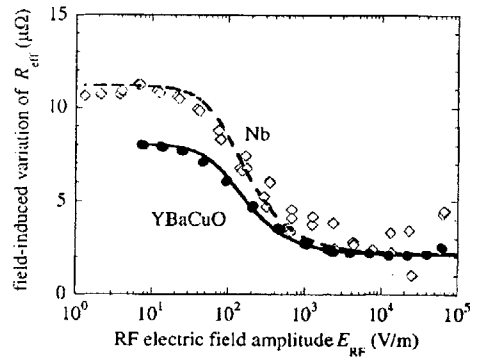

Fig. 8. Electric field-induced variation of the effective surface resistance for YBaCuO (circles) and Nb (diamonds) on MgO at $f = 2.3$ GHz and $T = 5$ K. The dashed and solid curves denote fits to Eq. (9).

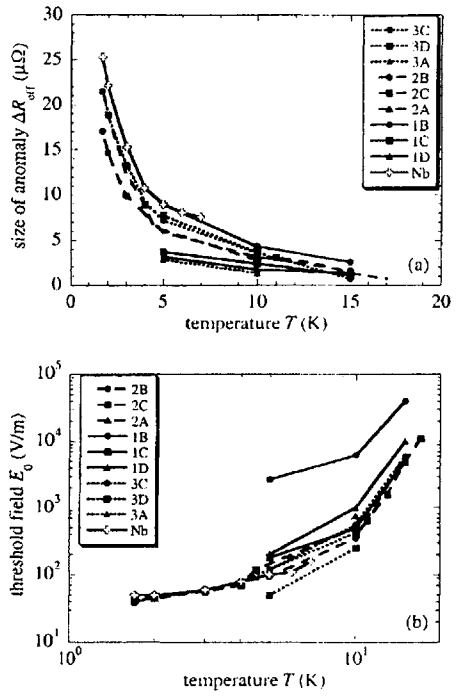

Fig. 9. Temperature dependences of the fit parameters ΔR_{eff} (panel (a)) and E_0 (panel (b)) for the power dependent loss tangent of MgO at $f = 2.3$ GHz and $T = 5$ K for the samples indicated in the legends (symbols and interpolation curves) c.f., Eq. (10).

4.2. Power Dependence

Figure 4 compares typical results for the power dependence of R_{eff}, ΔX_{eff}, and P_{IMD} at $T = 5$ K, here plotted versus input power. The R_{eff} decreased markedly as P_{in} increased, for the given resonator geometry and coupling above -60 dBm, reached a plateau around -40 dBm, and increased again at around -10 dBm. The difference between the low-power value of R_{eff} and its minimum increased strongly for decreasing temperature, in accordance with Fig. 6a. In contrast to the resistance, ΔX_{eff} was independent of power at low power and increased smoothly above -30 dBm. The increase of R_{eff} and ΔX_{eff} in the power range above -10 dBm is attributed to the nonlinear response of YBCO (Sec. 3). The IMD signal passed through a plateau in the region where R_{eff} decreased, and rose again more steeply where both X_{eff} and R_{eff} increased. It is worth noting that the frequency intermodulation, caused by the nonlinear loss tangent of MgO, is intimately related to R_{eff}. This is qualitatively different from the IMD behavior expected for the superconductor at high power or at $T > 20$ K, where P_{IMD} is usually dominated by the nonlinear reactance. Obviously, the dielectric microwave impedance of MgO induces enhanced frequency intermodulation, which could strongly degrade the performance of microwave devices.

4.3. Theoretical Description and Comparison Between YBCO/MgO and Nb/MgO

The unique temperature and power dependences of the dissipative and reactive response of MgO (Figs. 6 and 4) helped us to identify the underlying mechanism. Very similar features were observed for amorphous glasses and highly disordered crystalline solids in similar ranges of frequency and temperature [23,24]. The observed behavior was attributed to tunneling of atoms or molecules between nearly equivalent positions in the solid. This scientific area is subject to ongoing experimental and theoretical research [25]. Nevertheless, many features can be understood in the framework of a simple quantum mechanical two-level system. Phenomenologically, this model has similarities with the double-well potential underlying the Debye equations for dielectric relaxation [3,26]. The major difference between the two models is the resonant character of the transitions in the former, in contrast to the relaxational character in the latter. Dielectric resonances of isolated defects usually occur in the sub-mm wave range or at even higher frequencies, but recent theoretical studies have shown that clustering of defects can reduce the resonant frequencies very strongly, so that they may even reach into the microwave range [27].

The temperature dependence of the loss tangent can be easily derived from Fermi's golden rule. The temperature dependence of the dielectric permittivity, then, follows from that of $\tan\delta$ through the Kramers–Kronig-relation, which requires additional information on the frequency range over which resonances occur. Different results have to be expected for solids with rather dilute defects, where the resonances remain sharp and limited to a well-defined frequency interval, and for highly disordered systems. According to Ref. [24], one gets for resonant absorption

$$\tan\delta(T) = \frac{\pi}{\varepsilon_0\varepsilon_r} \times n_d\mu^2 \times \tanh\left(\frac{hf}{2kT}\right) \qquad (7)$$

for the dielectric loss tangent at low intensities, and

$$\frac{\Delta\varepsilon_r(T)}{\varepsilon_r} = \frac{\varepsilon_r(T) - \varepsilon_r(T_0)}{\varepsilon_r(T_0)} = -\frac{2}{\varepsilon_0\varepsilon_r} \times n_d\mu^2 \times \ln\left(\frac{T}{T_0}\right) \qquad (8)$$

for the fractional change of the permittivity in highly disordered systems, with T_0 a reference temperature. In Eqs. (7) and (8), n_d and μ describe the density and the electric dipole moment of the defects. The frequency dependences of $\tan\delta$ and $\Delta\varepsilon_r/\varepsilon_r$ will be different if relaxation effects have to be taken into account additionally.

The two-level model also explains in a natural way the anomalous power dependence, as resulting from saturation effects due to enhanced population of the higher energy level for increasing intensity of the microwave field. To derive the power dependence of the complex permittivity requires a more sophisticated mathematical framework, which bears similarities with the Bloch-equations for a spin-1/2–particle in a magnetic field [23]:

$$\tan\delta(S_{rf}) = \tan\delta(0) \times \left(1 + \frac{S_{rf}}{S_0}\right)^{-1/2}, \qquad (9)$$

where S_{rf} denotes the intensity of the RF field, $S_{rf} \propto E_{rf}^2$, and the real part of the permittivity is independent of power. The threshold intensity S_0 depends on μ but not on n_d. It bears also information on the characteristic relaxation times of the excited defect states [24]. In Ref. [3], the interpretation of the anomalous power dependence of $\tan\delta$ in terms of a microwave field-dependent dielectric relaxation time was obviously oversimplified. Equation (9) provides a more accurate explanation, connecting the experimental data now with a microscopic mechanism.

We compare our experimental results with the theoretical expectation in Figs. 7 and 8. In Fig. 7a we have plotted the difference between the two curves shown in Fig. 6a, normalized by G, versus the temperature function expected from Eq. (7). We have also included in this figure our results for an Nb film on MgO (diamonds). Both data sets are consistent with the expected linear relationship. The similar slopes indicate very similar properties, $n_d\mu^2$, of the MgO substrates, although these were bought from different suppliers. Fig. 7b shows the corresponding result for the fractional variation of ε_r expected from Eq. (8). The data derived for the YBCO film were not corrected for changes of the superconducting penetration depth, since $\lambda(T)$ can be safely assumed to be constant below 20 K. The situation is different for Nb with $T_c = 9.2$ K, where we accounted for $\Delta\lambda(T)$ according to BCS theory. As for the loss tangent, we find very similar results for both superconductors. The slopes in Figs. 7a and 7b, which should differ for a highly disordered system by a factor of $-\pi/2 \sim -1.6$, differ by $-5.5 \times 10^{-4}/6.5 \times 10^{-5} \sim -8.5$. The difference of a factor of $\sim$5 is attributed to the nature of the defects in a highly crystalline material like MgO.

A typical measured power dependence of $\tan\delta$ is compared with Eq. (9) in Fig. 8 for a YBCO film and an Nb film, both on MgO. The symbols represent the measured data, the curves denote the result of a single-parameter fit

$$R_{eff}(E_{rf}) = R_s + \Delta R_{eff} \times \left(1 + \frac{E_{rf}^2}{E_0^2}\right)^{-1/2}, \qquad (10)$$

which is equivalent to Eq. (9). The parameters R_s and ΔR_{eff} are given by the experimental data, while E_0 can be varied within a narrow range to optimize the fit. The data in Fig. 8 indicate similar E_0-values for the two types of films on MgO substrates used, which implies similar types of defects. The ΔR_{eff}-values for Nb/MgO seem a bit higher than for YBCO/MgO, which could hint for a larger defect density in the substrate.

Finally, in Fig. 9, we summarize the temperature dependences of ΔR_{eff} (panel a) and E_0 (panel b) for all samples studied. Figure 9a illustrates the increase of the loss tangent for decreasing temperatures. All samples lead to comparably high and temperature dependent ΔR_{eff}-values, except for two films of batch #1 (C and D), and the as-grown film #3A. It is tempting to attribute this behavior to the different annealing schedules (see discussion in Sec. 3.3), as these can well change the density of defects in MgO. Possible candidate defects were identified in Ref. [19] to be OH^--ions, which can be released from grain boundaries upon heating. Further studies are planned to verify our assumption.

The temperature variation of E_0 displayed in Fig. 9b results mainly from the temperature-dependent relaxation times of the defects in MgO. There is only one exceptional result among all others, namely for #1B. The reason for this peculiarity is not known at present. Complementary experiments like specific-heat measurements are required to extract more detailed information on the defect density and, in turn [24], the relaxation times of the defects in MgO that cause the nonlinearities.

5. CONCLUSIONS

We have investigated the nonlinear microwave properties of electron-beam coevaporated $YBa_2Cu_3O_{7-x}$ films on MgO of varying oxygen content, at 2.3 GHz and temperatures 1.7–80 K. Above

20 K, the nonlinear response of the resonators was dominated by the HTS films for both substrate materials. We have established clear correlations between the onset of nonlinear R_S, the dependence of P_{IMD} on the oscillating power P_{osc}, and the oxygen deficiency x of the YBCO films. With increasing x, the critical currents and third-order intercepts decreased, while the exponent of the power-law relation between P_{IMD} and P_{osc} increased from 2 to 3. This observation defines a route to optimize the linear response of HTS films for microwave applications. Beside overdoping by adjusting the oxygenation level, Ca-doping could be another promising approach, which is presently under investigation (see also [28]).

In MgO, at temperatures below 20 K, the dielectric loss tangent was found to dominate the nonlinear response of the resonators. The dissipation losses decreased with increasing power by up to one order of magnitude. This anomaly was accompanied by enhanced IMD. The surface reactance passed through a shallow minimum at about 5 K, but remained independent of power. The results were very similar for all investigated YBaCuO films as well as for Nb films on MgO made for reference. We attribute these effects to resonant absorption by impurity states in MgO. While proper identification of the impurities is lacking at present, OH^--ions are considered the most likely candidates, since they are greatly abundant in melt-fused MgO.

ACKNOWLEDGMENTS

We gratefully acknowledge valuable contributions from J. Derov, P. Droste, T. Dahm, C. Enss, B. Henderson, S. Hunklinger, K. Peters, and D. Seron. The work at QinetiQ was supported by the MOD (UK). The work at Lincoln Laboratory was supported by the AFOSR (U.S.A.). The work at Wuppertal was supported by the European Office of Aerospace Research and Development, AFOSR/AFRL, under Contract No. F61775–01–WE033.

REFERENCES

1. See, e.g., other contributions to this symposium.
2. M. A. Hein, *High-Temperature Superconductor Thin Films at Microwave Frequencies*, (Springer Tracts of Modern Physics, Vol. 155) (Springer, New York, 1999).
3. M. A. Hein *et al.*, *Appl. Phys. Lett.* **80,** 1007 (2002).
4. M. J. Lancaster, *Passive Microwave Device Applications of High-Temperature Superconductors* (Cambridge University Press, Cambridge, United Kingdom, 1997).
5. R. G. Humphreys *et al.*, *Mater. Sci. Eng. B* **10,** 293 (1991).
6. N. G. Chew *et al.*, *Appl. Phys. Lett.* **57,** 2016 (1990).
7. S. Orbach-Werbig, Dissertation, University of Wuppertal, Report WUB-DIS 94-9, (in press); N.G. Chew *et al.*, *IEEE Trans. Appl. Supercond.* **5,** 1167 (1995).
8. The niobium was deposited as described in K.K. Berggren *et al.*, *IEEE Trans. Appl. Supercond.* **9,** 3271 (1999).
9. D. E. Oates *et al.*, *IEEE Trans. Microwave Theory Tech.* **39,** 1522 (1991).
10. D. M. Sheen *et al.*, *IEEE Trans. Appl. Supercond.* **1,** 108 (1991).
11. P. P. Nguyen *et al.*, *Phys. Rev. B* **48,** 6400 (1993).
12. M. A. Hein, M. Perpeet, and G. Müller, *IEEE Trans. Appl. Supercond.* **11,** 3434 (2001).
13. A. A. Golubov *et al.*, in *Applied Superconductivity 1997*, (IOP Conference Series, No. 158) H. Rogalla and D. H. A. Blank, eds. (IOP Publishing, Bristol, United Kingdom, 1997), pp. 463–466.
14. J. Halbritter, *J. Supercond.* **11,** 231 (1998).
15. A. N. Grigorenko *et al.*, *Appl. Phys. Lett.* **78,** 1586 (2001).
16. J. S. Booth *et al.*, *J. Appl. Phys.* **86,** 1020 (1999).
17. B. A. Willemsen, K. E. Kihlstrom, and T. Dahm, *Appl. Phys. Lett.* **74,** 753 (1999).
18. T. Dahm and D. J. Scalapino, *Phys. Rev. B* **60,** 13125 (1999).
19. B. Henderson and W. A. Sibley, *J. Chem. Phys.* **55,** 1276 (1971).
20. J. Krupka, R. G. Geyer, M. Kuhn, and J. H. Hinken, *IEEE Trans. Microwave Theory Tech.* **42,** 1886 (1994).
21. T. Konaka, M. Sato, H. Asano, and S. Kubo, *J. Supercond.* **4,** 283 (1991).
22. H. Walter *et al.*, *Phys. Rev. Lett.* **80,** 3598 (1998); A. Carrington *et al.*, *Phys. Rev. Lett.* **86,** 1074 (2001).
23. S. Hunklinger and M. von Schickfus, in *Amorphous Solids*, W. A. Phillips, ed. (Springer, New York, 1981), pp. 81–105.
24. U. Strom, M. von Schickfus, and S. Hunklinger, *Phys. Rev. Lett.* **41,** 910 (1978).
25. S. Hunklinger and C. Enss, in *Insulating and Semiconducting Glasses*, (Series of Directions in Condensed Matter Physics, Vol. 17) P. Boolchand, ed., (World Scientific, Singapore, 2000), p. 499.
26. V. V. Daniel, *Dielectric Relaxation* (Academic Press, New York, 1967).
27. M. W. Klein, *Phys. Rev. B* **40,** 1918 (1989).
28. D. E. Oates, M. A. Hein, P. J. Hirst, R. G. Humphreys, G. Koren, and E. Polturak, *Physica C* **372–376,** 462 (2002).

INSTITUTE OF PHYSICS PUBLISHING SUPERCONDUCTOR SCIENCE AND TECHNOLOGY
Supercond. Sci. Technol. 17 (2004) S290–S294 PII: S0953-2048(04)71777-7

Temperature dependence of intermodulation distortion in YBCO

D E Oates[1], S-H Park[1,2], D Agassi[3] and G Koren[4]

[1] MIT Lincoln Laboratory, Lexington, MA 02420, USA
[2] MIT Department of EECS, Cambridge, MA 02139, USA
[3] Naval Surface Warfare Center, Carderock Division, Bethesda, MD 20817, USA
[4] Technion—Israel Institute of Technology, Haifa 32000, Israel

Received 20 October 2003
Published 6 April 2004
Online at stacks.iop.org/SUST/17/S290 (DOI: 10.1088/0953-2048/17/5/039)

Abstract
Measurements of the intermodulation distortion (IMD) as a function of temperature from 1.7 K to T_c in $YBa_2Cu_3O_{7-\delta}$ are presented. Films of the highest quality show an increase in IMD as the temperature decreases for temperatures below approximately 30 K. Films of lower quality do not show the increase in the temperature range measured. The increase is in qualitative agreement with that predicted by the nonlinear Meissner effect in d-wave superconductors. The temperature dependence of the measurements is compared with a new calculation of the nonlinear penetration depth.

1. Introduction

Nonlinear effects are still one of the limits to more widespread application of high-T_c materials in microwave frequency devices. Two-tone intermodulation distortion (IMD) is a deleterious effect observed in all superconducting materials, especially high-T_c superconductors. In practical devices such as filters, the IMD can degrade performance, even at relatively low power for filters with narrow bandwidth or very sharp skirts. The IMD is likely to arise from the same nonlinear current–voltage characteristic that also leads to the nonlinear surface impedance. Understanding of its origins, however, is lacking. It has been generally accepted that measured IMD is larger than intrinsic values inferred from theoretical considerations [1].

In the HTS materials it is well known that intrinsic nonlinearities are present. Dahm and Scalapino showed in a series of papers [2, 3] that the intrinsic nonlinear properties of the HTS materials would lead to IMD. It was found that the predicted IMD would increase at low temperatures due to the nonlinear Meissner effect [4]. Until now these effects of intrinsic nonlinearities have not been observed experimentally. It is likely that extrinsic nonlinearities arising from defects in the films were larger than the intrinsic effects and effectively masked the behaviour of the intrinsic effects. In this report, we demonstrate the upturn of IMD at low temperature in the best-quality films and show how films with more fabrication defects do not show evidence for the intrinsic behaviour.

The demonstration of intrinsic nonlinearities obviously has important consequences for practical devices. Although the measurements reported here concentrate on the low-temperature IMD, the performance at cryocooler temperatures can still be limited by the intrinsic values. However, we conclude that even the best-quality films measured in this study may not exhibit IMD at the intrinsic limit. A significant component of extrinsic nonlinearity might still be present at the temperatures of operation of practical devices.

2. Experiment

2.1. Films

The IMD measurements reported here have been carried out with six films from various sources. All of the films were YBCO and some had dopants added during the growth process. Table 1 gives the details of the films.

2.2. Surface impedance measurement

The films were patterned using standard photolithography and wet etching, were assembled with ground planes to form stripline resonators, and measured by a technique that has been described previously [8, 9], in which the Q and resonant frequency f_0 of the resonator are measured as a function of the microwave power at various temperatures between 1.7 K and T_c. The results are converted into the effective surface resistance $R_S(I_{rf})$ and reactance $X_S(I_{rf})$ where I_{rf} is the microwave current. The measurements were made at the fundamental frequency of 1.5 GHz for the case of the $LaAlO_3$ substrates and 2.3 GHz for the Al_2O_3 substrate.

Table 1. Details of the films used in IMD measurements.

Number	Film type	Substrate	Deposition method	Source
1	$YBa_2Cu_3O_{7-\delta}$	$LaAlO_3$	Pulsed laser deposition (PLD)	Koren [5]
2	$YBa_2Ni_{0.06}Cu_{2.94}O_{7-\delta}$	$LaAlO_3$	PLD	Koren
3	$YBa_2Zn_{0.06}Cu_{2.94}O_{7-\delta}$	$LaAlO_3$	PLD	Koren
4	$Y_{0.7}Ca_{0.3}Ba_2Cu_3O_{7-\delta}$	$LaAlO_3$	PLD	Koren
5	$YBa_2Cu_3O_{7-\delta}$	$LaAlO_3$	Sputtered	Anderson [6]
6	$YBa_2Cu_3O_{7-\delta}$	Al_2O_3	PLD	Lorenz [7]

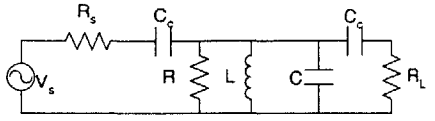

Figure 1. Equivalent circuit of a resonator. R, L, and C are given by the transmission line parameters [12]. C_c is the coupling capacitor and $R_s = R_L$ are the load and source impedances = 50 Ω.

2.3. Intermodulation distortion measurement

The same resonator as used for the Z_S measurements is used for the IMD measurements. The third-order IMD was measured in the usual way, in which two closely spaced tones of equal power at frequencies f_1 and f_2 are combined and applied to the resonator. The frequencies are centred about the resonant frequency and within the 3 dB bandwidth of the resonator, determined from the earlier measurements of Q. A tone separation Δf of approximately 1/32 of the low-power 3 dB bandwidth was used. The tone separation was adjusted at each temperature to maintain the same relationship to the bandwidth. The third-order mixing products at frequencies $2f_1 - f_2$ and $2f_2 - f_1$ are then measured in a spectrum analyser as a function of the input power to the resonator.

3. Experimental results and analysis

3.1. Normalization of IMD for different films

Since we have measured resonators with different Q values, resonant frequencies, characteristic impedance, and coupling factors, all of which influence the absolute value of the IMD, it is necessary to normalize the directly measured values of the IMD power. We make the usual assumption that the IMD arises from the nonlinear surface impedance, and that the nonlinear inductance dominates the generation of the IMD [3].

Expressions for the IMD power, given a value of the nonlinear inductance, have been derived by several authors [3, 10, 11]. If one assumes that the nonlinear inductance is given by

$$L = L_0 + L_2 I^2, \tag{1}$$

where L is the inductance in the equivalent circuit of the resonator shown in figure 1 [12], L_2 is a constant, and I^2 is the total rf current in the resonator, the expression for the IMD power P_{IMD} is [11]

$$P_{\mathrm{IMD}} = \left(\frac{3}{4}\right)^2 \omega^2 L_2^2 \frac{(2r_v(1-r_v))^4 Q_c^4 P^3}{\pi^2 Z_0^4} \tag{2}$$

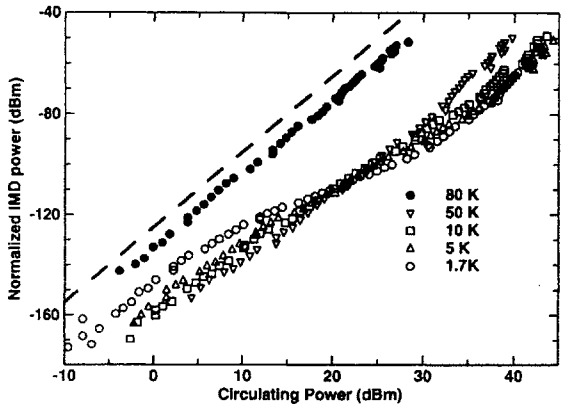

Figure 2. IMD versus circulating power for selected temperatures. This is for film no 1, the PLD $YBa_2Cu_3O_{7-\delta}$ on LAO. The dashed line illustrates slope 3 which is an indication of a P_{circ}^3 dependence. See equations (2) and (4).

where ω is the angular frequency, r_v is the voltage insertion ratio, related to the insertion loss IL in dB by

$$r_v = 10^{-\frac{IL}{20}}, \tag{3}$$

Q_c is the unloaded Q, P is the input power, and Z_0 is the characteristic impedance of the resonator. Thus, to compare different resonators, the IMD data are scaled by the factors involving r_v, Q_c, and Z_0. This scaling is also used to compare different temperatures in the same resonator, since the Q and r_v change with temperature. The other derivations of equation (2) [3, 10] give the same functional form for the power of the IMD as a function of the experimental quantities ω, L_2, r_v, Q_c, P and Z_0. They differ only by multiplicative constants. This difference does not matter here because we are making relative comparisons.

It is also most illustrative to plot the IMD results versus the circulating power in the resonator. The circulating power is given by

$$P_{\mathrm{circ}} = \frac{4r_v(1-r_v)Q_c P}{\pi^2}, \tag{4}$$

and then

$$P_{\mathrm{norm}} = \frac{P_{\mathrm{IMD}}}{r_v(1-r_v)Q_c}, \tag{5}$$

where P_{norm} is the normalized IMD power that is used to compare the data from various resonators.

3.2. IMD results

3.2.1. Power dependence. Figure 2 shows the measurements of the IMD as a function of the circulating power in the

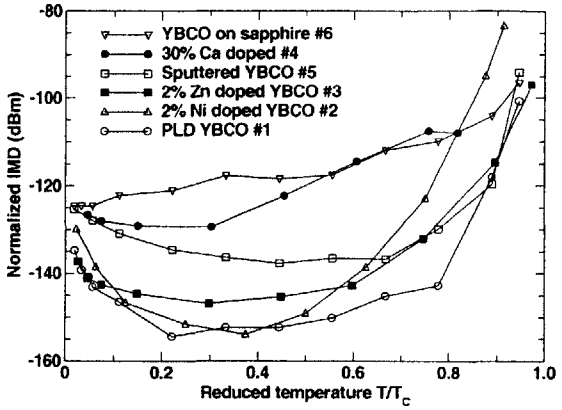

Figure 3. Measurements of the IMD at the fixed circulating power of 5 dBm for the various films listed in table 1. ○ YBCO no 1, △ Ni doped YBCO no 2, ■ Zn doped YBCO no 3, ● Ca doped YBCO no 4, □ sputtered YBCO no 5, ▽ YBCO on sapphire no 6.

resonator for the pulsed laser deposited (PLD) $YBa_2Cu_3O_{7-\delta}$ film, no 1 in table 1, for several temperatures. The behaviour as a function of power is quite complex. The simple ansatz of equation (1) predicts a dependence on circulating power of $P_{IMD} \sim P_{circ}^3$ yielding a slope of three in a log–log plot. This simple dependence is only shown in isolated parts of the power range. A dashed line in figure 2 shows a slope of three and is included as a reference. At low powers the dependence is of slope three, but at intermediate power the slope changes over to two for the lowest temperatures and subsequently at the highest powers the slope become three once again. Note that at the lowest powers the normalized IMD *increases* as the temperature decreases. This is counter to the normal expectation that superconductivity improves as the temperature is lowered.

For temperatures below approximately 70 K, the curves merge at approximately 20 dBm circulating power. The curves merge because the lower-temperature values, after initially showing slope three, change over to a slope-two regime. The slope-two behaviour is an indication that the simple ansatz of equation (1) no longer holds and the behaviour shows a modulus dependence on current, that is,

$$L = L_0 + L_2 |I| . \tag{6}$$

This will be discussed in more detail in section 4. At powers higher than the intersection point the slope becomes three once again, and the temperature dependence is approximately what one would expect, in that the IMD is monotonically increasing with increasing temperature.

3.2.2. Temperature dependence. Figure 3 shows the temperature dependence of the measured IMD at low power for the collection of films that is shown in table 1. Plotted is the IMD, scaled as described above, versus the reduced temperature. To obtain these data, each of the films was characterized like PLD YBCO film no 1 shown in figure 2. The actual range of temperature is from 1.7 to 85 K. These data were extracted from the IMD-versus-power measurements for each film at a circulating power of approximately 5 dBm.

The film with the lowest IMD at the middle temperature range, which is thus the highest-quality film, PLD YBCO no 1, shows a significant upturn at low temperatures. This is the film shown in figure 2. The other films show either a smaller upturn or none at all in the case of the YBCO film on sapphire and the Ca doped film. All films, however, show a tendency to arrive at the same low-temperature IMD. The high-temperature values also tend to merge to similar levels. A possible explanation for the lack of, or smaller, upturn at low temperatures seen in some of these films is the presence of defects or impurity dopants. Films on sapphire are known to have more defects, and in particular microcracks, than YBCO films on other substrates. The sputtered film, no 5, was also judged to be of lower quality than the best sputtered films. This was the conclusion of Z_S measurements on this film. Other sputtered films, not shown, from the same 5 cm diameter wafer showed almost identical behaviour.

3.3. IMD measurements on niobium

To verify our results on YBCO, comparable measurements were made on a resonator fabricated from a sputtered niobium film [13] on an $LaAlO_3$ substrate. It is predicted [2, 3] that s-wave superconductors show an IMD power decreasing exponentially at low temperatures, because of the finite energy gap. The IMD data versus temperature indicate that niobium does not show an upturn, and becomes independent of temperature at low T as might be expected if it is limited by extrinsic effects. However, the measurements on niobium do not reach the same reduced temperature as YBCO because of the lower T_c. The data are not of low enough reduced temperature to show unambiguously the expected s-wave behaviour. To fully verify the theory, lower-temperature measurements should be performed. However, the most important result of the niobium IMD measurements is that the temperature-independent IMD response rules out any substrate effects in the observed increase of IMD in YBCO at low temperatures.

4. Comparison with intrinsic d-wave theory

4.1. Theory of d-wave nonlinearity

To compare the data with theory, calculations of the lowest-order correction to the penetration depth have been carried out. The calculation derives the third-order response of a d-wave superconductor to a transversal microwave field under the assumption of a global equilibrium temperature. This is achieved by starting from the Gorkov equations and analytic evaluation of the proper terms in the Green function perturbative expansion [14]. Several simplifying approximations are made; in particular, frequency dependence is neglected in keeping with experimental evidence. The final expression is without free parameters except for a factor whose range is strictly limited. This approach yields a spatially independent penetration-depth expansion in terms of the averaged current density

$$\lambda(T, j) = \lambda_0(T) + \lambda_2(T) j^2 \tag{7}$$

where T is the temperature, j is the current density, and λ_2 is the nonlinear part of the penetration depth. The material

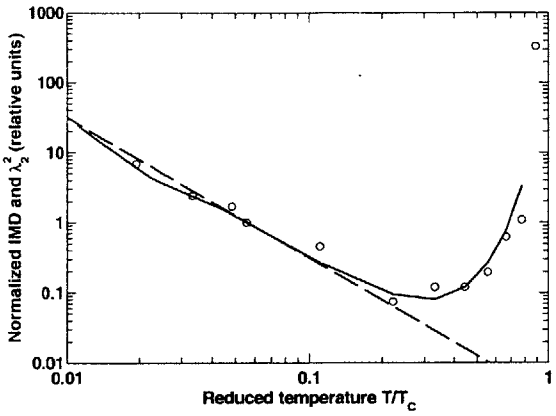

Figure 4. Comparison of data and theory. The open circles are the IMD data from film no 1. The solid curve is the calculation of d-wave theory. The dashed line depicts a slope of two.

parameters of the superconductor that were used are $T_c = 90$ K, $\lambda_0 = 0.2$ μm, and the energy gap $\Delta(0) = 3kT_c$. The result of equation (7) is the same functional form as that obtained by Dahm and Scalapino [3]. As discussed below, the predicted low-temperature behaviour of the IMD using our calculation is the same as that predicted by Dahm and Scalapino.

As discussed in [3] the IMD of a resonator is proportional to λ_2^2 of the material in the resonator. This is plotted in relative units as the solid curve in the log–log plot in figure 4 as a function of the reduced temperature T/T_c. The long-dashed line of figure 4 is proportional to $1/T^2$, which seems to agree well with the asymptotic behaviour of the calculation at low temperatures. Calculations by Dahm and Scalapino [2] produce very similar behaviour, with the same $1/T^2$ divergence at low temperatures.

4.2. Temperature dependence

Figure 4 also shows, as the open circles, the measured IMD of PLD YBCO film no 1 measured at a circulating power of 5 dBm, as a function of the reduced temperature. This is the highest-quality film of those shown in figure 3. The IMD is plotted in relative units. These data are not too sensitive to the exact value of the circulating power used to generate the plot because, as seen in figure 2, the different temperature curves are parallel in the low-power region. The temperature dependence of the measured data agrees well with the calculations that we have performed in that both show very similar $1/T^2$ behaviour at low temperature. These data also agree well with the model of Dahm and Scalapino [2, 3]. Thus the data agree with models of d-wave superconductors. This increase in λ_2 and IMD at low temperature is the signature of the nonlinear Meissner effect. Measurements at lower temperatures might be important to determine how low in temperature this dependence on T persists. It is obvious that the other films depicted in figure 3 do not agree well with the theory. The origins of the disagreement are discussed in the following section.

5. Discussion

We are convinced that the experimental data presented here are a result of the nonlinear electrodynamics of the YBCO material and not a result of heating, which has been ruled out as discussed in earlier publications from this group [15]. The sample is measured in a helium exchange-gas atmosphere, and other checks have been carried out, such as observing the same measured results with power increasing and with power decreasing. We have also compared frequency-domain and time-domain measurements of the surface impedance and seen no difference. Most importantly, the significant results of this paper concern the behaviour at very low power. The data of figure 4, for example, were measured with circulating powers of 5 dBm, which implies a dissipated power of -45 dBm in a resonator with a Q of 10^5. This level of dissipated power will not cause any significant temperature rise.

The effects of stress due to the mismatch in thermal expansion between the film and substrate are not considered to be important in the temperature dependence of the IMD in the temperature range presented here. We expect that the change in stress due to thermal expansion mismatch is minimal at low temperatures because almost all of the thermal expansion takes place between elevated temperatures and approximately 40 K. Thus, while the films may well be under stress due to mismatch of thermal expansion of the substrate and film between the growth and the operating temperature, we believe that changes in stress between 30 and 1.7 K are minimal and do not affect our conclusions.

While an earlier report [16] showed an indication of an increase in IMD at low temperatures, we believe that the data presented here are the observation of the nonlinear Meissner effect, which is the intrinsic nonlinearity resulting from the d-wave symmetry of the order parameter of the HTS materials. Most of the data of figure 3 show a significant departure from the theoretical behaviour. The departure can be explained by assuming that the measured IMD is the sum of the intrinsic values, calculated as outlined in section 4.1, and an extrinsic term that exhibits weak temperature dependence at low temperatures. The origin of the extrinsic term is not identified at this time but could arise from defects and impurities as suggested by the data from the Zn and Ni doped films. That the sapphire film shows no minimum and actually shows a slight decrease in IMD as the temperature approaches the lowest measured here is also very suggestive, since films on sapphire are known to contain more defects than those on LAO due to the large mismatch in thermal expansion between YBCO and sapphire. It is also true that the films showing weak or no minimum in the IMD-versus-T behaviour showed higher surface resistance and larger λ_0 than the best film, which shows the deepest minimum.

This hypothesis of an extrinsic contribution with very weak temperature dependence also explains the tendency of the data to approach a convergence point at very low temperatures. Because of the $1/T^2$ divergence of the intrinsic IMD at sufficiently low temperatures, all films will eventually exhibit a dominant intrinsic contribution. This naturally suggests that measurements at lower temperatures could be definitive in supporting this speculation.

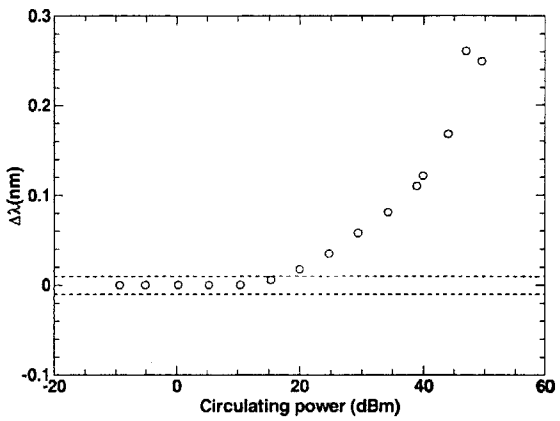

Figure 5. Penetration depth versus circulating power.

The measurements presented here have used the IMD to observe the nonlinear Meissner effect. This can be considered an indirect way to measure the effect because the IMD is proportional to the square of the nonlinear part of the penetration depth λ_2. It is in principle possible to measure λ_2 directly. In the resonator measurements this can be done by measuring the change of resonant frequency as a function of the microwave current. From this change in frequency, we can make an estimate of the change in penetration depth in the usual way [17] by assuming a uniform change in λ across the resonator centre conductor.

Figure 5 shows $\Delta\lambda$ versus circulating power for laser ablated film no 1 at 1.7 K. These values of $\Delta\lambda$ were derived from the measured change in resonant frequency versus circulating power. The dotted lines show changes in λ of 0.01 nm. This amount of change is only seen for circulating powers greater than 20 dBm, and below that power no measurable change in λ can be seen. To see the increase of IMD shown in figure 4, we presented the data from the IMD measurements in figure 2 at a circulating power of 5 dBm. At 20 dBm circulating power in figure 2, the low-temperature increase of IMD is not evident. Thus, at the power level where the increase in IMD at low temperature is seen (5 dBm), figure 5 shows that the changes in penetration depth are smaller than the experimental resolution. Thus, if we relied on the measured $\Delta\lambda$, we would not have seen the low-temperature increase of nonlinearity that is the signature of the nonlinear Meissner effect. Another way to understand the situation is to realize that we are measuring changes in λ of one part in 10^5. Since λ at low temperatures is proportional to T, this implies that a necessary condition for a direct measurement with this resolution is a temperature stability of the same amount. Thus the IMD measurements, although indirect, are a very sensitive method to measure the nonlinear penetration depth.

6. Conclusions

We have observed clear evidence of the nonlinear Meissner effect in YBCO thin films by measurements of the IMD as a function of temperature extended to low temperatures. This is an indication that we are observing intrinsic nonlinearities in the HTS materials. The films also show evidence of extrinsic effects as well. For the best film, comparisons with theory yield good agreement with the temperature dependence. Other films show a low-temperature increase in IMD, but significant departures from the theory result from extrinsic contributions to the IMD.

Acknowledgments

This work was supported by the Air Force Office of Scientific Research. We thank A C Anderson and M Lorenz for supplying films used in this study. We thank R P Konieczka and D Baker for technical support, and G Fitch for computer programming.

References

[1] Dahm T, Scalapino D J and Willemsen B A 1999 *J. Supercond.* **12** 339–42
[2] Dahm T and Scalapino D J 1999 *Phys. Rev.* B **60** 13125–30
[3] Dahm T and Scalapino D J 1997 *J. Appl. Phys.* **81** 2002–9
[4] Yip S K and Sauls J A 1992 *Phys. Rev. Lett.* **69** 2264–7
[5] Koren G, Levy N, Polturak E and Koral Y 2000 *Appl. Supercond.* **2** 303–6
[6] Anderson A C, Slattery R L, Oates D E and Yu-Jahnes L S 1993 *Solid State Research Quarterly Technical Report* Lincoln Laboratory, Lexington, MA, vol 2, pp 31–3
[7] Lorenz M, Hochmuth H, Natusch D, Tharigen T, Svetchnikov V L, Zandbergen H W, Schafer C, Kastner G and Hesse D 2000 *Mater. Res. Soc. Symp. Proc.* **603** 163–8
[8] Oates D E, Nguyen P P, Dresselhaus G, Dresselhaus M S, Koren G and Polturak E 1995 *J. Supercond.* **8** 725–33
[9] Oates D E and Anderson A C 1991 *IEEE Trans. Magn.* **27** 867–71
[10] Vopilkin E A, Parafin A E and Reznik A N 2000 *Tech. Phys.* **45** 214–20
[11] Oates D E 2003 unpublished
[12] Oates D E, Anderson A C and Mankiewich P M 1990 *J. Supercond.* **3** 251–9
[13] Berggren K K, Macedo E M, Feld D A and Sage J P 1999 *IEEE Trans. Appl. Supercond.* **9** 3271–4
[14] Agassi D and Oates D E 2003 *J. Supercond.* **16** 905–11 Agassi D and Oates D E 2004 to be submitted
[15] Xin H, Oates D E, Anderson A C, Slattery R L, Dresselhaus G and Dresselhaus M S 2000 *IEEE Trans. Microw. Theory Tech.* **48** 1221–6
[16] Benz G, Wünsch S, Scherer T A, Neuhaus M and Jutzi W 2001 *Physica* C **356** 122–8
[17] Oates D E 2001 *Microwave Superconductivity (NATO ASI Series)* ed H Weinstock and M Nisenoff (Dordrecht: Kluwer)

Bibliography

[1] M. Cyrot and D. Pavuna. *Introduction to superconductivity and high-T_c materials.* World Scientific, River Ridge, New Jersey, 1992.

[2] T. Van Duzer and C. W. Turner. *Principles of Superconductive Devices and Circuits*, page 132. Prentice Hall PTR, Upper Saddle River, NJ, second edition, 1999.

[3] A. B. Pippard. An experimental and theoretical study of the relation between magnetic field and current in a superconductor. *Proc. Roy. Soc (London)*, A216(7):547–568, Feb. 1953.

[4] T. P. Orlando and K. A. Delin. *Foundations of Applied Superconductivity.* Addison-Wesley Publishing Company, Inc., Reading, Massachusetts, 1991.

[5] A. A. Abrikosov. On the magnetic properties of superconductors of the second group. *JETP*, 5(6):1174–1182, Dec. 1957.

[6] M. Tinkham. *Introduction to superconductivity.* McGraw-Hill, New York, second edition, 1996.

[7] J. Bardeen, L. N. Cooper, and J. R. Scheriffer. Theory of superconductivity. *Physical Review*, 108(5):1175–1204, Dec. 1957.

[8] B. D. Josephson. Possible new effects in superconductive tunneling. *Physics Letters*, 1(7):251–253, Jul. 1962.

[9] P. M. Anderson and J. M. Rowell. Probable observation of the Josephson superconducting tunneling effect. *Phys. Rev. Lett.*, 10:230–232, Mar. 1963.

[10] G. Bednorz and K. A. Müller. Possible high T_c superconddductor. *Z. Phys.*, B64(189):251–253, Jul. 1986.

[11] A. M. Portis. *Electrodynamics of High-Temperature Superconductors.* World Scientific, Singapore, 1993.

[12] A. M. Kadin. *Introduction to Superconducting Circuits.* John Wiley & Sons, Inc., New York, second edition, 1998.

[13] M. J. Lancaster. *Passive microwave device applications of high-temperature superconductors.* Cambridge University Press, Cambridge, 1997.

[14] W. G. Lyons, R. S. Withers, J. M. Hamm, A. C. Anderson, P. M. Mankiewich, M. L. O'Malley, R. E. Howard, R. R. Bonetti, and A. E. Williams. High-temperature superconductive passive microwave devices. *IEEE MTT-S Digest*, pages 1227–1230, 1991.

[15] D. M. Pozar. *Microwave Engineering.* John Wiley & Sons, Inc., New York, second edition, 1998.

[16] D. E. Oates. *Nonlinear Behavior of Superconducting Devices*, volume 375 of *Microwave Superconductivity, NATO Science Series E: Applied Sciences*, chapter 5, pages 117–148. Kluwer Academic Publishers, Dordrecht, The Netherlands, 2001.

[17] J. W. Wosik, L. M. Xie, K. Nesteruk, D. Li, J. H. Miller, Jr., and S. A. Long. Power handling capabilities of superconducting YBCO thin films: thermally induced nonlinearity effects. *J. Supercond.*, 10(2):97–107, 1997.

[18] S. K. Yip and J. A. Sauls. Nonlinear Meissner effect in CuO superconductors. *Phys. Rev. Lett.*, 69(15):2264–2267, Oct. 1992.

[19] S. K. Yip, D. Xu and J. A. Sauls. Electromagnetic response of d-wave superconductors. *Physica B*, 194-196:1595–1596, 1994.

[20] T. Dahm and D. J. Scalapino. Theory of microwave intermodulation in a high-T_c superconducting resonator. *Appl. Phys. Lett.*, 69(27):4248–4250, Dec. 1996.

[21] J. Bardeen. Two fluid model of superconductivity. *Phys. Rev. Lett.*, 1(11):399–400, Dec. 1958.

[22] S. K. Yip, D. Xu and J. A. Sauls. Nonlinear Meissner effect in unconventional superconductors. *Phys. Rev. B*, 51(22):16233–16253, Jun. 1995.

[23] P. J. Hirschfeld, M.-R. Li and P. Wölfle. Is the nonlinear Meissner effect unobservable? *Phys. Rev. Lett.*, 81(25):5640–5643, Dec. 1998.

[24] P. J. Hirschfeld W. O. Putikka and P. Wölfle. Unusual low-frequency electromagnetic response in anisotropic superconductors: Application to UPt_3. *Phys. Rev. B*, 41(10):7285–7288, Apr. 1990.

[25] C. C. Tsuei and J. R. Kirtley. Pairing symmetry in cuprate superconductors. *Rev. Mod. Phys.*, 72(4):969–1016, Oct. 2000.

[26] T. Dahm and D. J. Scalapino. Theory of intermodulation in a superconducting microstrip resonator. *J. Appl. Phys.*, 81(4):2002–2009, Feb. 1997.

[27] T. Dahm and D. J. Scalapino. Intermodulation and quality factor of high-T_c superconducting microstrip structures. *J. Appl. Phys.*, 82(1):464–468, Jul. 1997.

[28] T. Dahm and D. J. Scalapino. Nonlinear current response of a d-wave superfluid. *Phys. Rev. B*, 60(18):13125–13130, Nov. 1999.

[29] T. Dahm. D. J. Scalapino and B. A. Willenmsen. Phenomenological theory of intermodulation in HTS resonators and filters. *J. Superconduct.*, 12(2):339–342, 1999.

[30] G. Koren, A. Gupta, R. J. Beserman, M. I. Lutwyche, and R. B. Laibowitz. Laser wavelength dependent properties of $YBa_2Cu_3O_{7-\delta}$ thin films deposited by laser ablation. *Appl. Phys. Lett.*, 55(23):2450–2452, Dec. 1989. The high quality epitaxial PLD films used in the present study, were produced using the 355 nm laser wavelength. They have a room temperature resistivity of $0.2m\Omega$ cm, T_c = 90-91K, and dc j_c (77K) = $4 - 5 \times 10^6 \mathrm{A/cm}^2$.

[31] A. C. Anderson, R. L. Slattery, D. E. Oates, and L. S. Yu-Jahnes. Cylindrical magnetron deposition of high-quality high-temperature superconductive thin films. *Lincoln Lab., Lexington, MA, Solid State Res. Quarterly Tech. Rep.*, 2:31–34, 1993.

[32] A. C. Westerheim, L. S. Yu-Jahnes, and Alfredo C. Anderson. Off-axis magnetron sputtering of YBCO films: The influence of atomic oxygen. *IEEE Trans. Magnetics*, 27(2):1001–1005, Mar. 1991.

[33] G. Hammerl, H. Bielefeldt, B. Goetz, A. Schmehl, C. W. Schneider, R. R. Schulz, H. Hilgenkamp, and J. Mannhart. Doping-induced enhancement of grain boundary critical currents. *IEEE Trans. Appl. Supercond.*, 11(1):2830–2837, Mar. 2001.

[34] M. Lorenz, H. Hochmuth, D. Natusch, T. Thärigen, V. L. Svetchnikov, H. W. Zandbergen, C. Schäfer, G. Kästner, and D. Hesse. Microstructure of YBCO and YBCO/$SrTiO_3$/YBCO PLD thin films on sapphire for microwave application. *Mat. Res. Soc. Symp. Proc.*, 603(1):163–168, 2000.

[35] M. Lorenz, H. Hochmuth, D. Natusch, M. Kusunoki, V. L. Svetchnikov, V. Riede, I. Stanca, G. Kästner, and D. Hesse. Doping-induced enhancement of grain boundary critical currents. *IEEE Trans. Appl. Supercond.*, 11(1):3209–3212, Mar. 2001.

[36] G. Kästner, D. Hesse, M. Lorenz, R. Scholz, N. D. Zakharov, and P. Kopperschmidt. Microcracks observed in epitaxial thin films of $YBa_2Cu_3O_{7-\delta}$ and $GdBa_2Cu_3O_{7-\delta}$. *phys. stat. sol (a)*, 150(381):381–394, 1995.

[37] G. Kästner, C. Schäfer, S. Senz, D. Hesse, M. Lorenz, H. Hochmuth, M. Getta, M. A. Hein, T. Kaiser, and G. Müller. Microstructure and microwave surface resistance of YBaCuO thin films. *IEEE Trans. Appl. Supercond.*, 9(2):2171–2174, Jun. 1999.

[38] N. G. Chew, S. W. Goodyear, J. A. Edwards, J. S. Satchell, S. E. Blenkinsop and R. G. Humphreys. Effect of small changes in composition on the electrical and structural properties of $YBa_2Cu_3O_7$ thin films.

[39] R. G. Humphreys, J. S. Satchell, N. G. Chew, J. A. Edwards, S. W. Goodyear, M. N. Keene and S. J. Hedges. Evaporated $Yba_2Cu_3O_7$ thin films and device technology. *Mater. Sci. Eng. B*, 10(4):293–303, Dec. 1991.

[40] K. K. Berggren, E. M. Macedo, D. A. Feld and J. P. Sage. Low T_c superconductive circuits fabricated on 150-nm-diameter wafers using a doubly planarized $Nb/AlO_x/Nb$ process. *IEEE Trans. Appl. Supercond.*, 9(2):3271–3274, Jun. 1999. The niobium was deposited as the first step of the trilayer process described in this publication.

[41] B. A. Willemsen, B. H. King, T. Dahm and D. J. Scalapino. Microwave intermodulation in high-T_c superconducting microstrip resonators. *IEEE Trans. Appl. Supercond.*, 9(2):4181–4184, Jun. 1999.

[42] D. E. Oates and A. C. Anderson. Surface impedance measurements of $YBa_2Cu_3O_{7-X}$ thin films in stripline resonators. *IEEE Trans. Mag.*, 27(2):867–871, Mar. 1991.

[43] D. E. Oates, P. P. Nguyen, G. Dresselhaus M. S. Dresselhaus, G. Koren and E. Polturak. Nonlinea surface impedance of YBCO thin films: Measurements, modeling, and effects in devices. *J. Superconduct.*, 8(6):725–733, 1995.

[44] M. Sucher and J. Fox. *Handbook of Microwave Measurements*, volume 2, pages 455–467. Polytechnic Press of the Polytechnic Institute of Brooklyn, New York, New York, third edition, 1963.

[45] D. M. Sheen, S. M. Ali, D. E. Oates, R. S. Withers and J. A. Kong. Current distribution, resistance, and inductance for superconducting strip transmission lines. *IEEE Trans. on Appl. Superconduct.*, 1(2):108–115, Jun. 1991.

[46] D. E. Oates, A. C. Anderson, D. M. Sheen and S. M. Ali. Stripline resonator measurements of Z_S versus H_{rf} in $YBa_2Cu_3O_{7-X}$ thin films. *IEEE Trans. On Microwave Theory and Tech.*, 39(9):1522–1529, Sep. 1991.

[47] D. E. Oates, A. C. Anderson and P. M. Mankiewich. Measurement of the surface resistance of $YBa_2Cu_3O_{7-x}$ thin films using stripline resonators. *J. of Superconduct.*, 3(3):251–259, 1990.

[48] D. E. Oates, S. H. Park, D. Agassi and G. Koren. Temperature dependence of intermodulation distortion in YBCO. *Supercond. Sci. Technol.*, 17:S290–S294, 2004.

[49] D. E. Oates, S. H. Park and G. Koren. Temperature dependence of nonlinear meissner effect. to be published in Physical Review Letters.

[50] E. A. Vopilkin, A. E. Parafin, and A. N. Reznik. Intermodulation in a microwave resonator with a high-temperature superconductor. *Technical Physics*, 45(2):214–220, 2000.

[51] A. A. Abrikosov and L. P. Gorkov. Contribution to the theory of superconducting alloys with paramagnetic impurities. *JETP*, 12:1243–1253, 1961.

[52] E. W. Hudson, K. M. Lang, V. Madhavan, S. H. Pan, H. Eisaki, S. Uchida and J. C. Davis. Interplay of magnetism and high-T_c superconductivity at individual Ni impurity atoms in $bi_2Sr_2CaCu_2O_{8+\delta}$. *Nature*, 411:920–924, Jun. 2001.

[53] S. H. Pan, E. W. Hudson, K. M. Lang, H. Eisaki, S. Uchida and J. C. Davis. Imaging the effects of individual zinc impurity atoms on superconductivity in $bi_2Sr_2CaCu_2O_{8+\delta}$. *Nature*, 403:746–750, Feb. 2000.

[54] P. Monthoux and D. Pines. Spin-fluctuation-induced superconductivity and normal-state properties of $YBa_2Cu_3O_7$. *Phys. Rev. B*, 49:4261–4278, 1994.

[55] D. Pines. Understanding high temperature superconductors: progress and prospects. *Physica C*, 282-287:273–278, 1997.

[56] J. Halbritter. RF residual losses, surface impedance, and granularity in superconducting cuprates. *J. Appl. Phys.*, 68(12):6315–6326, Dec. 1990.

[57] M. Hein. *High-Temperature-Superconductor Thin Films at Microwave Frequencies*, volume 155 of *Springer Tracts in Modern Physics*, chapter 3.3, page 151. Springer-Verlag, Berlin, Germany, 1999.

[58] M. A. Hein, R. G. Humphreys, P. J. Hirst, S. H. Park and D. E. Oates. Nonlinear microwave response of epitaxial YBaCuO films of varying oxygen content on MgO substrates. *Journal of Superconductivity*, 16(5):895–904, Oct. 2003.